

DESIGN OF LOW ENERGY NEGATIVE CARBON ION BEAMLINE FOR
ACCELERATOR MASS SPECTROMETER (AMS)

NATTHAPONG SAENGWISES



A Thesis Submitted in Partial fulfillment of the Requirements for the

Degree of Master of Science in Applied Physics

Suranaree University of Technology

Academic Year 2024

การออกแบบระบบลำเลียงคาร์บอนไดออกไซด์พลังงานต่ำสำหรับเครื่อง
สเปกโตรมิเตอร์มวลโดยอาศัยเครื่องเร่งอนุภาค



วิทยานิพนธ์นี้เป็นส่วนหนึ่งในการศึกษาตามหลักสูตรปริญญาวิทยาศาสตรมหาบัณฑิต

สาขาวิชาฟิสิกส์ประยุกต์

มหาวิทยาลัยเทคโนโลยีสุรนารี

ปีการศึกษา 2567

DESIGN OF LOW ENERGY NEGATIVE CARBON ION BEAMLINE FOR
ACCELERATOR MASS SPECTROMETER (AMS)

Suranaree University of Technology has approved this thesis submitted in
partial fulfillment of the requirements for a Master's Degree.

Thesis Examining Committee



A blue ink signature of Assoc. Prof. Dr. Prapun Manyum.

(Assoc. Prof. Dr. Prapun Manyum)
Chairperson



A blue ink signature of Assoc. Prof. Dr. Prayoon Songsiritthigul.

(Assoc. Prof. Dr. Prayoon Songsiritthigul)
Member (Thesis advisor)



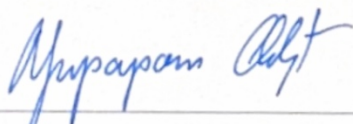
A blue ink signature of Assoc. Prof. Dr. Panomsak Meemon.

(Assoc. Prof. Dr. Panomsak Meemon)
Member



A blue ink signature of Dr. Keerati Manasatitpong.

(Dr. Keerati Manasatitpong)
Member



A blue ink signature of Assoc. Prof. Dr. Yupaporn Ruksakulpiwat.

(Assoc. Prof. Dr. Yupaporn Ruksakulpiwat)
Vice Rector for Academic Affairs
and Quality Assurance



A blue ink signature of Prof. Dr. Santi Maensiri.

(Prof. Dr. Santi Maensiri)
Dean of Institute of Science

ณัฐพงศ์ แสงวิเศษ : การออกแบบระบบลำเลียงคาร์บอนไอออนลบพลังงานต่ำสำหรับ
เครื่องสเปกโตรมิเตอร์มวลโดยอาศัยเครื่องเร่งอนุภาค (DESIGN OF LOW ENERGY
NEGATIVE CARBON ION BEAMLINE FOR ACCELERATOR MASS SPECTROMETER)
อาจารย์ที่ปรึกษา : รองศาสตราจารย์ ดร.ประยูร ส่งศิริฤทธิกุล, 78 หน้า

คำสำคัญ: เครื่องสเปกโตรมิเตอร์มวลโดยอาศัยเครื่องเร่งอนุภาค, การวัดอายุด้วยคาร์บอน-14, ระบบ
ลำเลียงคาร์บอนไอออนลบพลังงานต่ำ

งานวิจัยนี้มีวัตถุประสงค์เพื่อพัฒนาระบบผลิตและลำเลียงคาร์บอนไอออนลบพลังงานต่ำ
สำหรับเครื่องสเปกโตรมิเตอร์แยกแยะมวลโดยใช้เครื่องเร่งอนุภาค (Accelerator Mass
Spectrometer, AMS) โดยลดขนาดให้กะทัดรัดและประหยัดงบประมาณด้วยการนำอุปกรณ์ที่มีอยู่
ภายในสถาบันวิจัยแสงซินโครตรอน (องค์การมหาชน) มาใช้ใหม่ โดยระบบประกอบไปด้วย
แหล่งกำเนิดไอออนชนิดซีเซียมสปัตเตอร์, octupole deflector, Einzel lens และ aperture slit ที่
ทีมวิจัยร่วมกับวิศวกรจากสถาบันวิจัยดาราศาสตร์แห่งชาติ (องค์การมหาชน) สร้างแบบจำลองสาม
มิติในโปรแกรม SolidWorks และจำลองการเคลื่อนที่ของไอออนด้วยโปรแกรม CST Studio Suite
ผลการจำลองแสดงว่า ลำคาร์บอนไอออนลบพลังงาน 40 กิโลอิเล็กตรอนโวลต์ สามารถโฟกัสให้มี
ขนาดรากลึกที่สองของค่าเฉลี่ยกำลังสองเท่ากับ 2.42×2.38 มม.² และมีขนาดของ emittance เท่ากับ
8 mm·mrad (1.6 mm·mrad·√MeV) ที่ตำแหน่งของ aperture slit พร้อมอัตราการส่งผ่านของ
ไอออนกว่า 99 % ผ่าน aperture slit ขนาด 20×20 มม.² การตั้งแรงดันไฟฟ้าที่ Einzel lens
ขนาด -20,139 โวลต์ ช่วยโฟกัสลำไอออนมายังตำแหน่ง aperture slit ได้อย่างแม่นยำ

การศึกษาความคลาดเคลื่อนในการประกอบระบบนั้นพบว่า octupole deflector ยังคงให้
การส่งผ่านลำไอออนกว่า 99 เปอร์เซ็นต์ ถึงแม้จะมีมุมบิด 2 องศา และการเลื่อนไปจากแกนกลาง 2
มม. ขณะที่ Einzel lens ต้องการความคลาดเคลื่อนที่น้อยกว่า (เลื่อนไปจากแกนกลางได้ไม่เกิน 0.4
มม. และบิดได้ไม่เกิน 0.6 องศา) เนื่องจากสนามไฟฟ้าบริเวณนี้มีความเข้มสูง การคลาดเคลื่อนเพียง
เล็กน้อยก็ทำให้ลำไอออนเบี่ยงออกนอกโฟกัสได้ และการทดลองศึกษาผลกระทบของส่วนจับยึดของ
Einzel lens ภายในสุญญากาศนั้นพบว่าผลกระทบต่อลำไอออนจากการไปรบกวนสนามไฟฟ้า
บริเวณระหว่างทรงกระบอกของ Einzel lens แก้ไขได้โดยการขยับทรงกระบอกเข้ามาใกล้กันมากขึ้น

ระบบสุญญากาศสร้างจากอุปกรณ์ที่ไม่ได้ใช้งานภายในสถาบันวิจัยแสงซินโครตรอน ผ่านการ
ทำความสะอาดด้วยแอลกอฮอล์และทดสอบการรั่วด้วยเครื่องตรวจวัดแก๊สฮีเลียม (Pfeiffer Adixen
ASM 340) พบอัตราการรั่ว 10^{-9} mbar·L/s ซึ่งเป็นอัตราที่น้อยกว่าค่ามาตรฐาน 10^{-8} mbar·L/s จึง
พร้อมใช้งานได้จริง ระบบประกอบด้วยปั๊มเทอร์โบโมเลกุลขนาด 300, 350 และ 700 L/s สำหรับการ
สร้างสุญญากาศสูงพิเศษ โดยใช้ร่วมกับ scroll pump สำหรับสร้างสุญญากาศเบื้องต้น

อุปกรณ์จ่ายแรงดันไฟฟ้าสูงจากบริษัท Matsusada Precision Inc. ของประเทศญี่ปุ่น
จำนวน 10 เครื่อง ถูกเลือกใช้งานกับระบบซึ่งจำแนกได้เป็น การใช้งานสำหรับแหล่งกำเนิดไอออน

จำนวน 4 เครื่อง สำหรับสร้างสนามไฟฟ้าให้กับไอออนไนเซอร์และ Einzel lens อย่างละ 1 เครื่อง สำหรับ octupole deflector จำนวน 4 เครื่อง เพื่อใช้ในการเบี่ยงลำไอออนไนแกน X-Y ได้อย่างอิสระ โดยระบบจ่ายไฟฟ้าแรงดันสูงนั้นถูกควบคุมผ่านอินเทอร์เฟซ CO-HV/CO-E32 ด้วยสายไฟเบอร์ออปติก ทำให้ควบคุมและติดตามได้แม่นยำ ปลอดภัยจากสัญญาณรบกวน และวางติดตั้งได้สะดวกเพื่อให้ภายนอกห้องสุญญากาศอยู่ที่สก็ยกรวาด

ขดลวดความร้อนภายในไอออนไนเซอร์ใช้เส้นลวดโมลิบดีนัมเรเนียม (MoRe) ขนาดเส้นผ่านศูนย์กลาง 0.9 มม. พันเป็นวงกลมทรงโดนัท ซึ่งจากการศึกษาที่เคยมีมาก่อนนั้นใช้กำลังไฟ 150 วัตต์ ที่อุณหภูมิ 1200 องศาเซลเซียส และจากการคำนวณกฎของโอห์มและสมการความต้านทานไฟฟ้าในเส้นลวดนั้นจะต้องใช้ความยาวลวด 20 ซม. พันรอบแกน 2 มม. จำนวน 22 รอบ โดยจากการทดลองพบว่าสามารถเพิ่มจำนวนรอบในการพันได้เป็น 40 รอบเพื่อลดการใช้พลังงานจากอุปกรณ์จ่ายแรงดันไฟฟ้าลง และจากการทดลองพบว่าใช้พลังงานเพียง 70 วัตต์ เพื่อไปถึงอุณหภูมิสูงสุดที่ 1370 องศาเซลเซียส และสำหรับการทดลองทำแม่พิมพ์เพื่อกดเข้ากับดินน้ำมันที่นำมาจำลองการเป็นฉนวนระหว่างขดลวดความร้อนและไอออนไนเซอร์นั้นพบว่าแม่พิมพ์นี้สามารถกดและทำให้เกิดฉนวนหนา 1 มม. ได้แต่ยังไม่เรียบเนื่องจากมีรอยการจากสร้างตัวต้นแบบจากเครื่องพิมพ์สามมิติ เสนอแนวทางปรับปรุงด้วยการผลิตแม่พิมพ์อลูมิเนียมจากเครื่องกลึงเพื่อผิวที่เรียบและทนทานขึ้น

ผลการวิจัยทุกขั้นตอนยืนยันว่าโครงสร้างและระบบพร้อมใช้งาน มีคุณภาพลำไอออนตามเป้าหมาย ระบบมีขนาดกะทัดรัด และเหมาะสมต่อการใช้งานเป็นระบบ AMS วัดรังสีคาร์บอนครั้งแรกในประเทศไทยเพื่อรองรับการวิเคราะห์โบราณคดีและสิ่งแวดล้อมอย่างมีประสิทธิภาพ

NATTTHAPONG SAENGWISES : DESIGN OF LOW ENERGY NEGATIVE CARBON ION BEAMLINE FOR ACCELERATOR MASS SPECTROMETER. THESIS ADVISOR : ASSOCIATE PROFESSOR PRAYOON SONGSIRIRITTHIGUL, Ph.D. 78 PP.

Keywords: AMS, mass spectrometer, radiocarbon dating, low energy beamline

This research is aimed at developing a compact, low-energy negative carbon ion beamline for accelerator mass spectrometry (AMS) by using existing equipment at the Synchrotron Light Research Institute (Public Organization) to reduce size and cost. The beamline is composed of a cesium-sputter ion source, an octupole deflector, an Einzel lens, and an aperture slit. Three-dimensional models were generated in SolidWorks in collaboration with engineers from the National Astronomical Research Institute of Thailand (Public Organization), and ion trajectories were simulated using CST Studio Suite. Simulation results demonstrate that a 40 keV C^- beam can be focused to an RMS beam size of $2.42 \times 2.38 \text{ mm}^2$, with an emittance of $8 \text{ mm}\cdot\text{mrad}$ ($1.6 \text{ mm}\cdot\text{mrad}\cdot\sqrt{\text{MeV}}$) at the aperture slit, achieving over 99 % transmission through a $20 \times 20 \text{ mm}^2$ opening. A $-20,139 \text{ V}$ bias applied to the Einzel lens enables precise focusing of the ion beam at the slit location.

Misalignment studies revealed that the octupole deflector maintains over 99 % ion transmission even with a 2° tilt and a 2 mm offset from the optical axis. In contrast, the Einzel lens requires much tighter assembly tolerances—offsets no greater than 0.4 mm and tilts no more than 0.6° —because its strong electric field is highly sensitive to small displacements, which can lead to beam loss. Vacuum simulations of the Einzel lens mounting supports also indicated that conductive supports can perturb the field between the cylinders; this effect can be mitigated by reducing the gap between them.

The vacuum system was assembled from unused equipment at SLRI, cleaned with alcohol, and leak-tested using a Pfeiffer Adixen ASM 340 helium detector. Measured leak rates of approximately $10^{-9} \text{ mbar}\cdot\text{L/s}$ —below the $10^{-8} \text{ mbar}\cdot\text{L/s}$ threshold—confirmed readiness for operation. The system incorporates turbomolecular pumps with capacities of 300, 350, and 700 L/s for ultra-high vacuum, backed by a scroll pump for rough pumping.

Ten high-voltage power supplies from Matsusada Precision Inc. (Japan) were selected: four units for the ion source, one each for the ionizer and the Einzel lens to

generate the electric field, and four for the octupole deflector to provide independent X–Y beam steering. All supplies are controlled and monitored via CO-HV/CO-E32 fiber-optic interfaces, ensuring precise, noise-free operation, and are installed beneath the table so that the exterior of the vacuum chamber remains at ground potential.

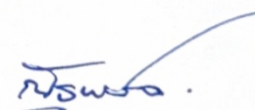

The ionizer heater coil is wound from 0.9 mm-diameter molybdenum-rhenium (MoRe) wire in a toroidal configuration. Based on Ohm's law and the resistivity equation, a 20 cm coil length wound in 22 turns on a 2 mm mandrel was calculated to reach 1200 °C with approximately 150 W of power. Experimental testing showed that increasing the turn count to 40 reduced power consumption to 70 W while achieving a maximum temperature of 1370 °C. A 3D-printed tamper was used to press alumina paste into the gap between coil and ionizer body, producing a 1 mm-thick insulator layer, though surface unevenness from printing artifacts was observed. Machining the tamper from aluminum is proposed to improve surface smoothness and durability.

Overall, the integrated system meets its performance targets—compact footprint, beam quality, alignment tolerances, vacuum integrity, and reliable heating—and establishes Thailand's first in-house AMS radiocarbon dating capability for archaeological and environmental analysis.

มหาวิทยาลัยเทคโนโลยีสุรนารี

School of Physics
Academic Year 2024

Student's signature
Advisor's signature

ACKNOWLEDGEMENTS

First and foremost, I would like to express my deepest gratitude to my advisor, Assoc. Prof. Dr. Prayoon Songsiriritthigul, for his unwavering guidance in vacuum system fundamentals and his invaluable advice over the past four years. His mentorship has been instrumental in shaping both the scientific rigor and practical skills required for this work.

I am also grateful to the staff of the Synchrotron Light Research Institute (SLRI), especially Dr. Keerati Manasatitpong for his expert guidance on CST Studio Suite, and Surachet Rattanasuporn for procuring and maintaining the necessary equipment, as well as for his hands-on support in troubleshooting. My thanks also go to the electrical engineer at SLRI for ensuring the safety of all high-voltage operations. I would like to thank the engineering team from the National Astronomical Research Institute of Thailand (NARIT), in particular Chaiwat Theppawong, for their continuous collaboration on SolidWorks design and integration.

Special thanks to my colleagues in the AMS laboratory at SLRI for their friendship, assistance in data collection, and constant motivation. I am deeply appreciative of my family for their unwavering support of my studies, and to my friends for their encouragement during challenging times.

My master's studies were supported by the Development Program in Science and Technology (DPST). Finally, I am thankful to everyone who contributed, directly or indirectly, to the successful completion of this thesis.

Natthapong Saengwises

CONTENTS

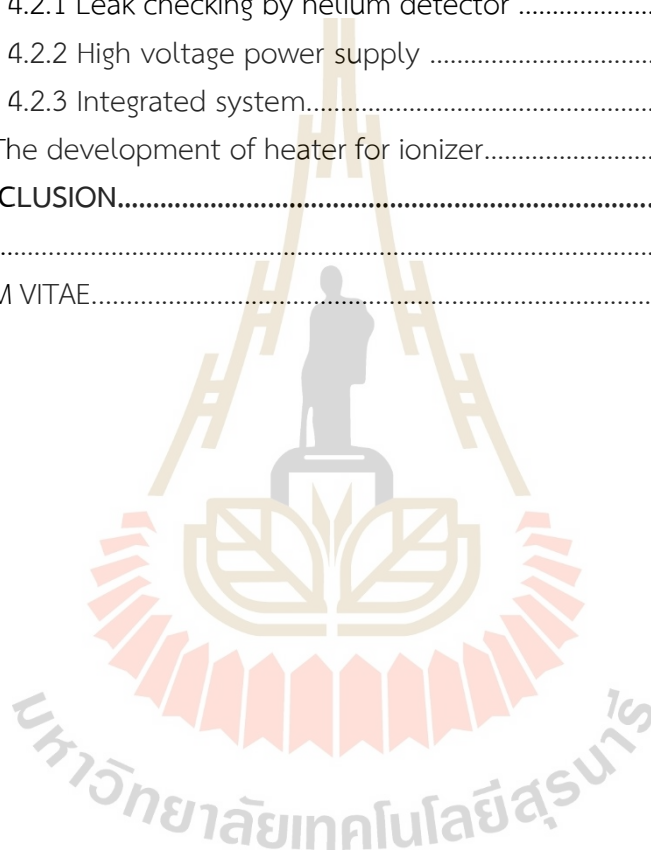
	Page
ABSTRACT IN THAI.....	I
ABSTRACT IN ENGLISH.....	III
ACKNOWLEDGEMENTS.....	V
CONTENTS.....	VI
LIST OF TABLES.....	IX
LIST OF FIGURES.....	X
CHAPTER	
I INTRODUCTION.....	1
1.1 Introduction.....	1
1.2 Research objectives.....	3
1.3 Scope of thesis.....	4
1.4 Outline of thesis.....	4
II LITERATURE REVIEWS	5
2.1 Accelerator Mass Spectrometry (AMS).....	5
2.2 Development of AMS.....	6
2.3 Mini Carbon Dating System (MICADAS)	8
2.4 Electrostatic deflector.....	10
2.5 Electrostatic lens.....	13
2.6 Heater for ionizer	16
2.6.1 Design of the ionizer from HeatWave Labs, Inc.	17
2.6.2 Properties of MoRe alloy.....	18
2.7 Particle tracking solver in CST Studio Suite	21
2.7.1 Finite element analysis.....	21
2.7.2 Equation of motion (Lorentz force law).....	22
2.7.3 Maxwell's equations.....	22
2.7.3.1 Gauss's law (Electric).....	23
2.7.3.2 Gauss's law for magnetism.....	23
2.7.3.3 Faraday's law.....	23
2.7.3.4 Ampère - Maxwell law.....	23

CONTENTS (Continued)

	Page
III RESEARCH METHODOLOGY.....	24
3.1 Simulation using CST Studio Suite.....	24
3.1.1 Particle tracking simulation.....	24
3.1.1.1 Mesh refinement.....	25
3.1.1.2 Convergence study.....	26
3.1.1.3 Transfer source via define particle export interface.....	27
3.1.2 Ion source simulation.....	29
3.1.3 The study of miss alignment of the octupole deflector.....	31
3.1.4 Einzel lens simulation.....	33
3.1.4.1 The study of effects from mounting support.....	33
3.1.4.2 The study of focal range.....	35
3.1.4.3 The study of miss alignment.....	36
3.1.5 Low-energy negative carbon ion beamline simulation.....	37
3.2 Low-energy beamline design.....	39
3.2.1 Vacuum system.....	39
3.2.1.1 Existing vacuum components at SLRI.....	39
3.2.1.2 Leak checking by helium detector.....	43
3.2.2 High Voltage Power Supply (HVPS).....	45
3.2.2.1 HVPS for ion source.....	45
3.2.2.2 HVPS for octupole deflector.....	46
3.2.2.3 HVPS for Einzel lens.....	46
3.2.2.4 High voltage isolation transformer.....	46
3.2.3 Integrated system.....	47
3.3 The development of heater for ionizer.....	47
3.3.1 Calculation and design of the toroidal heater.....	47
3.3.2 Fabrication of the toroidal heater.....	49
3.3.3 Experimental setup.....	51
IV RESULTS AND DISCUSSION.....	52
4.1 Computer simulation results.....	52
4.1.1 Convergence study.....	53
4.1.2 The study of miss alignment of the octupole deflector.....	54
4.1.3 Einzel lens simulation results.....	56
4.1.3.1 The study of effects from mounting support.....	56

CONTENTS (Continued)

	Page
4.1.3.2 The study of focal range.....	59
4.1.3.3 The study of miss alignment.....	61
4.1.4 Low-energy negative carbon ion beamline simulation results....	62
4.2 Low-energy beamline design	64
4.2.1 Leak checking by helium detector	64
4.2.2 High voltage power supply	64
4.2.3 Integrated system.....	66
4.3 The development of heater for ionizer.....	67
V CONCLUSION.....	72
REFERENCES.....	73
CURRICULUM VITAE.....	78



LIST OF TABLES

Table		Page
2.1	Power Consumption of the Ionizer Heater at Different.....	18
2.2	Mechanical, Physical, Electrical, and Thermal Properties of MoRe Alloy	19
4.1	Acceptable tolerances for the central electrode of the Einzel Lens.....	62
4.2	Recording data on MoRe filament heating under vacuum conditions.....	68



LIST OF FIGURES

Figure	Page
1.1 The AMS system at the Lalonde AMS Lab, University of Ottawa, operates with a terminal voltage of 3 MV.....	1
2.1 The layout of AMS system at Japan Atomic Energy Agency Accelerator Mass Spectrometry facility at Tono (JAEA-AMS-TONO)	6
2.2 The layout of MICADAS. With its small dimensions of $2.5 \times 3 \text{ m}^2$	7
2.3 Simplified diagram of the ion optics of the MICADAS system.....	8
2.4 Octupole deflector.....	10
2.5 The schematic design of the octupole deflector.....	11
2.6 The horizontal (a) and vertical (b) profiles of a 40 keV C^- beam horizontally deflected with ΔV_y set to zero, while ΔV_x is varied from 0 to +300 V.....	11
2.7 The simulated deviated angle of a 40 keV C^- beam after passing through the deflector as a function of ΔV	12
2.8 The emittance of the 40-keV C^- beam entering the deflector at 40 mm from source.....	12
2.9 Cutaway view of ion trajectories in an Einzel lens.....	13
2.10 Geometry of the ion source, electrostatic Einzel lens, and analyzing magnet implemented via the SIMION code	14
2.11 Simulation results for beam transmission in two different modes of the Einzel lens: (a) accel-decel mode and (b) decel-accel mode	14
2.12 The ion beam envelope and electric field component on the beam axis beam when the electrostatic einzel lens was biased with (a) 46,903 V and (b) -20,951 V	15
2.13 The emittance of the ion beam when the ES Einzel lens was biased with (a) 46,903 V and (b) -20,951 V	15
2.14 Cross-sectional drawing of an electro-static einzel lens with three cylindrical tube electrodes	16
2.15 Drawing of the Ø1.38-inch ionizer heater from HeatWave Labs.....	17
2.16 Electrical Resistivity of TZM Alloy, HT Alloy, and Pure Molybdenum vs. Temperature	20

LIST OF FIGURES (Continued)

Figure	Page
2.17 Mesh types for computer simulation. (a) Tetrahedral mesh (b) Hexahedral mesh	21
3.1 Flow chart of particle tracking simulation in CST Studio Suite.....	25
3.2 Mesh Generation for the particle tracking solver module in CST.....	26
3.3 The global mesh settings, where the N_mesh variable is defined in the mesh properties, are used with the parameter-sweep function to perform the convergence study.....	26
3.4 In the parameter sweep function, the N_mesh variable is swept from 20 to 200 in steps of 20, yielding 10 values (20, 40, 60, ..., 200) and progressively increasing the mesh density.....	27
3.5 Defining the particle export interface. a) Boundary and position setup for particle export at the ion focus point, located 160 mm from the emission point; the boundary plane is sized larger than the beam envelope. b) Example of the particle export interface (blue plane) defined for the ion source, using the known focal position of the ion beam.....	28
3.6 Setting the kinetic energy and angular spread of the particle sources to model the effects of HVPS ripple and the sputtering process respectively.....	29
3.7 Simulation results of the ion source a) Trajectories of ^{12}C , ^{13}C , and ^{14}C ions focused at 160 mm from the source. b) Particle distribution image at the focal point c) Energy spreads at the focal point.....	30
3.8 Comparison of a new ionizer (left) and a used ionizer (right), showing burn marks at the center caused by sputtered ions spreading in all directions and striking the surface.....	31
3.9 The octupole deflector model has rods each 10 mm in diameter and a total inner diameter of 40 mm	32
3.10 The aperture slit design consists of four independently adjustable blades, each movable along the $\pm x$ and $\pm y$ axes, allowing a maximum square opening of $20 \times 20 \text{ mm}^2$ or complete closure. Each blade also serves as a current collector to measure and monitor the ion beam. a) Upstream side b) Downstream side.....	33
3.11 The ratio of the Einzel lens lengths (ring1 : gap : ring2).....	34

LIST OF FIGURES (Continued)

Figure	Page
3.12 The Einzel lens model 1 (43 : 21 : 64 mm).....	34
3.13 The Einzel lens model 2 (40 : 6 : 82 mm).....	34
3.14 Optimizer Function Settings in CST Studio Suite a) Definition of variables and their ranges for the solver to vary. b) Specification of the optimization goals.....	35
3.15 The cross section of einzel lens design includes mounting supports (shown on the leftmost side) shared with the octupole deflector	36
3.16 The cross-section of the low-energy negative carbon ion beamline shows the details and positions of the main components: the ion source (orange), the octupole deflector (pink), the Einzel lens (green), and the aperture slit (blue). The insulator segment is also highlighted. a) Beamline with external details. b) Simplified beamline model for particle-tracking simulation in CST.....	37
3.17 Analysis of the ion beam using particle monitors. a) The 101 monitors spanning from the ion source focal point through and slightly beyond the aperture slit, including Monitor 1 at the slit and Monitor 2 along the beam path. b) Template based post processing showing the results as the ion beam passes each monitor.....	38
3.18 6-Ways Cross Chamber, 8" OD, Sphere Body 9 inch	39
3.19 Adapter CF203 to CF152.....	40
3.20 6-Ways Cross Chamber, 6" OD size 270 mm.....	40
3.21 6-Ways Cross Chamber, 6" OD size 220 mm.....	41
3.22 Edge weld bellow and alignment studs.....	41
3.23 Vacuum gate valve.....	42
3.24 Glass view port.....	42
3.25 Setup of the leak-testing system using a Pfeiffer Adixen ASM 340 leak detector at SLRI.....	43
3.26 Monitoring and recording the leak rate and inlet pressure according to the operating instructions.....	44
3.27 Simplified diagram of the power-supply zones for generating electric fields in the cesium sputter source for AMS at SLRI.....	45

LIST OF FIGURES (Continued)

Figure	Page
3.28 Toroidal heater with 40 turns installed inside the ionizer body.....	48
3.29 Fabrication of the toroidal heater coil by SLRI's machine shop	50
3.30 3D-printed prototype of the tamper by SUT QLAB	50
3.31 Experimental setup for heating the MoRe coil in the vacuum system.....	51
4.1 Optical layout of the negative carbon ion beamline.....	52
4.2 Optimal mesh size of the ion source model	52
4.3 Convergence study graphs used to select the optimal mesh size for the ion source model. a) $rms(position_x)$ vs. plane position b) Emittance vs. plane position	53
4.4 Convergence of gun iteration vs. charge accuracy.....	54
4.5 Comparison of particle images at the aperture slit between perfect alignment (black) and tilt = 2° with offset = 2 mm (red). The black square indicates the maximum slit opening of $20 \times 20 \text{ mm}^2$	55
4.6 Comparison of normalized ion density at the aperture slit for perfect alignment (black) and for the worst-case misalignment with $\theta = 2^\circ$ and offset = 2 mm (red), shown as a histogram.....	56
4.7 Simulated beam image at the focal plane using a -20 kV bias on the central electrode. a) Model 1 with ratio of 43: 21: 64 mm. b) Model 2 ratio of 40: 6: 82 mm. The insulator segment is shown in blue.....	57
4.8 The electric field inside Einzel lens model 1 is shown in a cross-sectional view to illustrate the electric field perturbations around the support rods (black arrows)	58
4.9 Comparison of the focal distances of Einzel lens Model 1 and Model 2.....	59
4.10 Cross-sectional view of the electric field within the Einzel lens, showing how the field strength varies with the applied bias voltage.....	59
4.11 Graph showing the relationship between plane position and $rms(position_x)$ for various V_Einzel values. The plot also indicates the distance from the source to the center of the Einzel lens (389 mm) and the distance from the lens center to the aperture slit (476 mm).....	60
4.12 Trajectories of negative carbon ions through the Einzel lens. a) -17.5 kV, producing an almost parallel beam. b) -20,139 V (from the optimizer), focused exactly at the aperture slit. c) -30 kV, the maximum output of the power supply.....	61

LIST OF FIGURES (Continued)

Figure	Page
4.13 Trajectories of C^- ions through the Einzel lens with a middle electrode 1.6° tilt and 1.6 mm offset from the optical axis.....	61
4.14 Trajectories of C^- ions passing through the perfectly aligned low-energy negative carbon ion beamline.....	62
4.15 Particle images at the aperture slit for the perfectly aligned low energy negative carbon ion beamline. The black square indicates the maximum slit opening of 20 × 20 mm ² . Figure a) mark size = 1.5 and Figure b) mark size = 0.1.....	63
4.16 Energy spread with FWHM at the aperture slit location.	63
4.17 Digital display of the helium leak rate during vacuum component testing	64
4.18 Diagram of the HVPS configuration used in the negative carbon ion beamline.....	65
4.19 A compact system design for the low-energy negative carbon ion beamline, comprising a tabletop vacuum system integrated with HVPS units beneath the table. The ceramic insulator standoffs are shown in red, and the isolation transformer is shown in black.....	66
4.20 Pressing the tamper into modeling clay in the ionizer body's grooves, simulating the application of alumina paste (Al_2O_3)	67
4.21 MoRe heater coil a) Before installation b) During testing at 800 °C	69
4.22 The graph shows the relationship between temperature and resistance....	69
4.23 The graph shows the relationship between temperature and power consumption.....	70
4.24 The graph shows the relationship between temperature and pressure in vacuum system.....	71

CHAPTER I

INTRODUCTION

1.1 Introduction

Accelerator Mass Spectrometry (AMS) is a powerful and precise technique widely used for radiocarbon dating, allowing researchers to determine the age of carbon-based materials by measuring the ratio of ^{14}C to stable isotopes such as ^{12}C and ^{13}C in a sample (Harris, 1987). AMS offers significant advantages over traditional radiometric methods, including gas proportional counting and liquid scintillation counting. It requires much smaller sample sizes and delivers higher precision, making it invaluable for dating samples that are tens of thousands of years old. This capability has greatly benefited fields such as archaeology, geology, and environmental science. Additionally, AMS offers rapid processing times and higher sensitivity, enabling researchers to construct more detailed chronological studies.

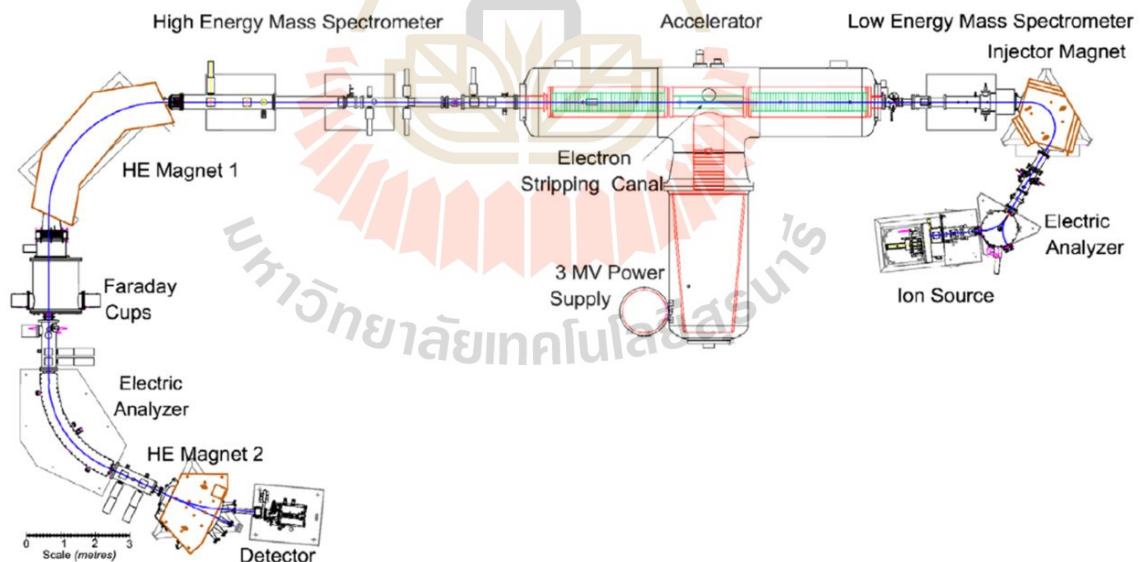


Figure 1.1 The AMS system at the Lalonde AMS Lab, University of Ottawa, operates with a terminal voltage of 3 MV (Kieser, W. E., 2023).

The development of AMS has undergone significant advancements to improve its efficiency and reduce the size of its systems. Historically, AMS systems were large as shown in Figure 1.1 and required high-energy accelerators to achieve the necessary sensitivity for isotope analysis. However, recent innovations have led to the creation of smaller AMS systems that operate at lower terminal voltages (200-300 kV), which significantly reduce both space and power requirements while maintaining high precision. These compact systems can use permanent magnets instead of electro-magnets, further cutting down on energy consumption and the need for cooling. Downsizing these systems not only reduces installation and operational costs but also integrates sample preparation units, enhancing the throughput and versatility of AMS for applications in environmental and archaeological research, among others (Keiser, W. E., 2023).

A critical component within AMS is the ion generation or negative carbon ion beamline, which ensures the stability and quality of the ion beam before it enters the main acceleration phase. The beamline process starts with the generation of negative carbon ions from ion source, after which the ions are extracted and formed into a beam. To maintain the beam's focus and alignment, electrostatic lenses and electrostatic deflectors are used. These elements help correct any initial misalignment and aberrations of ion beam, ensuring that the ion beam remains well-focused and follows the correct trajectory. This focus is essential for the beam to pass efficiently through the acceleration stages and to ensure accurate isotope separation in later steps.

The power supply and vacuum system are essential components for achieving the optimal performance of an AMS system. The power supply is responsible for generating the high-voltage electric potential required to accelerate ions in the beamline. This high voltage creates the electric fields that control the direction of the ions and increase their energy, ensuring that the ion beam remains stable and focused as it moves through the system. Simultaneously, the vacuum system maintains an ultra-high vacuum environment, typically in the range of 10^{-6} to 10^{-9} Torr, as described in the study (Liu et al., 2019). The vacuum system operates with a dynamic pressure of up to 6×10^{-7} Torr throughout the ion source and beamline, maintaining a stable environment crucial for reliable ^{14}C dating, particularly for archaeological and environmental samples. This vacuum is crucial for minimizing collisions between the ions and residual gas molecules, which could otherwise cause scattering and energy loss, degrading the quality of the beam. Together, the power

supply and vacuum system ensure the stability, precision, and efficiency of the ion beam, ultimately contributing to the accuracy of isotope measurements in AMS.

The computer programs used for simulation and design are CST Studio Suite and SolidWorks for creating 3D models of the support structures inside the vacuum chamber, as well as various vacuum components. By conducting design and simulation in parallel, the simulation results become more realistic and reliable.

This work focuses on the design and simulation of a compact, low-energy negative carbon ion beamline for AMS. By designing and building the system in-house, the cost of purchasing a fully assembled unit can be reduced, and personnel capable of troubleshooting and minimizing future maintenance expenses can be developed. Furthermore, this will be Thailand's first radiocarbon dating instrument for archaeological artifacts, offering more affordable in-country testing services compared to sending samples abroad. This thesis presents the engineering design alongside results from computer simulations used to study how mechanical supports affect the electrostatic field and to determine the precise placement of all components inside and outside the vacuum chamber along the beamline. In addition, hands-on testing of the heated filament for carbon ion production was performed, the vacuum system was leak-checked to ensure operational readiness, and high-voltage power supplies were integrated beneath the table to help achieve a truly compact layout.

1.2 Research objectives

A compact system is designed to deliver a negative carbon ion beam with an energy of up to 40 keV, featuring adjustable beam focal length and steering in both X and Y directions. The system must maintain beam emittance below $10 \pi \cdot \text{mm} \cdot \text{mrad} \cdot \sqrt{\text{MeV}}$ with a current of 50 μA at the aperture slit. Assembly tolerances, including allowable tilt angles and positional offsets, are to be defined based on alignment tools and design constraints. Electric fields within the ion source, octupole deflector, and Einzel lens are to be generated using specified parameters, including the integration of a heater, to determine power supply specifications. The beamline vacuum system is to be assembled using existing components available at SLRI, with optical components designed for compatibility. Additionally, a heater for the ionizer is to be developed, and a suitable construction method is to be identified to enable heating up to 1200°C.

1.3 Scope of thesis

- 1.3.1 This thesis focuses on the carbon ion beamline system, which is part of an accelerator mass spectrometer for radiocarbon dating. This beamline consists of four main components: the ion source, an octupole deflector, an Einzel lens, and an aperture slit.
- 1.3.2 Mechanical design of the ion source, octupole deflector and Einzel lens chamber using SolidWorks.
- 1.3.3 CST Studio Suite is used to study the electric field and perform particle simulations, measure beam properties (such as beam emittance, beam position, beam size, and focal length), and investigate the effects of structural supports on the electric field.
- 1.3.4 Primarily, existing vacuum components and chambers, along with a scroll pump and a turbomolecular pump from SLRI, are utilized to minimize costs.

1.4 Outline of thesis

This thesis is divided into five chapters. Chapter I is the Introduction, consisting of the background, objectives, and scope of the work. In Chapter II, an overview of AMS is provided, followed by a discussion on the development of AMS and ongoing efforts to downsize AMS systems. The role of electrostatic components in the ion beamline, including the octupole deflector and Einzel lens, is explained, and Maxwell's equations for particle-tracking simulations in CST Studio Suite are described. Chapter III is divided into three parts: the first presents CST simulations; the second describes the assembly of the compact system, including vacuum components, vacuum leak checking, and high-voltage power supplies; and the third details the development of the heater for the ionizer and filament heating inside the vacuum chamber. In Chapter IV, the experimental results are presented and discussed. Finally, Chapter V provides a summary of the findings along with concluding remarks.

CHAPTER II

LITERATURE REVIEW

In this section, an overview of AMS is presented, followed by a discussion of its development and the ongoing efforts to downsize AMS systems. The functions of key electrostatic components in the ion beamline, including the octupole deflector and Einzel lens, are explained. Additionally, the design of the Heatwave Labs ionizer and the calibration of the heating filament's power consumption are described. Finally, Maxwell's equations relevant to particle-tracking simulations in CST Studio Suite are introduced.

2.1 Accelerator Mass Spectrometry (AMS)

AMS is a sensitive and robust technique typically applied to the quantification of long-lived radioisotopes in samples too small to be decay-counted (Marchetti et al., 2005). Mass spectrometers (Haag, A. M., 2016) comprised of three main components: an ion source, a mass analyzer, and a detector. AMS for radiocarbon dating is an advanced technique for determining the age of biological samples by finding the proportion of the radioisotope of ^{14}C to ^{12}C in graphite form. While the conventional technique determines the age of a sample by counting the radioactivity of ^{14}C (β -minus decay reaction). In comparison (Harris, 1987), the AMS technique, which directly measures the ratio of ^{14}C to ^{12}C atoms, allows for faster and more accurate analysis of samples with very low quantities of graphite (Seema S. Ojha, 2013). showed that minimum sample size is thus reduced approximately 1000-fold (from 1 g to 1 mg), and the datable time span of the method can, theoretically, be doubled (from 40,000 to 80,000 years).

2.2 Development of AMS

The development of AMS has seen significant advancements over the decades, particularly in terms of downsizing the system. Initially, AMS systems required large, high-energy accelerators with terminal voltages in the range of MeV (Mega-electron volts), such as the systems seen at Japan Atomic Energy Agency Accelerator Mass Spectrometry facility at Tono (JAEA-AMS-TONO) as shown in Figure 2.1, which utilized terminal voltages of 4.5 MV or higher (Matsubara et al., 2014).

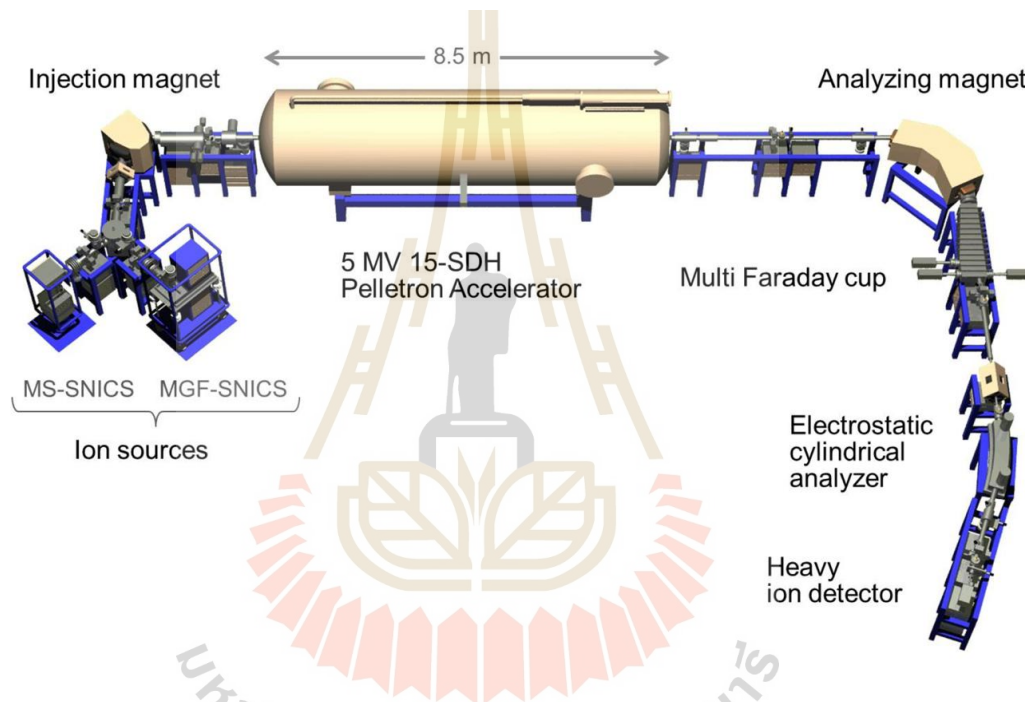


Figure 2.1 The layout of AMS system at Japan Atomic Energy Agency Accelerator Mass Spectrometry facility at Tono (JAEA-AMS-TONO) (Matsubara et al., 2014).

These large systems were effective in providing high-precision isotopic measurements but were costly, required significant space, and involved complex operational demands. However, in recent years, advancements in technology have enabled the development of compact AMS systems that operate at much lower terminal voltages, typically around 200 kV. An example of this innovation is the Mini Carbon Dating System (MICADAS), a compact AMS setup that achieves high performance despite its smaller size. With overall dimensions of just $2.5 \times 3 \text{ m}^2$ as shown in Figure 2.2, MICADAS integrates all essential components, including a high-voltage power supply and vacuum system, into a highly compact footprint.

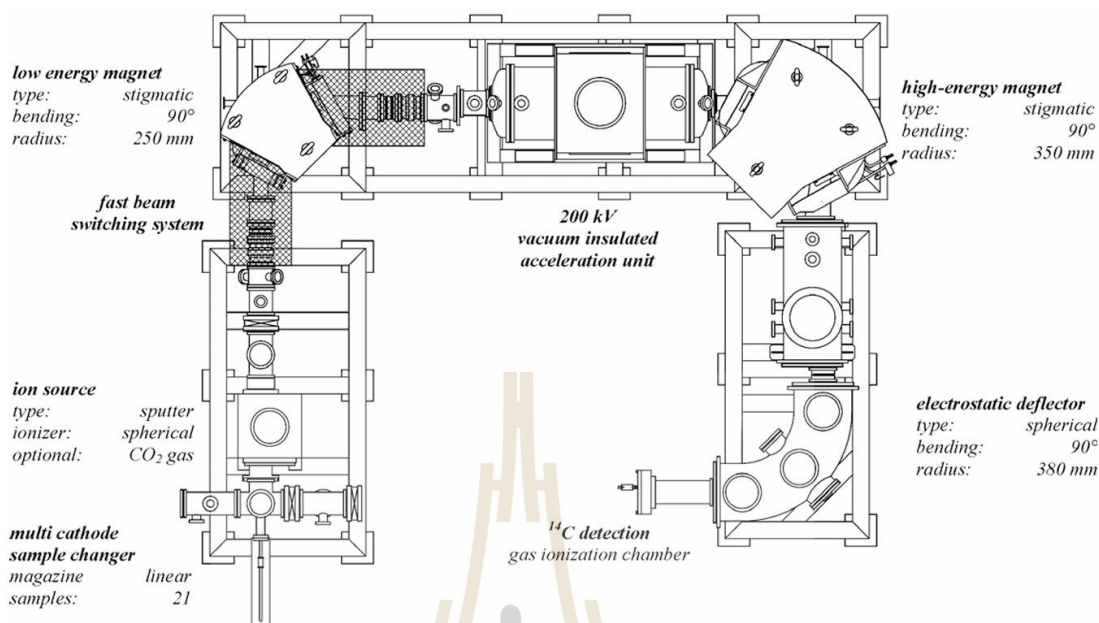


Figure 2.2 The layout of MICADAS. With its small dimensions of 2.5 x 3 m², can be easily fit into a common laboratory environment (H.-A. Synal et al., 2007).

The system as shown in Figure 2.2 operates at 200 kV, significantly reducing the size and complexity without compromising precision. These improvements have made AMS systems more accessible and affordable, allowing smaller laboratories and institutions to utilize the technology for applications in radiocarbon dating, environmental research, and archaeology.

In the sample preparation, the AMS system for radiocarbon dating requires the use of negative carbon ions, which are produced by the Source of Negative Ions by Cesium Sputtering (SNICS). This negative ion source designed for extracting negative carbon ions in graphite form by cesium sputtering. For this reason, there are various methods for the sample preparation and the compression method of graphite into the sample holder. The paper by Balsley et al. (1987) details methods for converting carbonaceous materials into solid graphite suitable for use in a cesium sputter ion source. Initially, carbon samples are converted to carbon dioxide, which is then reduced to graphite powder using hydrogen and iron as a catalyst. The graphite powder, or amorphous carbon, is encapsulated in a tantalum tube, compressed at high pressure (around 14 kbar), and heated to approximately 2500°C in a vacuum. This process ensures the formation of a smooth, hard graphite surface, which is ideal for producing high-intensity ion beams with good

geometrical characteristics. The preparation method emphasizes consistency, minimal contamination, and reproducibility, making it crucial for accurate AMS measurements. Moreover (Broek TAB, Roberts ML, 2024), the Ion Plus AG (MICADAS) demonstrated that recessed targets, particularly at a 1 mm depth, produced a more narrowly focused beam with lower emittance, improving transmission through the accelerator. Small graphite samples (200 μg) with recessed surfaces generated higher currents for longer periods, resulting in a 2–3X increase in ionization efficiency. Additionally, isotopic ratio measurements of these samples were more stable over time. Due to these benefits, the standard method for pressing MICADAS graphite has been updated to include a recessed surface approach.

2.3 Mini Carbon Dating System (MICADAS)

MICADAS is a highly compact and energy-efficient ^{14}C -AMS instrument designed for routine radiocarbon measurements. The heart of MICADAS is a hybrid cesium sputter ion source capable of producing stable negative-ion currents of 50–150 μA for solid graphite cathodes and 10–20 μA for gas samples ($\geq 10 \mu\text{g C}$). A random-access sample changer holds up to 40 graphite or gas cathodes, allowing continuous operation without breaking vacuum or cooling down the ion source.

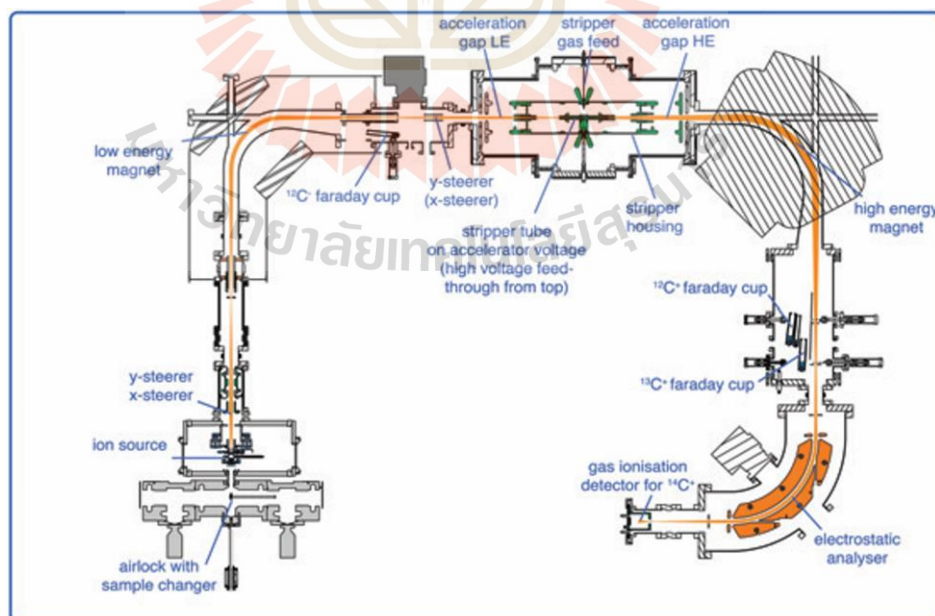


Figure 2.3 Simplified diagram of the ion optics of the MICADAS system. The high-voltage segment is shown in green (Synal et al., 2007).

Ion acceleration to 200 kV is provided by a vacuum-insulated solid-state power supply, eliminating the need for SF₆ or other insulating gases. Downstream of the accelerator, helium stripping yields up to 47 % transmission of ¹⁴C ions, with background levels (machine blanks) extending beyond 68,000 radiocarbon years. A low-noise gas ionization detector then identifies ¹⁴C ions with high reliability, enabling routine dating of samples older than 50,000 radiocarbon years.

Operation of MICADAS requires only 2.5 kW of average power and is fully air-cooled, so no water cooling is needed. The vacuum system including the ion source region, accelerator terminal, and analysis beamline must maintain pressures in the ultra-high vacuum (UHV) range (10⁻⁷ to 10⁻⁸ torr) to minimize scatter and background. Continuous monitoring of vacuum levels is achieved through integrated gauges, and automated vacuum interlocks protect both the ion source and the accelerator during sample changes or shutdowns.

Key specifications and operational conditions of MICADAS include:

- Ion source: Hybrid cesium negative-sputter, 40 position sample wheel
- Negative-ion currents: 50–150 µA (solid); 10–20 µA (gas, ≥10 µg C)
- Accelerator: 200 kV vacuum-insulated solid-state power supply
- Stripping medium: Helium (≤47 % ¹⁴C transmission)
- Detector: Gas ionization detector with low noise, enabling blank levels > 68,000 ¹⁴C yr BP
- Power consumption: ≤2.5 kW (air-cooled)
- Footprint: 3.2 m × 2.6 m × 2.2 m; weight ≈ 4,500 kg
- Sample throughput: Automated magazine changes allow continuous measurement without breaking vacuum.

By integrating all high-voltage components into a vacuum-insulated terminal and using permanent magnet technology, MICADAS minimizes infrastructure needs no SF₆ or water cooling is required and delivers fast tuning, long-term measurement stability, and minimal maintenance. This makes it particularly attractive for laboratories aiming to perform high-precision ¹⁴C dating with limited space and resources

2.4 Electrostatic deflector

The misalignment of the beamline components can cause the beam to deviate from the axis; therefore, an electrostatic deflector is required to correct the beam trajectory. This device utilizes electric fields to alter the path of charged particles. When ions pass through a region with an electric field, they experience a force proportional to the field strength and the charge of the ions. Electrostatic deflectors typically consist of parallel plates (Spivak-Lavrov et al., 2023) or electrodes with a voltage difference applied between them. Quadrupole deflectors are generally more suitable for applications requiring basic focusing and steering, where linear beam dynamics dominate. In contrast, octupole deflectors are advantageous in scenarios where the correction of non-linear effects is critical, such as in high-precision beam shaping and stability enhancement.

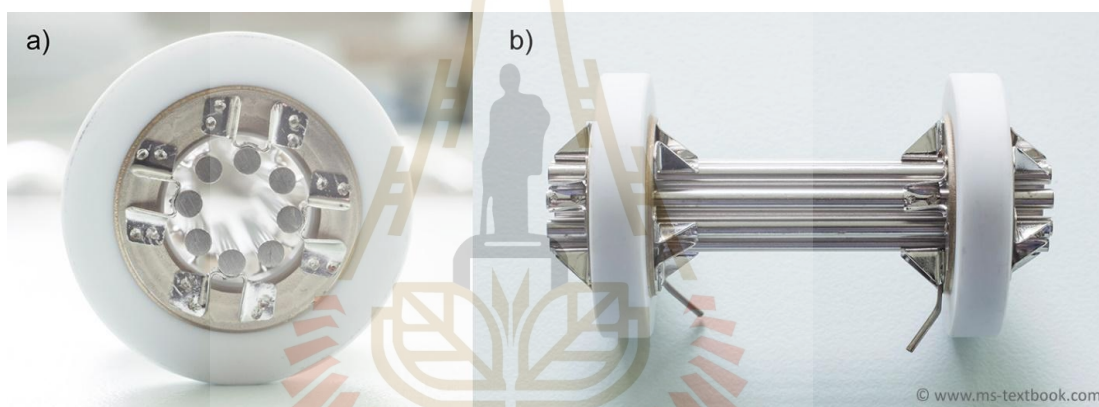


Figure 2.4 Octupole deflector: (a) Head-on view showing the octupole alignment, and (b) side view. Ref. MS-Textbook. (n.d.). For instructors.

Drummond, I. W. (1984) explains that an octupole is a type of multipole ion optical element consisting of eight rods or electrodes arranged symmetrically around the beam path. Its primary function is to apply corrective forces to ion beams, particularly in systems where beam shaping and the correction of higher-order aberrations are critical. Unlike simpler devices, such as quadrupoles, which correct second-order effects, the octupole addresses higher-order aberrations, making it useful for fine-tuning the beam's profile, especially in high-precision systems such as ion microscopy or mass spectrometry. By adjusting the voltages applied to the rods, the octupole compensates for distortions and imperfections in the beam, improving overall beam quality and stability. It is often used in combination with other optical elements, such as quadrupoles or Einzel lenses, to refine the beam shape and correct asymmetries in the beam trajectory.

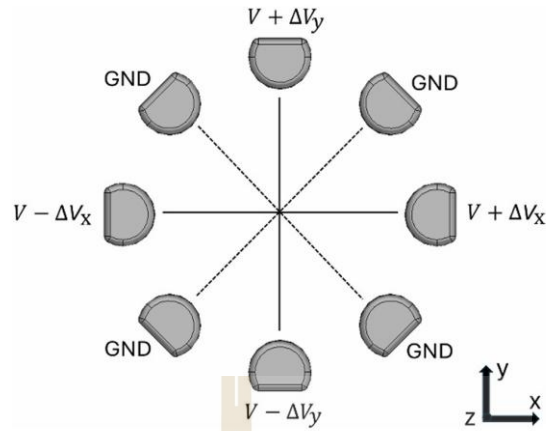


Figure 2.5 The schematic design of the octupole deflector (Chomchan et al., 2024).

The paper (Chomchan et al., 2024) designed and simulated a simple electrostatic octupole deflector intended for use in a compact AMS devoted to radiocarbon dating. The deflector is positioned immediately downstream of a cesium-sputter ion source and consists of eight stainless-steel rod electrodes arranged symmetrically in a 40 mm circular aperture. By biasing the horizontal and vertical electrode pairs independently (ΔV_x and ΔV_y), the authors demonstrated through finite-element electric-field analysis and charged-particle tracking (using CST Studio Suite) that the beam can be steered in the X and Y directions without cross-coupling.

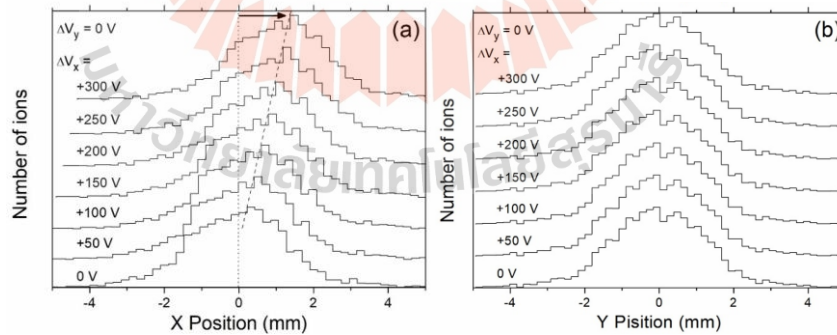


Figure 2.6 The horizontal (a) and vertical (b) profiles of a 40 keV C^- beam horizontally deflected with ΔV_y set to zero, while ΔV_x is varied from 0 to +300 V (Chomchan et al., 2024).

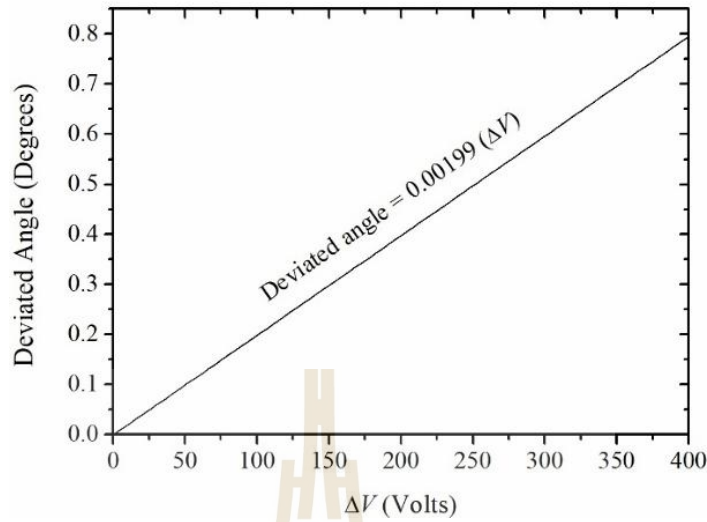


Figure 2.7 The simulated deviated angle of a 40 keV C^- beam after passing through the deflector as a function of ΔV (Chomchan et al., 2024).

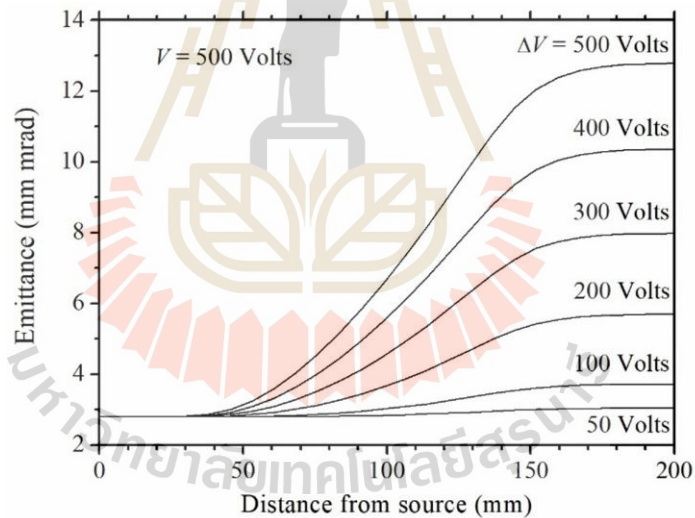


Figure 2.8 The emittance of the 40-keV C^- beam entering the deflector at 40 mm from source (Chomchan et al., 2024).

Simulations showed a linear relationship between the applied voltage difference and the beam's deflection angle, and that the emittance of a 40 keV C^- beam increases with larger deviation angles (e.g., from 2.9 mm·mrad unperturbed to approximately 6.0 mm·mrad at $\Delta V \approx 200$ V for a 0.4° deviation). These results confirm that beam deflections in the two directions are independent, with virtually no coupling. The emittance of the deviated beam increases with increasing deviated angle, thus the adjusting voltage.

2.5 Electrostatic lens

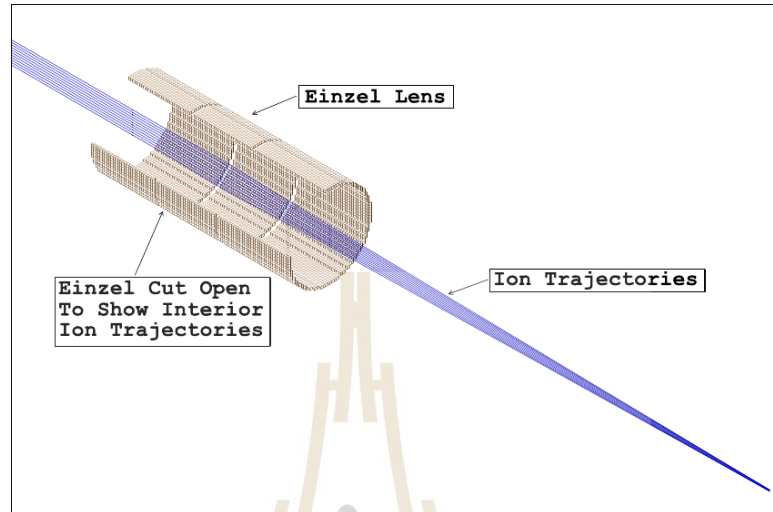


Figure 2.9 Cutaway view of ion trajectories in an Einzel lens. Ref. Scientific Instrument Services, Inc. (n.d.). SIMION: User Manual - Chapter 2: Ion Optics and Electrostatic Fields.

An Einzel lens is a type of electrostatic lens used in charged particle beam systems, such as ion and electron beamlines, to focus the beam without significantly altering its energy. It consists of three cylindrical electrodes, with the outer two typically grounded and the middle one held at a specific voltage. When a charged particle beam passes through the lens, the electrostatic field created by the potential difference causes the beam to focus by adjusting its trajectory. What makes the Einzel lens particularly useful is that it focuses the beam while maintaining the initial energy of the particles, making it ideal for applications where energy stability is crucial, such as AMS and other precision ion optics systems. Its simple design and effectiveness at controlling beam divergence and focusing make it a vital component in many particle accelerator setups.

Park et al. (2020) presents a simulation analysis of ion beam extraction using an electrostatic Einzel lens for low-energy AMS. The research focuses on optimizing beam focusing and separation in a compact AMS system. The SIMION program was used to simulate the ion trajectories, revealing that the use of an Einzel lens enhances the focusing and separation of ion beams, improving transmission efficiency.

The study evaluated the lens in two operational modes, accel-decel and decel-accel, as shown in Figure 2.11a and 2.11b and found that while both modes successfully transmitted the ion beam, they had different effects on beam emittance and isotopic separation. The decel-accel mode was found to be better suited for beam injection into an accelerating column or analyzing isotopic separation, while the accel-decel mode was more advantageous for other low-energy ion transport systems.

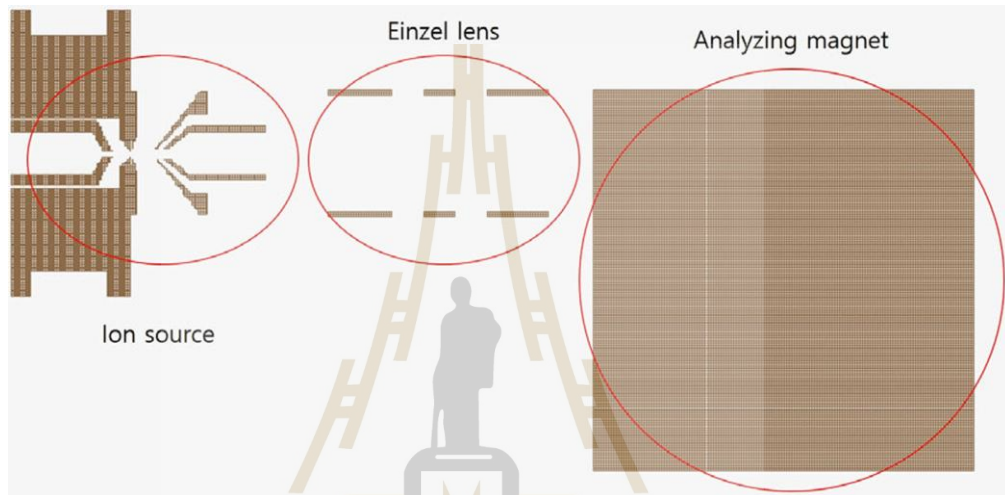


Figure 2.10 Geometry of the ion source, electrostatic Einzel lens, and analyzing magnet implemented via the SIMION code (Park et al., 2020).

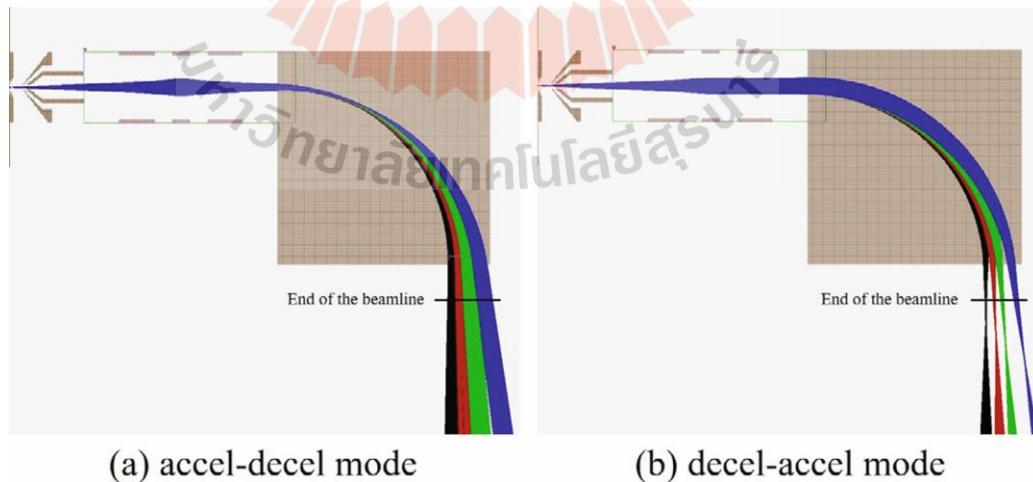


Figure 2.11 Simulation results for beam transmission in two different modes of the Einzel lens: (a) accel-decel mode and (b) decel-accel mode (Park et al., 2020).

Suethonglang et al. (2024) present the design and simulation of a compact electrostatic Einzel lens tailored for use in a low-energy (40 keV) carbon ion beamline within an AMS. The lens consists of three coaxial cylindrical electrodes, each with a 35 mm inner diameter, 3 mm wall thickness, and 17 mm axial gap, mounted inside a standard 4-inch vacuum tube. The two outer electrodes are held at ground potential, while the central electrode is biased either positively or negatively to generate the focusing field.

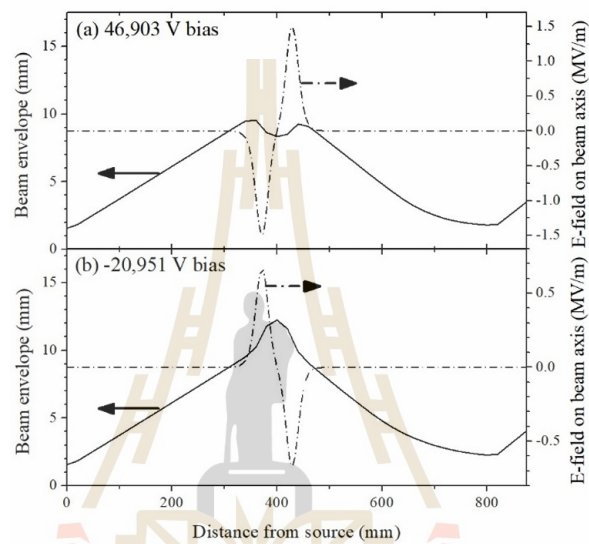


Figure 2.12 The ion beam envelope and electric field component on the beam axis beam when the electrostatic Einzel lens was biased with (a) 46,903 V and (b) -20,951 V (Suethonglang et al., 2024).

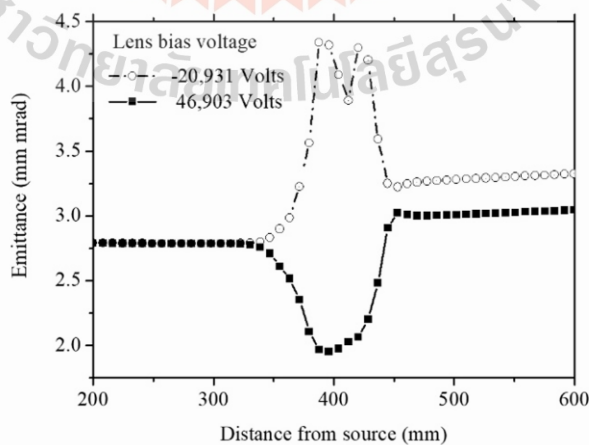


Figure 2.13 The emittance of the ion beam when the ES Einzel lens was biased with (a) 46,903 V and (b) -20,951 V (Suethonglang et al., 2024).

Using CST Studio Suite for particle-tracking simulations, the authors optimized the bias voltage and electrode dimensions. They found that a negative bias of $-20,951$ V on the middle electrode produced a tighter focus and lower emittance growth (an ~ 18 % increase from 2.8 mm·mrad to ~ 3.3 mm·mrad) compared to a positive bias of $+46,903$ V (where emittance rose to ~ 3.2 mm·mrad at the waist) as shown in Figure 2.13.

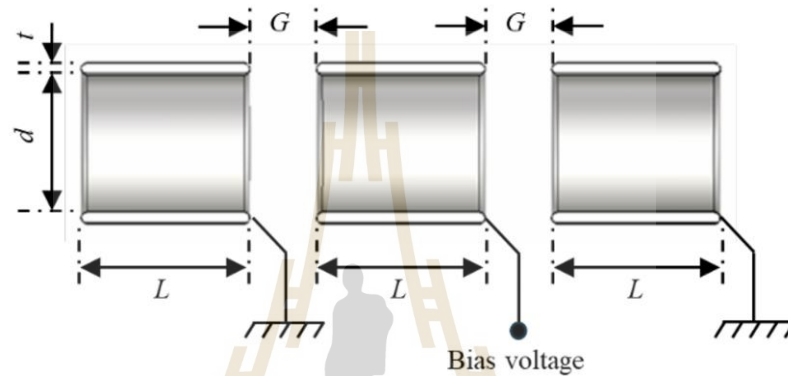


Figure 2.14 Cross-sectional drawing of an electro-static Einzel lens with three cylindrical tube electrodes (Suethonglang et al., 2024).

Moreover, by varying the length of the middle electrode from 43 mm to 86 mm, they demonstrated that the longer middle electrode minimized downstream emittance while still fitting within the 4 -inch chamber. Specifically, at twice the side-tube length (relative length = 2.0), beam emittance at the focus (800 mm from the ion source) was lowest (~ 3.15 mm·mrad) when the optimized negative bias ($\approx -21,500$ V) was applied. In conclusion, the optimized Einzel lens focuses a 40 keV C^- beam to a waist at 800 mm from the source with a demagnification factor of 1.0 and only a ~ 12.5 % emittance increase. This design combines high beam quality with practical high-voltage resilience, making it well-suited for a compact AMS system.

2.6 Heater for ionizer

For ion beam production inside the cesium sputter source, an ionizer is required to ionize the cesium vapor into cesium ions (Cs^+).

Table 2.1 Power Consumption of the Ionizer Heater at Different Temperatures (IonPlus AG) Ref. Cathode Engineering Co. (2023). HeatWave Labs AG Cesium-Sputter Ionizer Product Data Sheet.

Temperature (°C)	V (Volt)	Current (A)	Power (Watt)
1,000	6.16	12.22	72.28
1,110	7.8	14.06	109.67
1,210	9.5	15.8	150.1

2.6.2 Properties of MoRe alloy

MoRe (Molybdenum-Rhenium alloy) is commonly used as a filament material for the ionizer in cesium sputter sources due to its high melting point, excellent resistance to high temperatures, and stable electrical properties. It can withstand the high heat required for thermionic emission, making it ideal for generating electrons to ionize cesium in vacuum environments. Additionally, MoRe resists corrosion from cesium and maintains stability under vacuum conditions, ensuring long-lasting performance and reliable ionization efficiency. These properties make it an optimal choice for high-performance ion sources in sputtering applications.

Table 2.2 Mechanical, Physical, Electrical, and Thermal Properties of MoRe Alloy Ref. Rhenium.com. (n.d.). Molybdenum-Rhenium Alloy Annealed Properties.

Molybdenum–Rhenium Alloy, Annealed | MECHANICAL AND PHYSICAL PROPERTIES

	Metric	English
Physical Properties		
Density	13.5 g/cc	0.488 lb/in ³
Mechanical Properties		
Tensile Strength, Ultimate	1180 MPa	171000 psi
	240 MPa	34800 psi
	@Temperature 1200 °C	@Temperature 2190 °F
	620 MPa	89900 psi
	@Temperature 800 °C	@Temperature 1470 °F
Tensile Strength, Yield	845 MPa	123000 psi
	210 MPa	30500 psi
	@Temperature 1200 °C	@Temperature 2190 °F
	415 MPa	60200 psi
	@Temperature 800 °C	@Temperature 1470 °F
Elongation at Break	22%	22%
Modulus of Elasticity	365 GPa	52900 ksi
Poissons Ratio	0.285	0.285
Shear Modulus	132 GPa	19100 ksi
Electrical Properties		
Electrical Resistivity	0.0000220 ohm-cm	0.0000220 ohm-cm
Critical Superconducting Temperature	10.9 K	10.9 K
Thermal Properties		
CTE, linear	5.72 µm/m-°C	3.18 µin/in-°F
	@Temperature 500 °C	@Temperature 932 °F
	6.45 µm/m-°C	3.58 µin/in-°F
	@Temperature 1000 °C	@Temperature 1830 °F
Thermal Conductivity	36.8 W/m-K	255 BTU-in/hr-ft ² -°F
Melting Point	2450 °C	4440 °F
Maximum Service Temperature, Air	725 °C	1340 °F
Component Elements Properties		
Molybdenum, Mo	52.50%	52.50%
Rhenium, Re	47.50%	47.50%

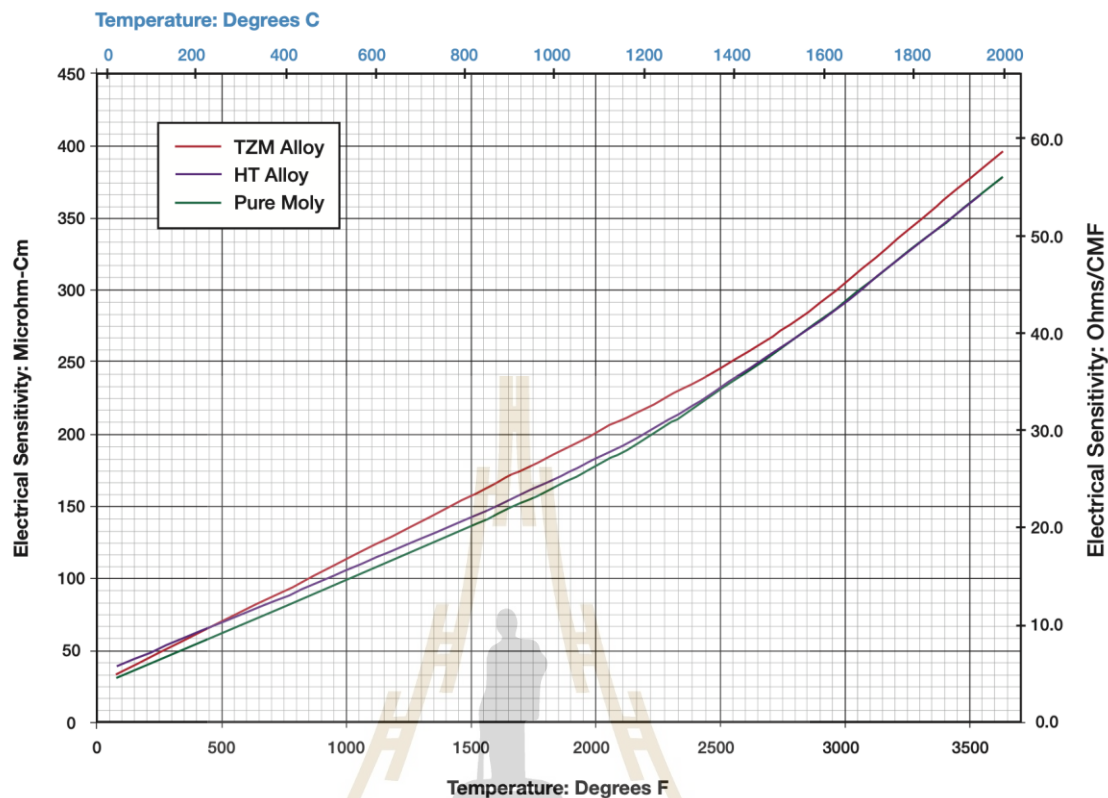


Figure 2.16 Electrical Resistivity of TZM Alloy, HT Alloy, and Pure Molybdenum vs. Temperature Ref. National Element Industries. (2017). Molybdenum Technical Data.

This Figure 2.16 shows how the electrical resistivity of three molybdenum-based materials TZM alloy (red), HT alloy (blue), and pure molybdenum (green) increase almost linearly with temperature from room temperature up to about 2,000 °F ($\approx 1,090$ °C). At 2,200 °F ($\approx 1,205$ °C), resistivity reaches roughly 200 $\mu\Omega\cdot\text{cm}$ (≈ 30 Ω/CMF) for all three, with TZM consistently exhibiting the highest values and pure molybdenum the lowest. The close spacing of the curves indicates that alloying with Ti, Zr, or heat treatments modifies resistivity only slightly across this temperature range. As the temperature of these molybdenum-based materials increases, their electrical resistivity rises accordingly because lattice vibrations (phonons) intensify, scattering conduction electrons more frequently and impeding their flow. As a result, at higher filament temperatures such as the 1,200 °C needed for cesium sputtering the ionizer heater's resistance will be significantly higher than at room temperature, requiring greater voltage or current to maintain the same power level.

2.7 Particle tracking solver in CST Studio Suite

Particle Tracking Solver is a submodule of Particle Studio that applies the Lorentz force law to fields computed from Maxwell's equations in this case via finite element analysis (FEA) to update particle positions and velocities over discrete time steps. First, CST's FEM or FIT field solvers perform FEA to solve Maxwell's equations and generate detailed electric and magnetic field maps throughout the geometry. The core equations used in CST Studio Suite's Particle Tracking Solver then couple the particle's equation of motion (the Lorentz force law) with those pre-computed FEA fields, allowing accurate tracking of charged particles through complex electromagnetic structures.

2.7.1 Finite element analysis

In CST Studio Suite, Finite Element Analysis (FEA) is primarily used to compute electromagnetic fields within complex geometries. The FEA solver automatically generates a high-quality tetrahedral mesh that conforms to the model's surfaces and internal features, with adaptive refinement in regions of high field gradient or geometric detail.

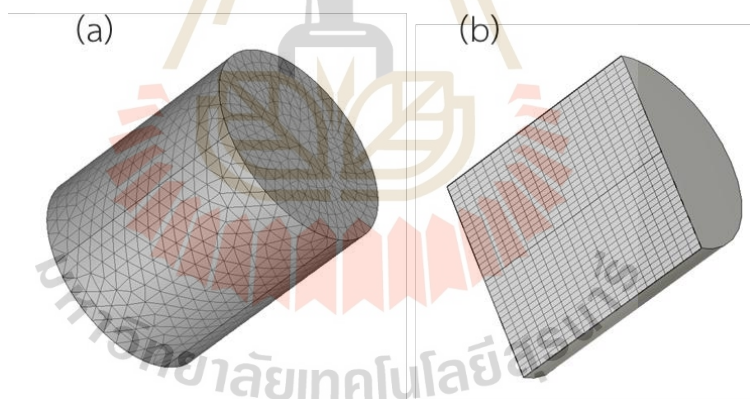


Figure 2.17 Mesh types for computer simulation. (a) Tetrahedral mesh (b) Hexahedral mesh.

Once the mesh is generated by CST's Mesher (via Mesh → Global Properties or Mesh View → Update), a static field solver discretizes Poisson's equation (together with material relations) on that mesh to produce an electrostatic (and, if required, magnetostatic) field map. This solver supports both hexahedral and tetrahedral grids. The resulting $\mathbf{E}(\mathbf{r})$ and $\mathbf{B}(\mathbf{r})$ distributions are then exported to Particle Studio's Tracking Solver, which integrates the Lorentz force law through these static fields—updating each particle's trajectory over time.

2.7.2 Equation of motion (Lorentz force law)

A charged particle with charge q and mass m moves according to the Lorentz force law:

$$\frac{d\mathbf{p}}{dt} = q(\mathbf{E} + \mathbf{v} \times \mathbf{B}) \quad \text{Eq. 1}$$

Where,

\mathbf{p} is the relativistic momentum of the particle,

$\mathbf{E}(\mathbf{r}, t)$ is the electric field at position \mathbf{r} and time t ,

$\mathbf{B}(\mathbf{r}, t)$ is the magnetic field at position \mathbf{r} and time t ,

\mathbf{v} is the particle's velocity.

For a relativistic particle, momentum is given by:

$$\mathbf{p} = \gamma m \mathbf{v}, \text{ with } \gamma = \frac{1}{\sqrt{1 - \frac{|\mathbf{v}|^2}{c^2}}} \quad \text{Eq. 2}$$

Thus, the full relativistic form of the equation of motion becomes:

$$\frac{d}{dt} (\gamma m \mathbf{v}) = q(\mathbf{E} + \mathbf{v} \times \mathbf{B}). \quad \text{Eq. 3}$$

The particle position is then updated by:

$$\frac{d\mathbf{r}}{dt} = \mathbf{v} \quad \text{Eq. 4}$$

2.7.3 Maxwell's equations

CST's Particle Tracking Solver first computes \mathbf{E} and \mathbf{B} throughout the simulation domain by solving Maxwell's equations (in differential form) using the Finite Integration Technique (FIT):

2.7.3.1 Gauss's law (Electric)

$$\nabla \cdot \mathbf{D} = \rho, \text{ where } \mathbf{D} = \epsilon \mathbf{E} \quad \text{Eq. 5}$$

2.7.3.2 Gauss's law for magnetism

$$\nabla \cdot \mathbf{B} = 0, \text{ where } \mathbf{B} = \mu \mathbf{H} \quad \text{Eq. 6}$$

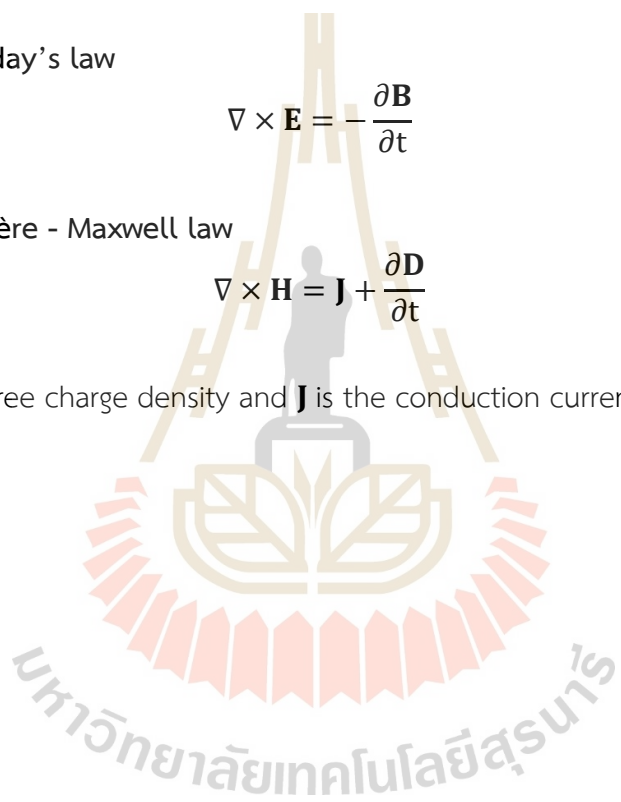
2.7.3.3 Faraday's law

$$\nabla \times \mathbf{E} = -\frac{\partial \mathbf{B}}{\partial t} \quad \text{Eq. 7}$$

2.7.3.4 Ampère - Maxwell law

$$\nabla \times \mathbf{H} = \mathbf{J} + \frac{\partial \mathbf{D}}{\partial t} \quad \text{Eq. 8}$$

Where ρ is the free charge density and \mathbf{J} is the conduction current density.



CHAPTER III

RESEARCH METHODOLOGY

The research methodology is divided into three sections. The first section covers computer simulations performed in CST Studio Suite, detailing each step of the simulation process. The second section addresses the design and placement of vacuum components, including leak checking of the vacuum chamber to ensure operational readiness and positioning the power supplies beneath the beamline to achieve a compact system layout. The third section presents the development and design of the ionizer heater.

3.1 Simulation using CST Studio Suite

This section presents the computer simulations carried out with CST Studio Suite. Simple 3D geometries were generated directly in CST, while more complex 3D models were created in SolidWorks by an engineer from NARIT.

3.1.1 Particle tracking simulation

In the CST workflow, the Particle Tracking Solver module is used. It is essential to select an appropriate mesh type and sufficient mesh density to ensure that simulation results are both reliable and accurate, while avoiding unnecessary consumption of computational resources. The flow chart of the simulation process is shown in Figure 3.1.

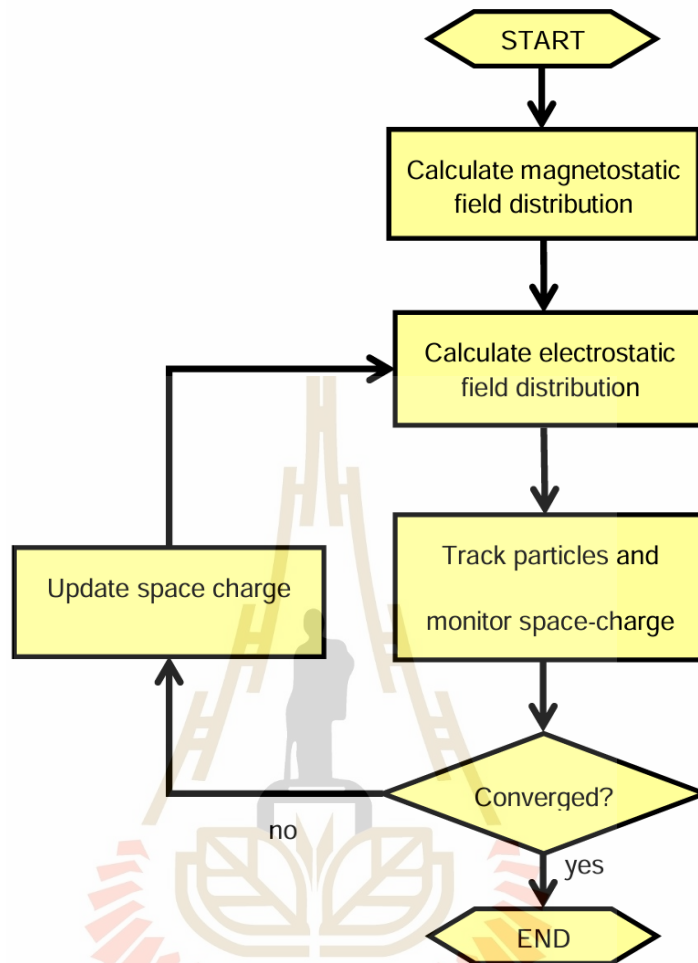


Figure 3.1 Flow chart of particle tracking simulation in CST Studio Suite.

3.1.1.1 Mesh refinement

In the Particle Tracking Solver module, a hexahedral mesh (brick cells) is employed to track particle trajectories through the electric fields computed from Maxwell's equations. Local mesh refinement is applied, as shown in Figure 3.2, along the ion beam path and in regions with high field gradients—such as around the emission surface and at electrode edges—to increase mesh density where it is most critical. A convergence study is then conducted to determine the optimal cell size. This strategy ensures that accurate particle tracking results are achieved while minimizing the use of computational resources.

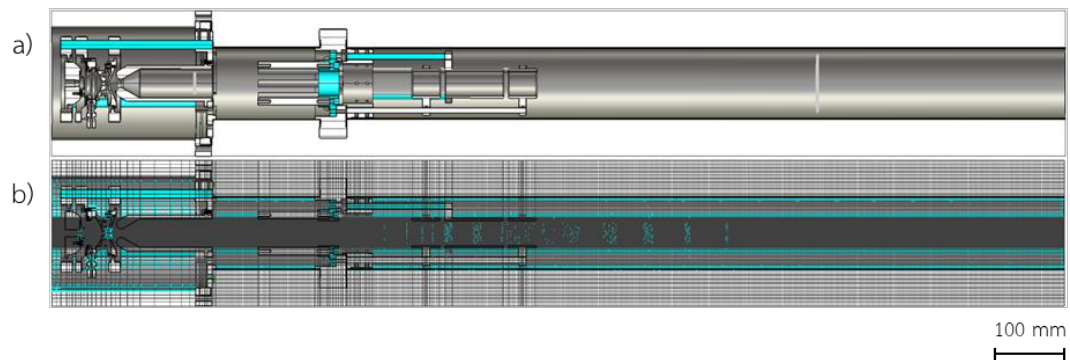


Figure 3.2 Mesh Generation for the particle tracking solver module in CST Studio Suite. a) The negative carbon ion beamline model used for simulation. b) The same model after applying local hexahedral mesh refinement along the ion beam path, from the ion source to the aperture slit at the end of the beamline.

3.1.1.2 Convergence study

In the simulation workflow, a convergence study was conducted to ensure that key beam parameters, such as emittance and the beam envelope, remained invariant with respect to increasing mesh density. Starting from a baseline hexahedral mesh size, the global mesh was systematically refined by varying the parameter N_mesh , as shown in Figure 3.3, which represents the number of cells per maximum model box edge.

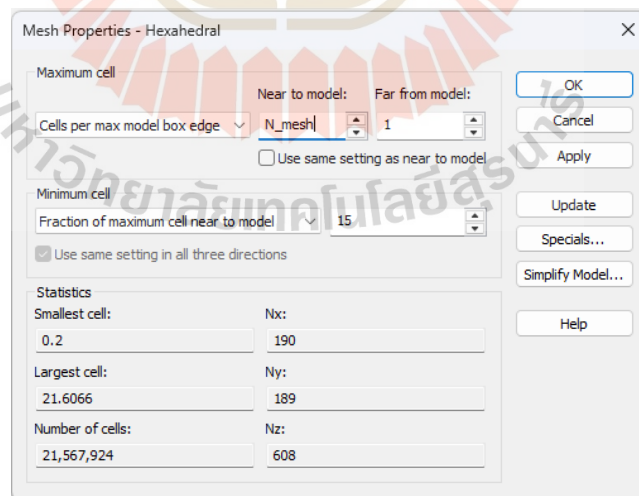


Figure 3.3 The global mesh settings, where the N_mesh variable is defined in the mesh properties, are used with the parameter-sweep function to perform the convergence study.

The convergence study was initiated with $N_{\text{mesh}} = 20$ and incremented by 20 up to 200, as shown in Figure 3.4, with local refinements introduced around high-gradient regions and along the ion beam path. At each refinement step, a parameter-sweep function was employed to iteratively increase N_{mesh} and to position particle monitors along the beam axis.

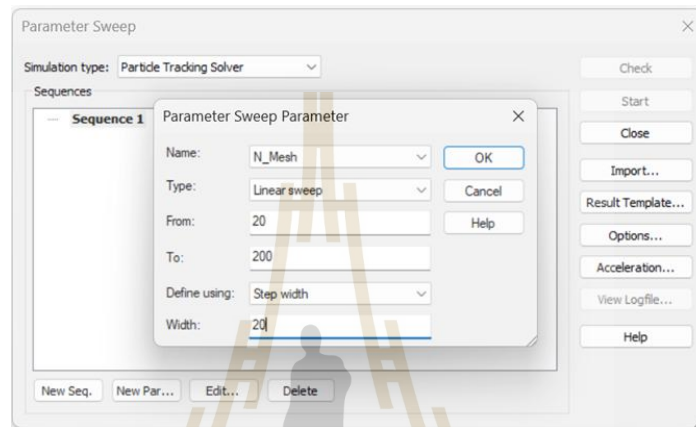


Figure 3.4 In the parameter sweep function, the N_{mesh} variable is swept from 20 to 200 in steps of 20, yielding 10 values (20, 40, 60, ..., 200) and progressively increasing the mesh density.

The Particle Tracking Solver was then executed, and the beam parameters were recorded. Convergence was considered achieved when successive refinements resulted in changes of less than 1 % in all monitored parameters. This threshold is widely accepted in fields employing Field/PIC/FEM techniques, as it represents a practical balance between high accuracy and manageable computational cost. This process not only ensures that the results are free from artifacts caused by mesh coarseness or insufficient particle sampling but also identifies the optimal balance between computational efficiency and accuracy, thereby enhancing both the reliability and effectiveness of the simulation methodology.

3.1.1.3 Transfer source via define particle export interface

In the simulation of the negative carbon ion beamline, multiple sequential components—ion source, octupole deflector, Einzel lens, and aperture slit—are modeled. To conserve computational resources and reduce simulation time, the particle export interface (shown in Figure 3.5) is employed to transfer the output of one optical element as the input source for the next.

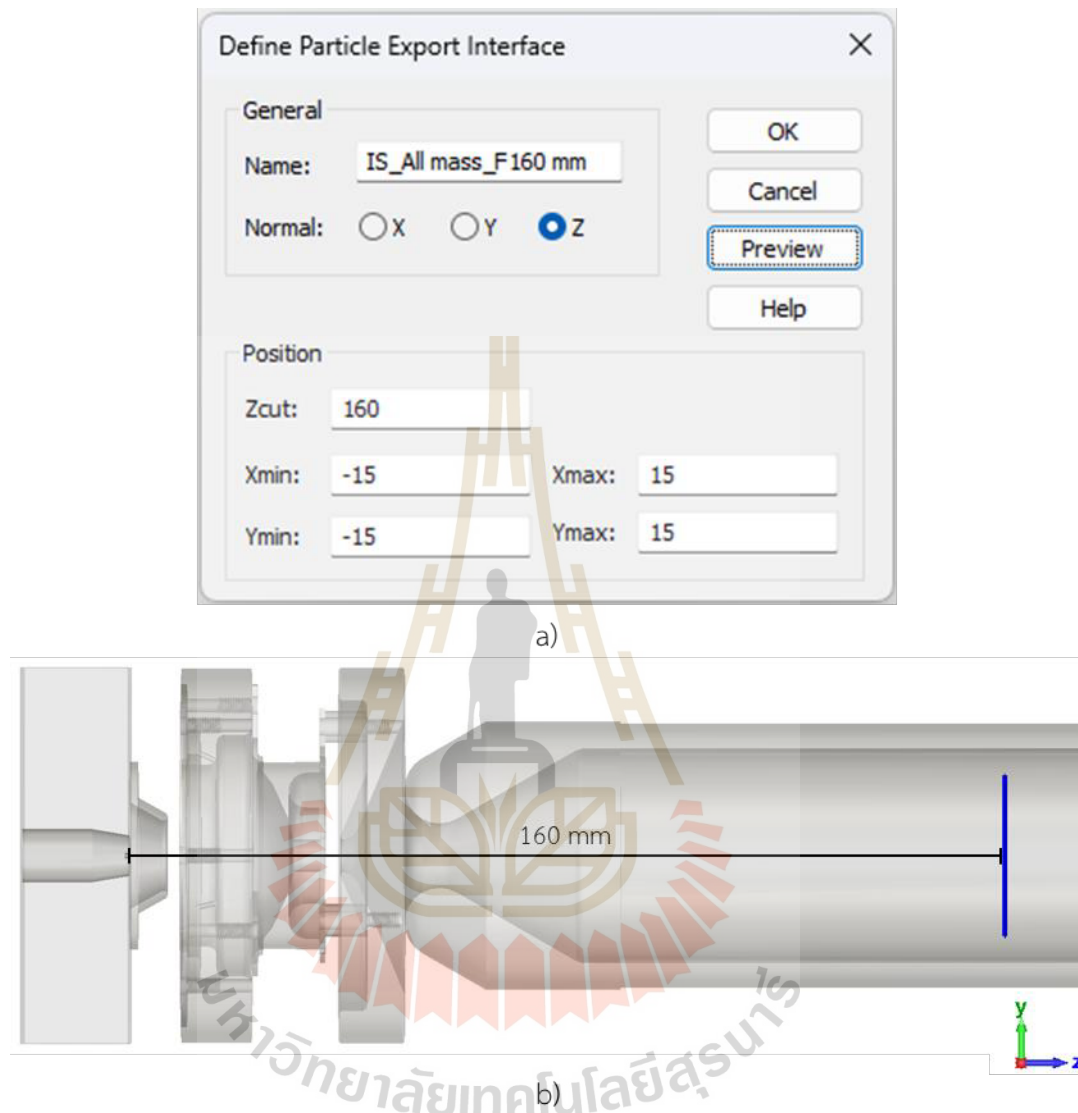


Figure 3.5 Defining the particle export interface. a) Boundary and position setup for particle export at the ion focus point, located 160 mm from the emission point; the boundary plane is sized larger than the beam envelope. b) Example of the particle export interface (blue plane) defined for the ion source, using the known focal position of the ion beam.

Specifically, the particle interface is exported at the focal point of the first element (e.g., the ion source) and then imported as the starting beam for the subsequent element (octupole deflector, followed by the Einzel lens, etc.). This chaining approach ensures an efficient and accurate end-to-end beamline simulation.

3.1.2 Ion source simulation

Since Saengwises et al. (2024) have already optimized the ion source model for a cesium-sputter AMS source, our simulation defines a particle source comprising ^{12}C , ^{13}C , and ^{14}C ions. Each ion carries a charge of $-1.6 \times 10^{-19} \text{ C}$ and has a mass of 12 amu, 13 amu, and 14 amu, respectively, for a total of 118,803 particles. This particle count corresponds to the emission density specified in CST.

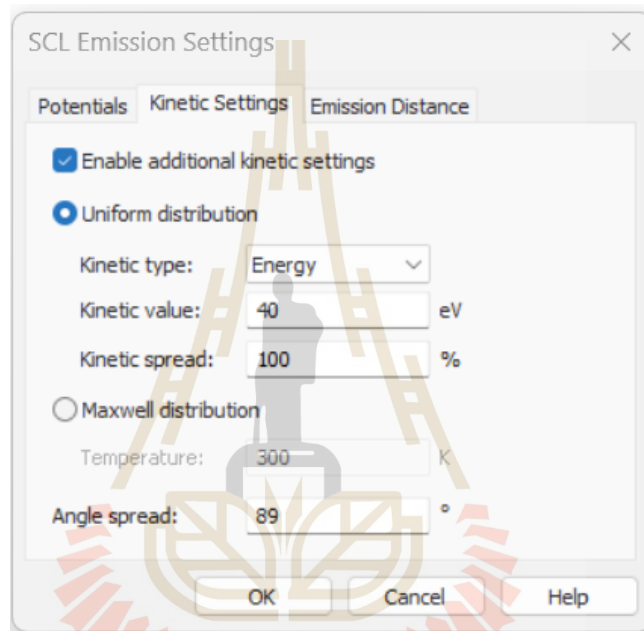


Figure 3.6 Setting the kinetic energy and angular spread of the particle sources to model the effects of HVPS ripple and the sputtering process respectively.

The requirement for generating the necessary electric field inside the ion source was addressed by applying a 40 kV potential difference using a high-voltage power supply (HVPS). Consideration was also given to the ripple, defined as the residual fluctuations on the DC output caused by imperfect filtering in the power circuit (Matsusada Precision Inc., 2023). The selected HVPS for the ion source exhibits a ripple of less than 0.1 % peak-to-peak. In CST, this required setting the source's kinetic energy spread to 40 eV (as shown in Figure 3.6) and defining an angular spread for the particle source to simulate the sputtering process, which emits negative carbon ions in all directions from the sample target. Due to CST's limitation in modeling a full 90° spread, the angular spread was set to 89° .

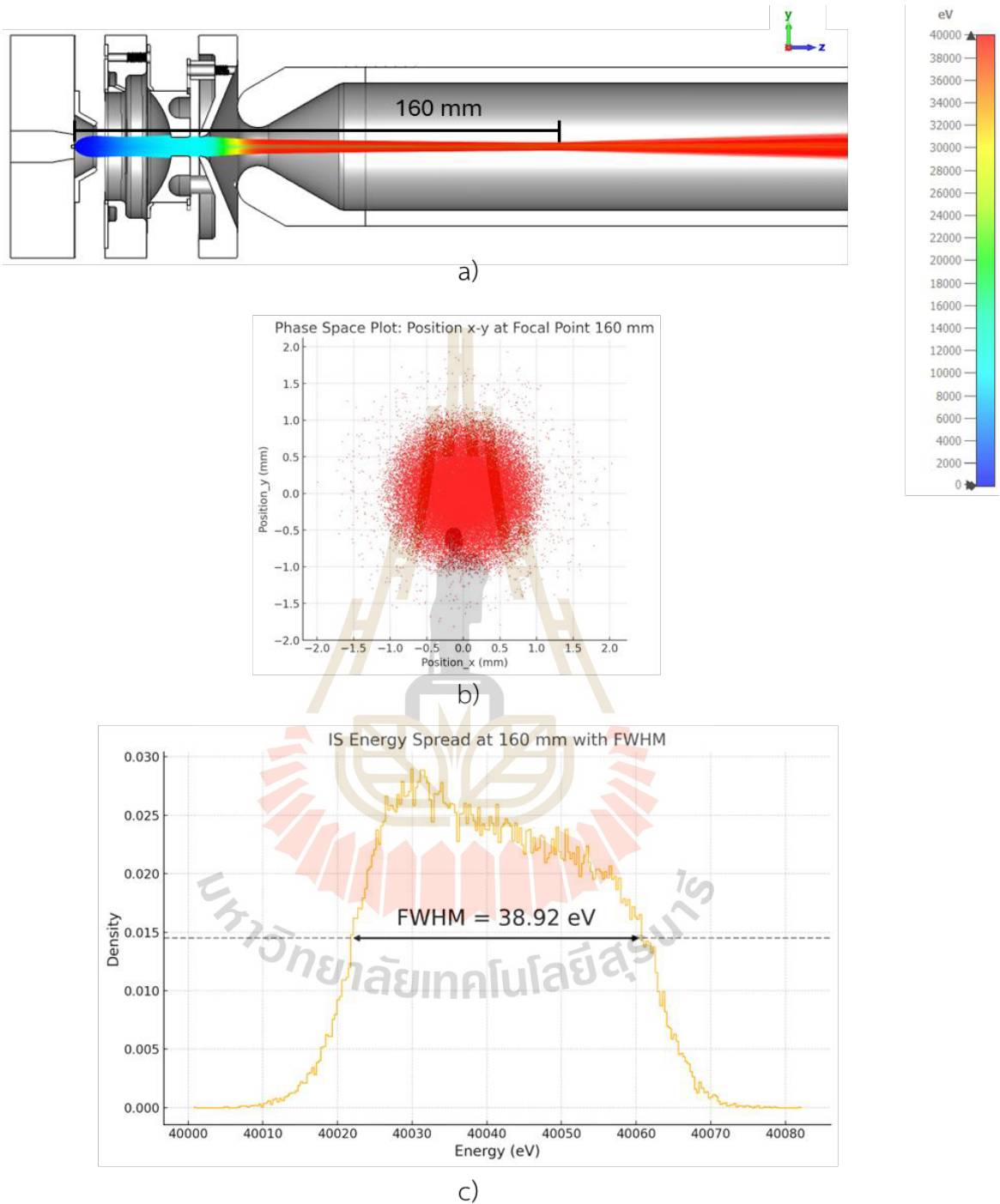


Figure 3.7 Simulation results of the ion source a) Trajectories of ^{12}C , ^{13}C , and ^{14}C ions focused at 160 mm from the source. b) Particle distribution image at the focal point. c) Energy spreads at the focal point.

The simulation of the ion source, as shown in Figure 3.7, yielded 68,442 ions exiting the source, corresponding to a 58 % transmission. The 89° angular spread produces a larger beam that collides with the ionizer, causing particle loss. This is consistent with the actual ionizer wear marks shown in Figure 3.8. At the focal point, 160 mm from the source, the beam emittance was calculated to be 3.5 mm·mrad.



Figure 3.8 Comparison of a new ionizer (left) and a used ionizer (right), showing burn marks at the center caused by sputtered ions spreading in all directions and striking the surface Ref. Purdue University Prime Lab. (n.d.). Ionizer.

3.1.3 The study of miss alignment of the octupole deflector

During the fabrication and assembly of the actual components, misalignments—such as tilt and offset of the electrodes along the optical axis (z-axis) following the ion source—are inevitable. To define acceptable assembly tolerances, these errors were simulated. Based on the capabilities of the available alignment tools, the maximum expected offset is 1 mm, and the maximum tilt angle is 2° . In the simulation shown in Figure 3.9, two parameters were varied: the tilt angle (θ) at 0° , 0.5° , 1° , 1.5° , and 2° , and the offset of the octupole deflector along the y-axis at 0, 0.5, 1, 1.5, and 2 mm. The

objective was to determine the maximum tilt and offset that still allow the ion beam to be correctly focused at the aperture slit.

The power supply chosen for operating the octupole deflector (Matsusada Precision Inc., 2023) delivers up to 1 kV to every other rod, with the remaining four rods held at ground potential.

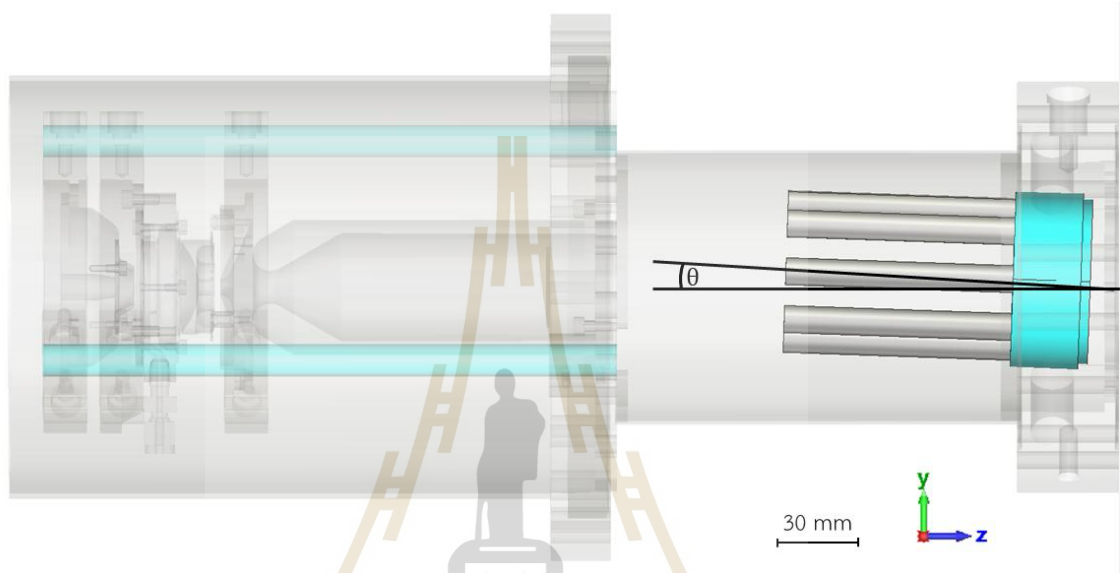


Figure 3.9 The octupole deflector model has rods each 10 mm in diameter and a total inner diameter of 40 mm, matching the dimensions from Figure 2.5 (Chomchan et al., 2024). This model was used to study tilt angles (θ) of 0°, 0.5°, 1°, 1.5°, and 2°, and offsets achieved by translating the entire octupole component along the positive y-axis by 0, 0.5, 1, 1.5, and 2 mm. The insulator segment is shown in blue.

In the simulation, two parameters—tilt angle and offset along the y-axis (offset_y)—were varied across five values each, resulting in a total of 25 parameter combinations. For each case, the particle monitor image placed at the aperture slit was examined to determine whether the beam remained focused and successfully passed through the slit. The aperture slit consists of four blades, each independently adjustable along the $\pm x$ and $\pm y$ axes. These blades can be fully opened to form a maximum square aperture of $20 \times 20 \text{ mm}^2$ or closed completely, as shown in Figure 3.10.

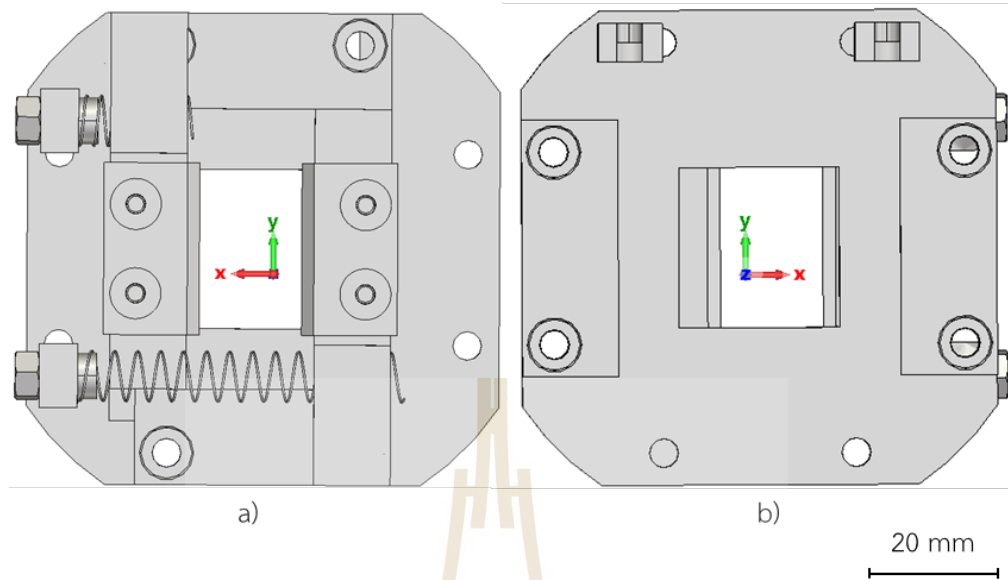


Figure 3.10 The aperture slit design consists of four independently adjustable blades, each movable along the $\pm x$ and $\pm y$ axes, allowing a maximum square opening of $20 \times 20 \text{ mm}^2$ or complete closure. Each blade also serves as a current collector to measure and monitor the ion beam. a) Upstream side b) Downstream side.

3.1.4 Einzel lens simulation

The optical element downstream of the octupole deflector is an Einzel lens, which consists of three coaxial cylindrical electrodes with a 35 mm inner diameter and 3 mm wall thickness, as described by Suethonglang et al. (2024). The first and third electrodes are held at ground potential, while the central electrode is driven by a high-voltage power supply (Matsusada Precision Inc., 2023) providing a negative bias of up to 30 kV. The function of this Einzel lens is to focus the ion beam onto the aperture slit.

3.1.4.1 The study of effects from mounting support

The impact of the mounting supports on the ion beam was studied by including both the mounting support rods and the Einzel lens in the simulations. Although this approach increases computational resource usage and simulation time, it provides more accurate and realistic results. The Einzel lens consists of three coaxial cylinders with gaps between them, as shown in Figure 3.11.

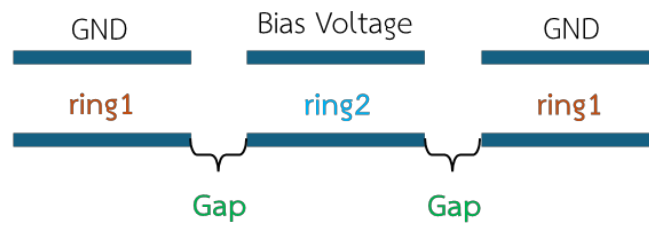


Figure 3.11 The ratio of the Einzel lens lengths (ring1 : gap : ring2).

Conductive stainless-steel support rods passing alongside the gaps between the electrodes can perturb the electric field and consequently affect the ion beam. To evaluate this effect, two models with different ring-to-gap ratios were analyzed. Model 1 employs a ratio of 43 : 21 : 64 mm (Figure 3.12), while Model 2 uses a ratio of 40 : 6 : 82 mm (Figure 3.13).

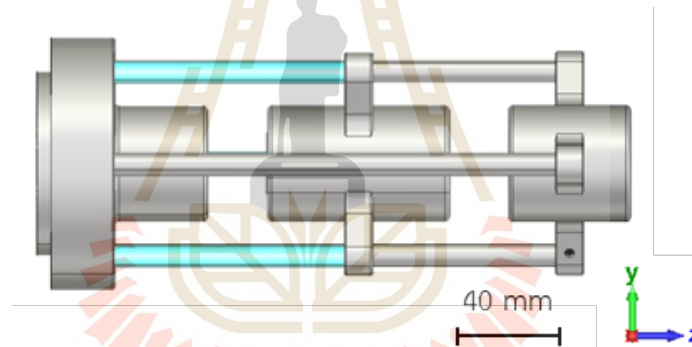


Figure 3.12 The Einzel lens model 1 (43 : 21 : 64 mm)

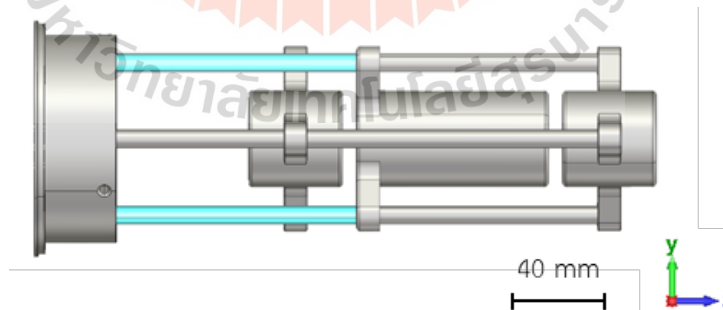


Figure 3.13 The Einzel lens model 2 (40 : 6 : 82 mm)

In the simulations, the particle source from the ion source was imported using the Particle Import Interface. The beam shape at the focal plane was then examined while a -20 kV bias was applied to the Einzel lens, and the electric field distribution near the support rods was observed.

3.1.4.2 The study of focal range

After the improved Einzel lens model was finalized, the optimizer function in CST was used to vary the applied potential to ensure that the ion beam focused at 476 mm from the Einzel lens—the position of the aperture slit. The optimization variable, V_{Einzel} , was defined as the bias voltage on the Einzel lens and was varied by the solver from 0 V to -30,000 V (Figure 3.14a). The optimization goal (Figure 3.14b) was to minimize $rms(position_x)$ at the focal point, where $rms(position_x)$ represents the root-mean-square of the particle positions.

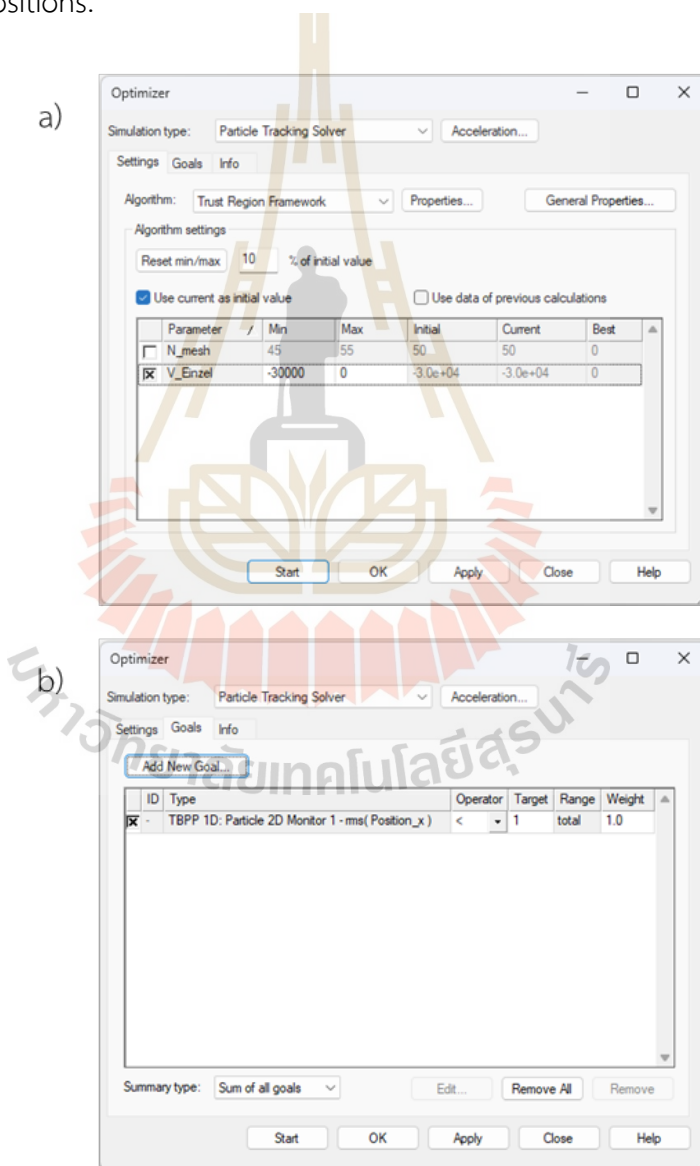


Figure 3.14 Optimizer Function Settings in CST Studio Suite a) Definition of variables and their ranges for the solver to vary. b) Specification of the optimization goals.

3.1.4.3 The study of miss alignment

When the actual components are fabricated and assembled, the Einzel lens aligned downstream of the octupole deflector shares mounting supports on a CF152 vacuum-chamber flange (shown as the leftmost electrode in Figure 3.15). During alignment, some degree of tilt or offset error is inevitable.

Simulations were therefore performed to specify the allowable assembly tolerances. Engineers defined the maximum expected alignment errors as a 1 mm offset and a 2° tilt. In the simulations (Figure 3.15), two parameters were varied: the tilt angle (θ) at 0° , 0.2° , 0.4° , 0.6° , 0.8° , 1.0° , 1.2° , 1.4° , and 1.6° , and the y-axis offset of the middle electrode by translating it 0, 0.2, 0.4, 0.6, 0.8, 1.0, 1.2, 1.4, and 1.6 mm along the positive y-axis. The focus was placed on the middle-ring electrode, as it is most susceptible to alignment errors due to its support rod being made of an alumina insulator (shown in Figure 3.12b, blue electrode), which is less rigid than the stainless-steel rods used for rings 1 and 3. For each parameter combination, the particle-monitor image at the aperture slit was examined to determine whether the beam remained focused on and successfully passed through the slit.

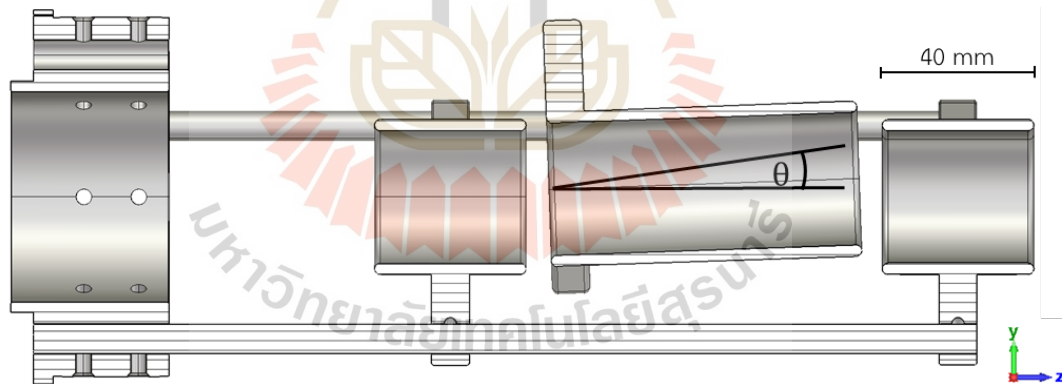


Figure 3.15 The cross section of Einzel lens design includes mounting supports (shown on the leftmost side) shared with the octupole deflector.

3.1.5 Low-energy negative carbon ion beamline simulation

In assembling the fully integrated system—which comprises the ion source, octupole deflector, Einzel lens, and aperture slit as primary components, along with various mounting supports inside the vacuum chamber—the CST model is simplified by omitting nonessential details such as vacuum pumps, chamber fittings, screws, and other hardware, as shown in Figure 3.16a. This simplification reduces computational load and simulation time. The model is then focused on the ion beam path and only those support structures likely to perturb the electric field (Figure 3.16b). Before initiating the simulation, the mesh is defined and a convergence study is performed to determine the optimal mesh density.

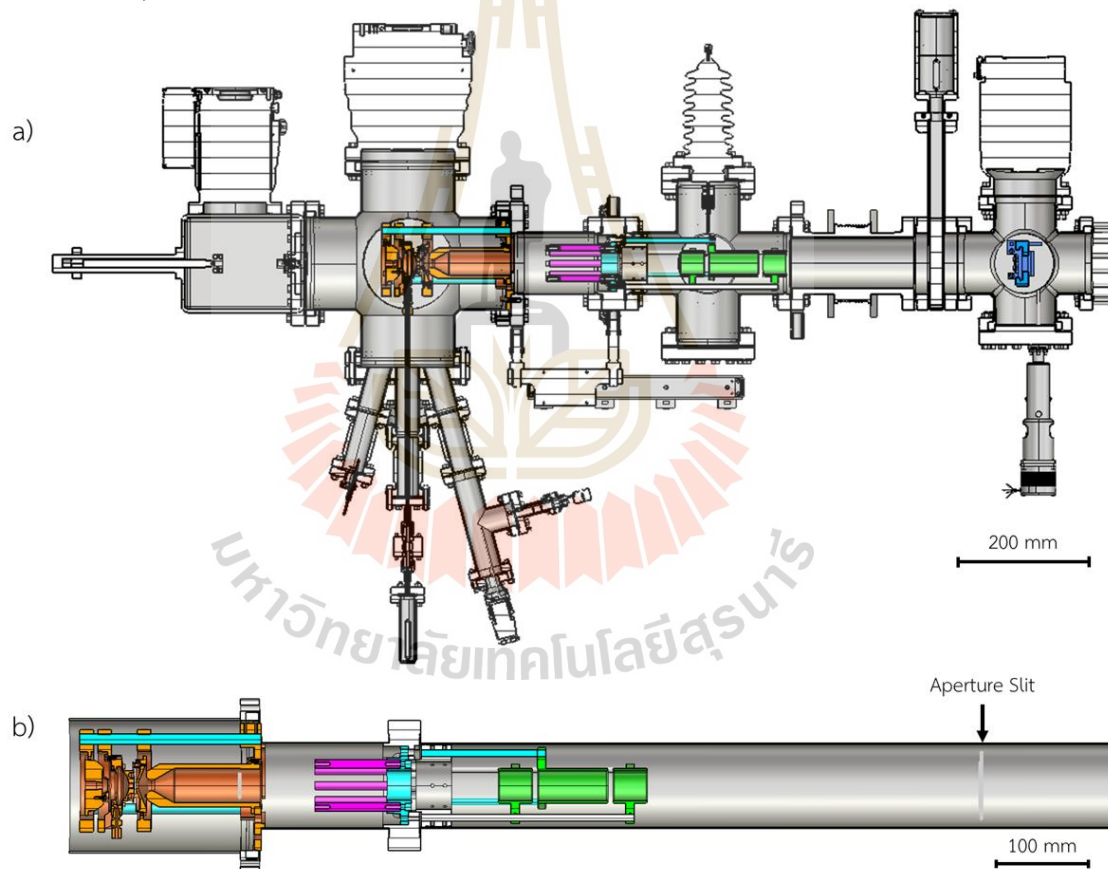


Figure 3.16 The cross-section of the low-energy negative carbon ion beamline shows the details and positions of the main components: the ion source (orange), the octupole deflector (pink), the Einzel lens (green), and the aperture slit (blue). The insulator segment is also highlighted. a) Beamline with external details. b) Simplified beamline model for particle-tracking simulation in CST.

In simulating the full system, the source was first defined using the Particle Import Interface to transfer the particle distribution at the ion source focus to subsequent stages, thereby reducing simulation time. The optimized bias voltage was then applied to the Einzel lens by setting V_{Einzel} to -2.01×10^4 volts, as determined from the focal-range study. This simulation represents an ideal case with perfect, systematic alignment. The beam size and emittance were examined along the entire optical axis and at the aperture slit using the Particle 2D Monitor function. Specifically, Monitor 1 was placed at the aperture slit, and 100 additional monitors (Monitor 2) were distributed from the ion source focal point through and slightly beyond the slit, as shown in Figure 3.17a. Post-processing was subsequently employed to analyze rms(position), beam envelope, beam image, and emittance, as illustrated in Figure 3.17b.

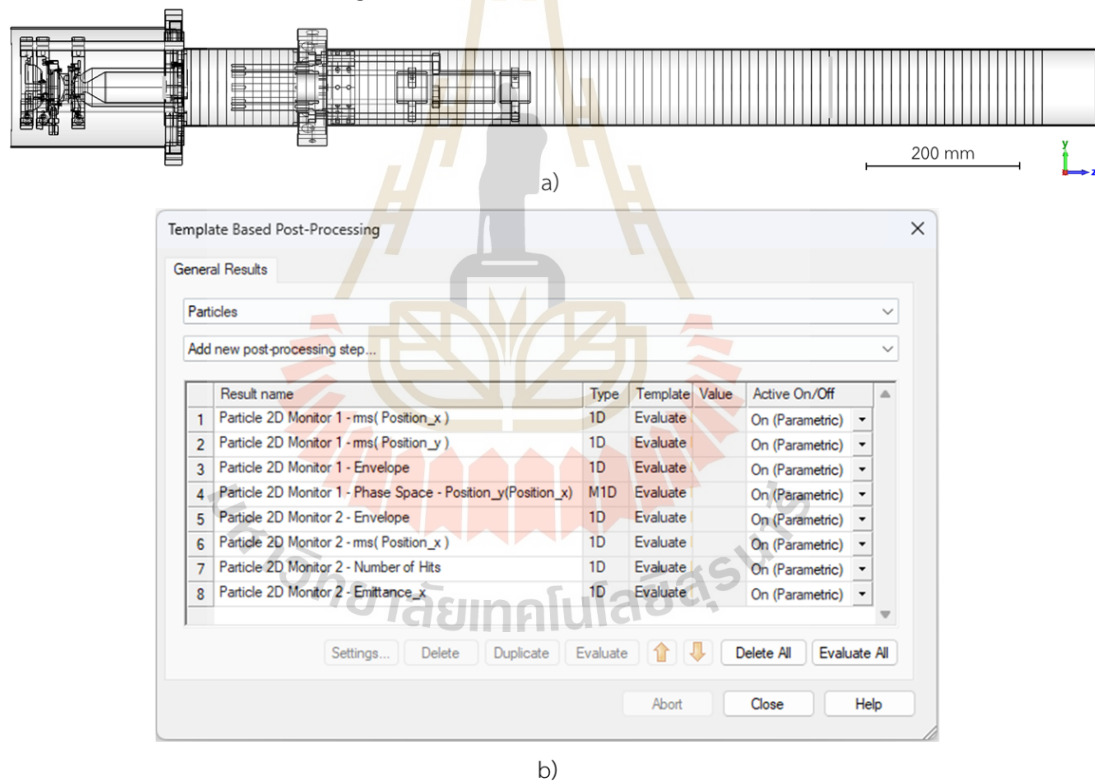


Figure 3.17 Analysis of the ion beam using particle monitors. a) The 101 monitors spanning from the ion source focal point through and slightly beyond the aperture slit, including Monitor 1 at the slit and Monitor 2 along the beam path. b) Template based post processing showing the results as the ion beam passes each monitor.

3.2 Low-energy beamline design

For the operation of the AMS, the system must function under vacuum conditions. The vacuum system maintains an ultra-high vacuum environment, typically in the range of 10^{-6} to 10^{-9} Torr, which is essential for minimizing collisions between ions and residual gas molecules. To reduce procurement and manufacturing costs, existing vacuum components from SLRI's unused equipment inventory were selected, inspected, and prepared for vacuum operation before being assembled into the system layout. Assembly drawings were created in SolidWorks through collaboration with engineers from NARIT. For beamline sections requiring high-voltage operation, power supplies from Matsusada Precision Inc. were selected to match the specifications of each component. Finally, the power supplies were positioned beneath the beamline to achieve a compact system design.

3.2.1 Vacuum system

3.2.1.1 Existing vacuum components at SLRI

- 6-Ways Cross Chamber, 8" OD, Sphere Body 9" for ion source chamber



Figure 3.18 6-Ways Cross Chamber, 8" OD, Sphere Body 9 inch.

- Adapter CF203 to CF152 for octupole deflector

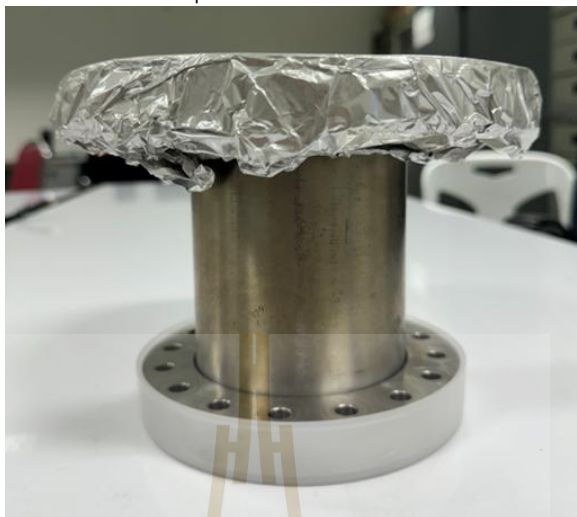


Figure 3.19 Adapter CF203 to CF152.

- 6-Ways Cross Chamber, 6" OD size 270 mm for Einzel lens



Figure 3.20 6-Ways Cross Chamber, 6" OD size 270 mm

- 6-Ways Cross Chamber, 6" OD size 220 mm for aperture slit.



Figure 3.21 6-Ways Cross Chamber, 6" OD size 220 mm

- Edge Weld Bellow CF152 and alignment studs for vacuum chamber extension.



Figure 3.22 Edge weld bellow and alignment studs.

- Vacuum Gate Valve (CF152) for isolating vacuum sections

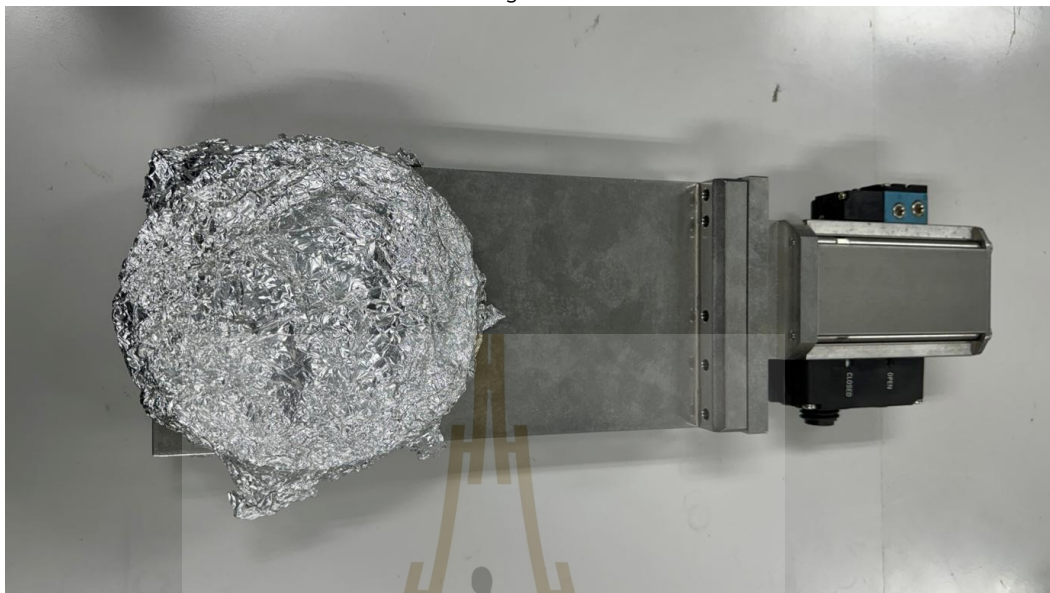


Figure 3.23 Vacuum gate valve

- Glass view port CF34, CF70, CF114 and CF152



Figure 3.24 Glass view port

3.2.1.2 Leak checking by helium detector

To prepare the vacuum chamber for operation, existing components from SLRI were cleaned, assembled, and tested for leaks. A Pfeiffer Adixen ASM 340 leak detector was used to verify vacuum integrity, and a reusable Viton gasket was chosen for sealing. Helium was applied to check for leaks, with a leak rate below 1×10^{-8} mbar·L/s indicating readiness for use.

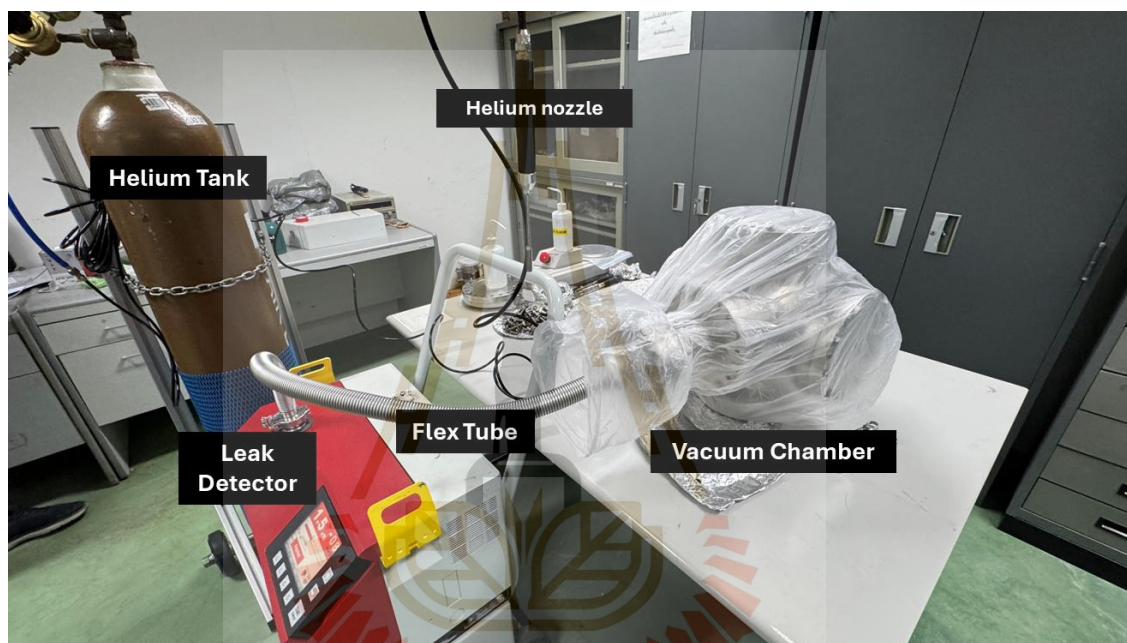
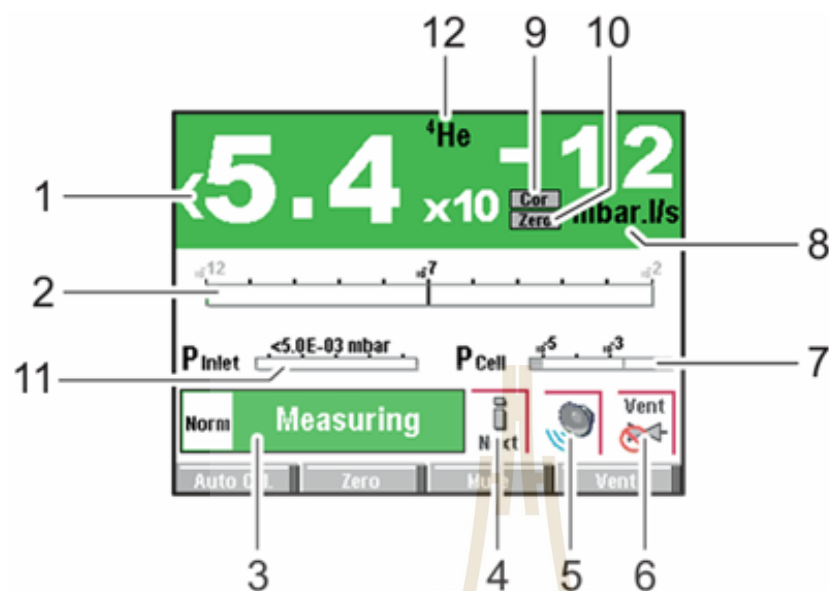


Figure 3.25 Setup of the leak-testing system using a Pfeiffer Adixen ASM 340 leak detector at SLRI.

Procedure:

- Cleaned all vacuum components with alcohol to remove contaminants.
- Assembled components and sealed the chamber using a reusable Viton gasket.
- Connected a Pfeiffer Adixen ASM 340 leak detector via a flexible hose.
- Activated the turbomolecular pump to evacuate the chamber.
- Applied helium around all seals and connections by spraying or enclosing them in a plastic bag.
- Waited 30 minutes for stabilization.
- Monitored helium leak rate; confirmed leak-tight condition if below 1×10^{-8} mbar·L/s.



1	Digital display of the leak rate (green \leq reject set point < red)
2	Bargraph display of the leak rate (adjustable scale)
3	Detector status and Detection mode
4	Access error information
5	Mute function indicator (except ASI 30)
6	Air inlet function indicator (except ASI 30)
7	Cell pressure bargraph display
8	Leak detector unit
9	Leak rate correction function indicator
10	Zero function indicator
11	Detector inlet pressure display (unit consistent with the leak rate unit)
12	Tracer gas (³ He, ⁴ He or H ₂)

Figure 3.26 Monitoring and recording the leak rate and inlet pressure according to the operating instructions. Ref. Pfeiffer Vacuum GmbH. (n.d.). CF Vacuum Gate Valves [Product data sheet].

3.2.2 High Voltage Power Supply (HVPS)

A high-voltage power supply for mass spectrometry should provide stable DC output up to 60 kV with ultra-low ripple ($\leq 0.001\%$ pp), tight voltage regulation ($\pm 0.01\%$), and precise current control to avoid signal drift. It must include safety interlocks, remote control capability, and effective cooling (air or water) while fitting standard rack dimensions for laboratory integration (Matsusada Precision Inc., 2023).

3.2.2.1 HVPS for ion source

The internal components of the ion source designed for AMS require three distinct power-supply zones to generate the necessary electric fields, as illustrated in Figure 3.27. The first zone (green) includes the sample target, target support, and immersion lens, all operating at -40 kV. The second zone (orange) consists of the ionizer shroud, ionizer body, and ionizer support, with a voltage range of -35 kV to -28 kV to control the sputter energy during cesium sputtering. The third zone (blue) operates at ground potential.

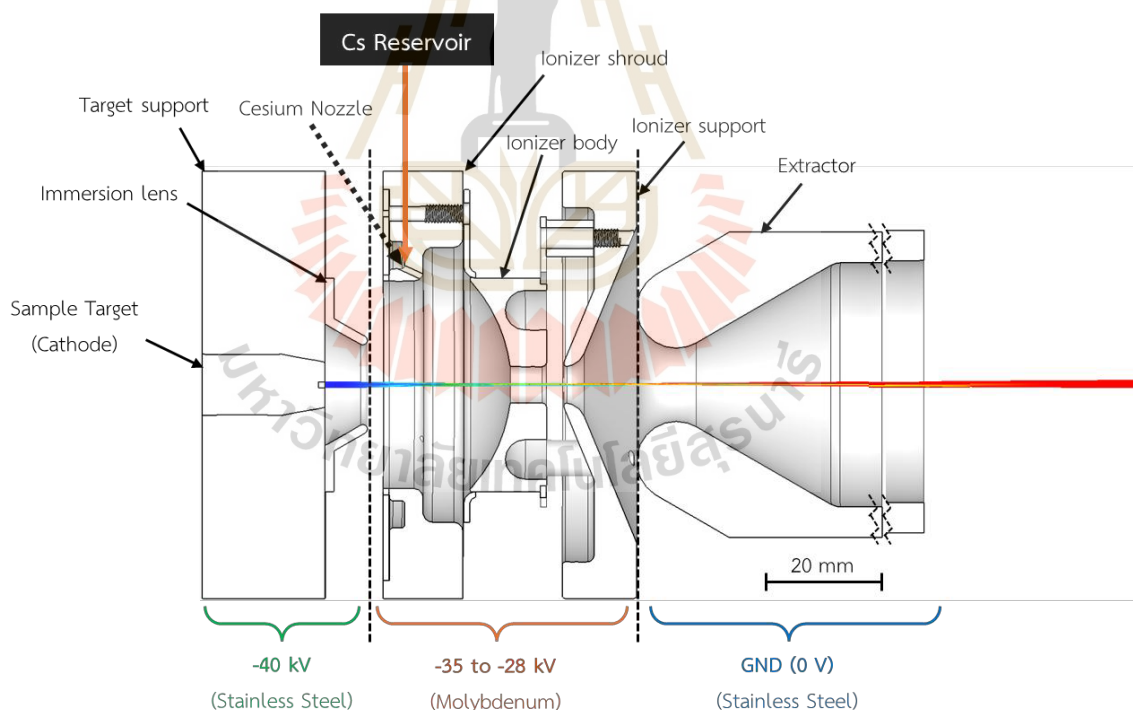


Figure 3.27 Simplified diagram of the power-supply zones for generating electric fields in the cesium sputter source for AMS at SLRI.

In addition to the electric fields, the cesium sputtering process requires three dedicated heaters. The first heater warms the cesium reservoir to about 120 °C so that liquid Cs vaporizes. The second heater maintains the vapor state in the cesium transport line, preventing condensation before the Cs nozzle. The third heater powers the MoRe filament located behind the ionizer body. According to Table 2.1, reaching a filament temperature of 1200 °C requires approximately 150 W of power.

3.2.2.2 HVPS for octupole deflector

The octupole deflector operates at a relatively low voltage and requires a stable, adjustable 1 kV DC supply to generate the internal electric field for beam steering. Figure 2.5 shows the schematic design of the deflector, which uses four independent rods. Each rod must be driven by its own power supply, so four identical 1 kV units are required to provide precise and independent voltage control.

3.2.2.3 HVPS for Einzel lens

Similarly, the Einzel lens requires a negative bias voltage on its central electrode to generate the focusing field, as shown in Figure 2.14. This bias is adjustable up to -30 kV and is supplied by a dedicated high-voltage unit to ensure stable and precise beam focusing.

3.2.2.4 High voltage isolation transformer

In operating the ion source, the three power supplies for the Cs reservoir, Cs line, and ionizer heater must float at the ionizer body potential of -30 kV. To reduce costs and avoid purchasing additional high-voltage power supplies, a high-voltage isolation transformer is used to float these supplies at -30 kV. Similarly, the graphite target requires -40 kV; by floating its supply on the same -30 kV reference, only a -10 kV power supply is needed to achieve the required -40 kV, further minimizing expenses. The isolation transformer must be mounted on an insulator or high-voltage bushing to ensure that the external beamline remains at ground potential.

3.2.3 Integrated system

By selecting existing vacuum components from SLRI and procuring the necessary power supplies, a low-energy negative carbon ion beamline for AMS was assembled based on the combined dimensions of these parts. Various component spacings were studied by creating detailed drawings in SolidWorks, followed by the production of a 3D-printed prototype of the system. This work was carried out in collaboration between SLRI and NARIT, with an emphasis on maintaining a compact design and ensuring that all external beamline structures remain at ground potential for safety.

3.3 The development of heater for ionizer

In the sputtering process within the ion source, the surface of the ionizer body plays a critical role in ionizing cesium vapor into Cs^+ ions. To enable this, the ionizer body surface must be heated to approximately 1200 °C. In the experiments, the heater coil positioned behind the ionizer body is tested. This coil, made from MoRe alloy, is wound in a toroidal shape. The required wire length and number of turns are calculated to ensure that the coil can achieve the necessary temperature.

3.3.1 Calculation and design of the toroidal heater

The AMS development project for radiocarbon dating at SLRI purchased MoRe filament wire with a 0.9 mm diameter, matching the specifications of the filament material used by HeatWave Labs Inc. (Figure 2.15). MoRe is an exceptionally strong alloy with a melting point around 2450 °C as shown in Table 2.2. The addition of rhenium increases its toughness and resistance to creep at high temperatures, preventing the wire from stretching or becoming brittle during operation. In vacuum, MoRe also exhibits lower metal evaporation than tungsten or graphite filaments, reducing chamber contamination and extending filament lifetime.

In calculating the required wire length, the electrical resistivity (ρ) is referenced from Figure 2.16, which shows that at an operating temperature of 1200 °C, ρ is 200 $\mu\Omega \cdot \text{cm}$. Since resistivity increases with temperature, and Table 2.1 indicates a power requirement of approximately 150 W, the filament length needed for the toroidal heater can be determined using the following equations:

The electrical power equation is defined from the definitions of work W and electric current I . When calculating the power P :

$$P = \frac{dW}{dt} = \frac{dQ}{dt} V = IV \quad \text{Eq. 9}$$

Ohm's law describes by:

$$V = IR \quad \text{Eq. 10}$$

Electrical resistance formula describes how the electrical resistance R of a uniform conductor depends on its material resistivity ρ , length L , and cross-sectional area A . It is given by the formula:

$$R = \rho \frac{L}{A} \quad \text{Eq. 11}$$

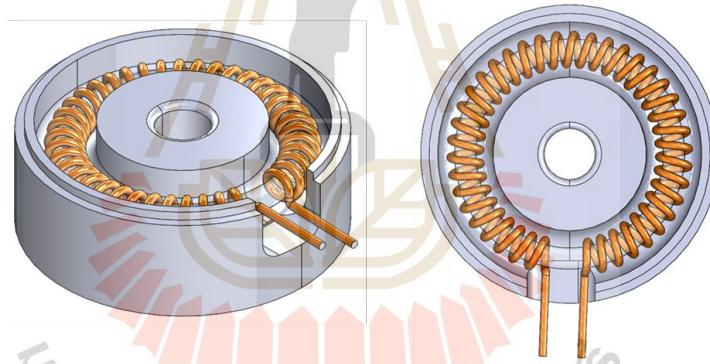


Figure 3.28 Toroidal heater with 40 turns installed inside the rear of the ionizer body.

At an operating temperature of 1200 °C, Table 2.1 indicates that the filament resistance, calculated using Ohm's law, is 0.6 Ω . Using the electrical resistance formula, the required wire length is determined to be approximately 0.2 m. Since the heater coil is mounted behind the ionizer body, an insulating material is required to prevent electrical shorting. Alumina (Al_2O_3) was selected to separate the coil from the ionizer body due to its excellent insulating properties. To achieve the target resistance, the coil must be wound with 22 turns around a 2 mm-diameter mandrel. However, during the creation of the SolidWorks drawing, it was found that doubling the number of turns is feasible. This modification increases the overall coil length, raises its resistance, and reduces power consumption, as illustrated in Figure 3.28.

The relationship between temperature and resistance in metals is typically described by the linear Temperature Coefficient of Resistance (TCR) equation, which is also known as the Resistivity Equation for Conductors.

$$R(T) = R_0[1 + \alpha(T - T_0)] \quad \text{Eq. 12}$$

Where:

- $R(T)$ is the resistance at temperature T ,
- R_0 is the resistance at a reference temperature T_0 (often room temperature),
- α is the temperature coefficient of resistance (TCR), which is a material-specific constant that determines how much the resistance increases with temperature,
- T is the temperature in Celsius (or Kelvin, with appropriate conversions).

For the relationship between temperature and power, the power consumed by the filament is related to its temperature and follows a nonlinear relationship governed by the Stefan-Boltzmann law for radiative heat loss:

$$P = \varepsilon \sigma A T^4 \quad \text{Eq. 13}$$

Where:

- P is the power radiated by the filament,
- ε is the emissivity of the filament,
- σ is the Stefan-Boltzmann constant $5.67 \times 10^{-8} \text{ W/m}^2 \text{ K}^4$,
- A is the surface area of the filament,
- T is the absolute temperature in Kelvin.

3.3.2 Fabrication of the toroidal heater

After finalizing the design, the heater coil drawing was sent to SLRI's machine shop for fabrication, as shown in Figure 3.29. For the insulator between the ionizer body and the heater coil, alumina paste was selected, allowing it to be pressed into the body's grooves for effective insulation. To apply the paste, a tamper tool was 3D-printed at SUT QLAB, as shown in Figure 3.30. The application process was first tested using modeling clay as a stand-in for the alumina paste to ensure proper fit and handling.

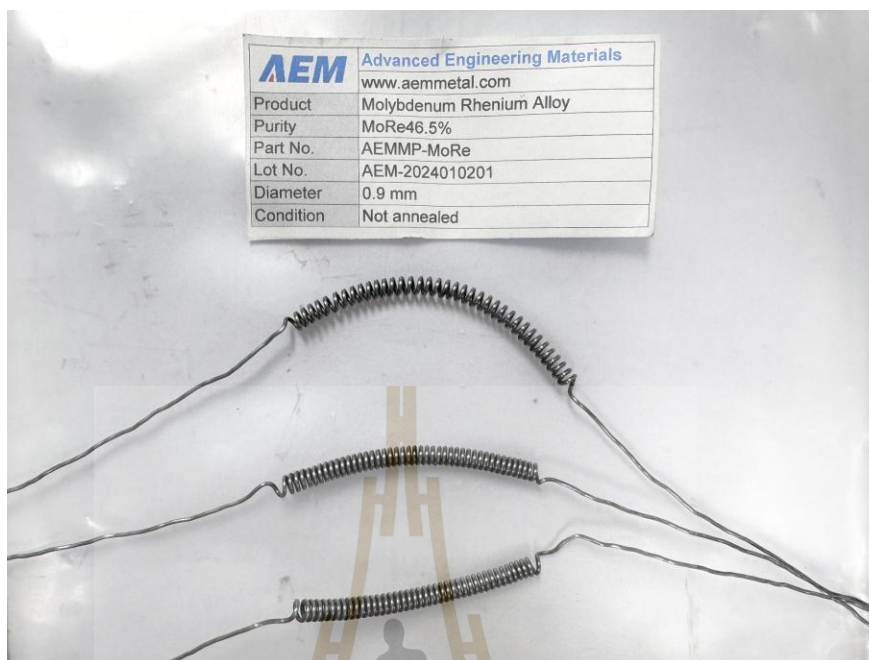


Figure 3.29 Fabrication of the toroidal heater coil by SLRI's machine shop.



Figure 3.30 3D-printed prototype of the tamper by SUT QLAB.

3.3.3 Experimental setup

Once all preparations were complete, the heater coil test was set up under vacuum, as shown in Figure 3.31. An SLRI vacuum chamber was selected for its suitable ports, including a high-current feedthrough, flex hose, CF203 viewport, and pressure gauge. A pyrometer was used to measure the coil's temperature based on its thermal radiation, with an emissivity (ϵ) of 0.17 applied for MoRe and the pyrometer positioned 22 cm from the coil through the viewport, with video output displayed on a monitor. A mobile vacuum pumping unit—consisting of a scroll pump and a turbomolecular pump—was connected to the chamber via the flex hose. The high-current power supply was attached to the feedthrough using a custom connector that also secured the coil in place. Finally, the pressure gauge was installed on the chamber to monitor vacuum levels during testing.

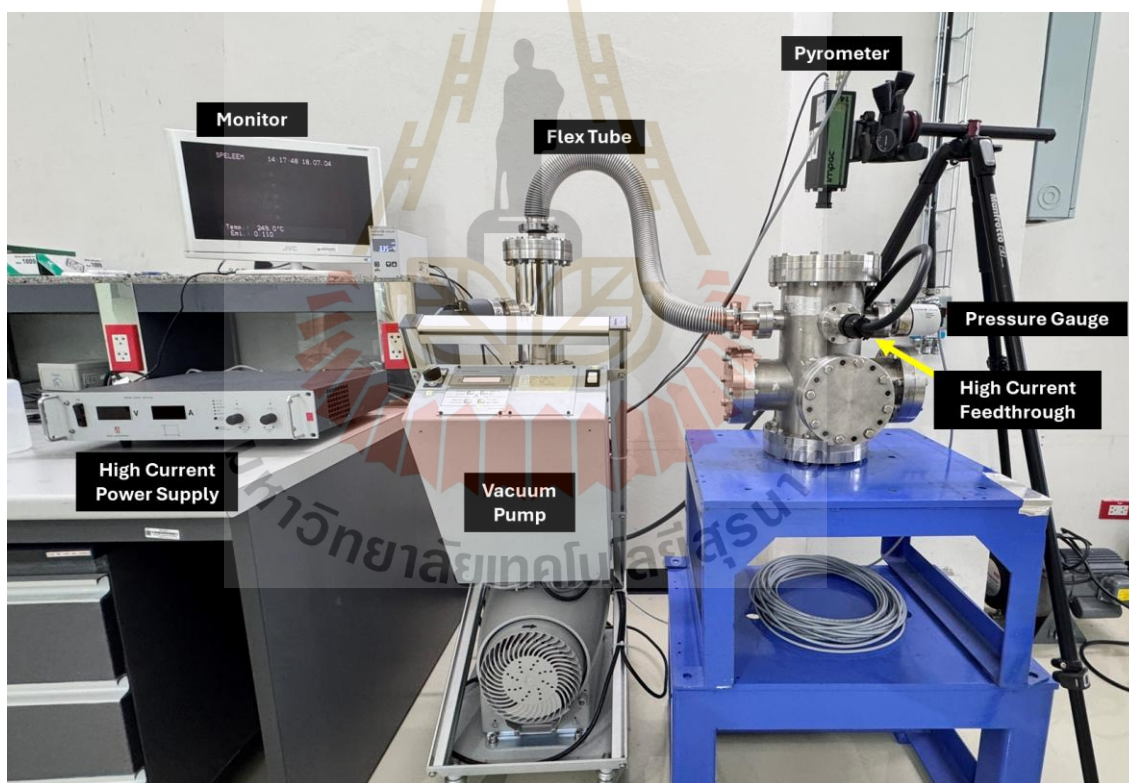


Figure 3.31 Experimental setup for heating the MoRe coil in the vacuum system.

CHAPTER IV

RESULTS AND DISCUSSION

Chapter IV discusses and analyzes the experimental results, including computer simulations of the ion source, octupole deflector, Einzel lens, and the fully integrated system. It also presents the assembly of the compact beamline system, which includes the vacuum components and the power supplies mounted beneath the beamline. Finally, the chapter explains the results from the vacuum heater coil tests conducted on the ionizer.

4.1 Computer simulation results

In both the simulation and the system assembly, the distances follow the optical layout as shown in Figure 4.1.

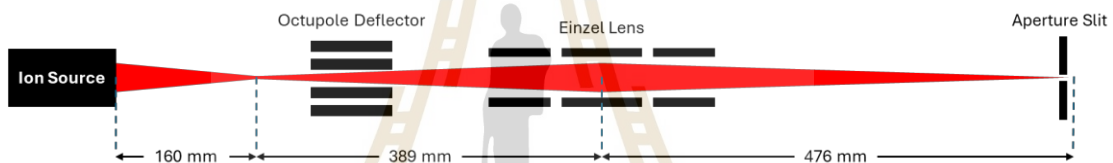


Figure 4.1 Optical layout of the negative carbon ion beamline.

In the simulations, a mesh convergence study is always performed before finalizing the results of each model. For example, a convergence study was conducted on the ion source model, as shown in Figure 4.2, to determine the optimal cell size. This ensures accurate results while conserving computational resources and reducing simulation time.

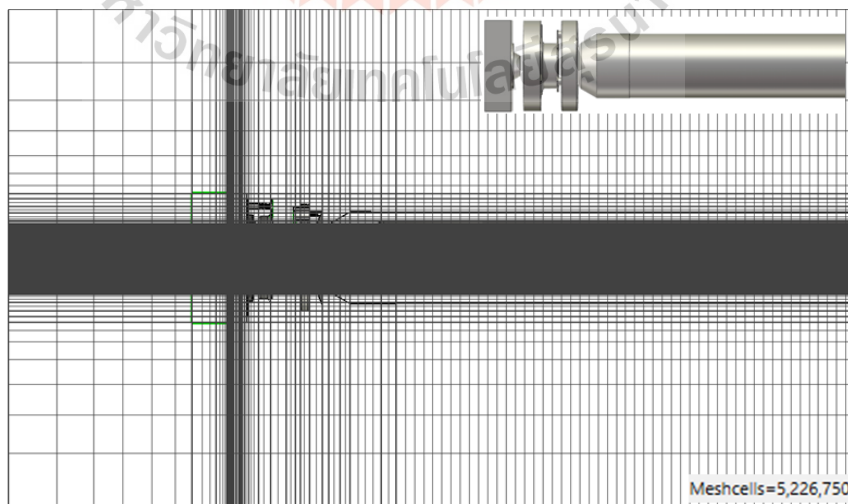


Figure 4.2 Optimal mesh size of the ion source model.

4.1.1 Convergence study

The parameter N_{mesh} was varied to increase mesh density in regions near surfaces or areas requiring high detail. N_{mesh} represents the number of cells per maximum model box edge. A parameter sweep was performed across ten values of N_{mesh} (ranging from 20 to 200). The results showed that increasing the mesh density beyond $N_{mesh} = 20$ led to changes of less than 1%, meeting the commonly accepted convergence threshold of approximately 1% used in Field/PIC/FEM studies. This threshold balances the need for high accuracy with acceptable computational cost.

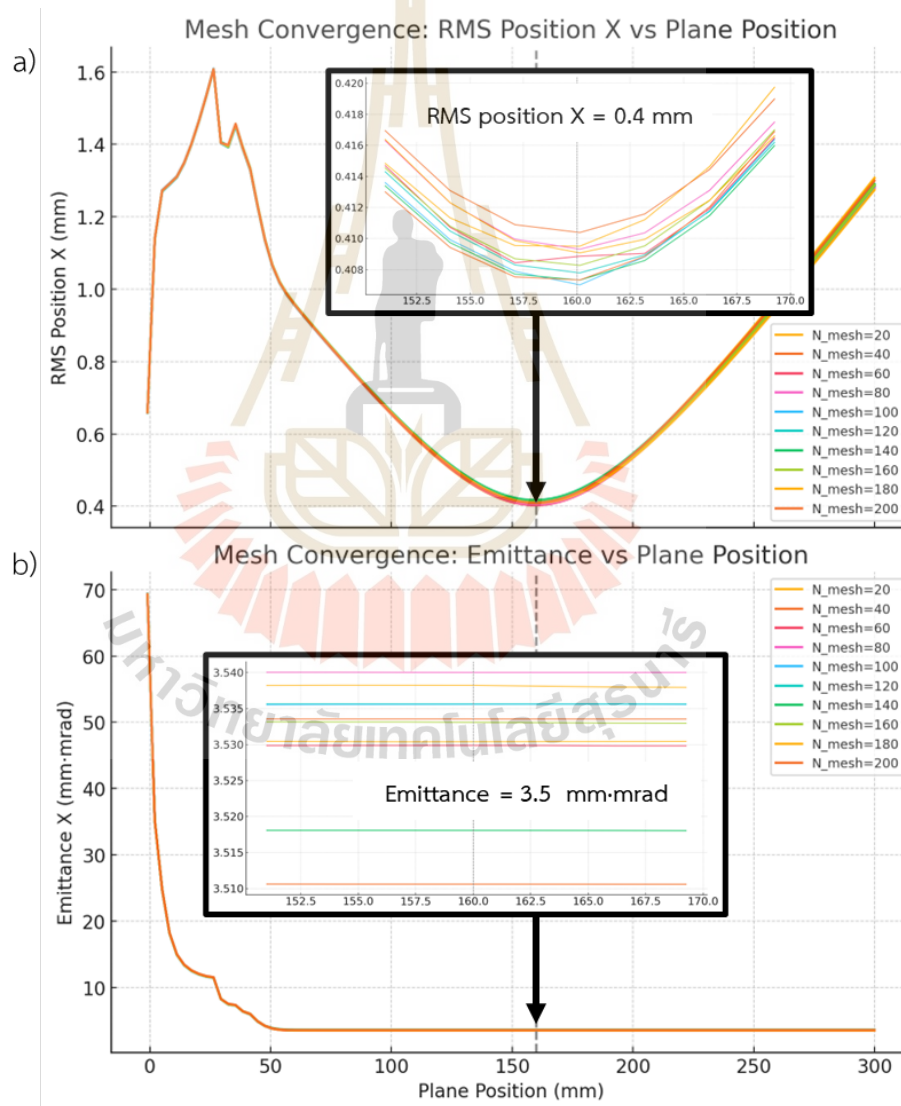


Figure 4.3 Convergence study graphs used to select the optimal mesh size for the ion source model. a) rms(position_x) vs. plane position b) Emittance vs. plane position.

From Figure 4.3, it is observed that the results converge when considering both the $rms(position_x)$ and emittance on the particle monitor along the beam path. The ion source's focal point is located 160 mm from the sample target, where the $rms(position_x)$ is 0.4 mm—consistent with the beam image in Figure 3.7b—and the emittance stabilizes at 3.5 mm·mrad immediately after extraction. Based on these findings, a mesh density corresponding to $N_mesh = 20$ —the lowest value tested—was selected. This choice results in a total of 5,226,750 cells for the ion source model simulation, as shown in Figure 4.2.

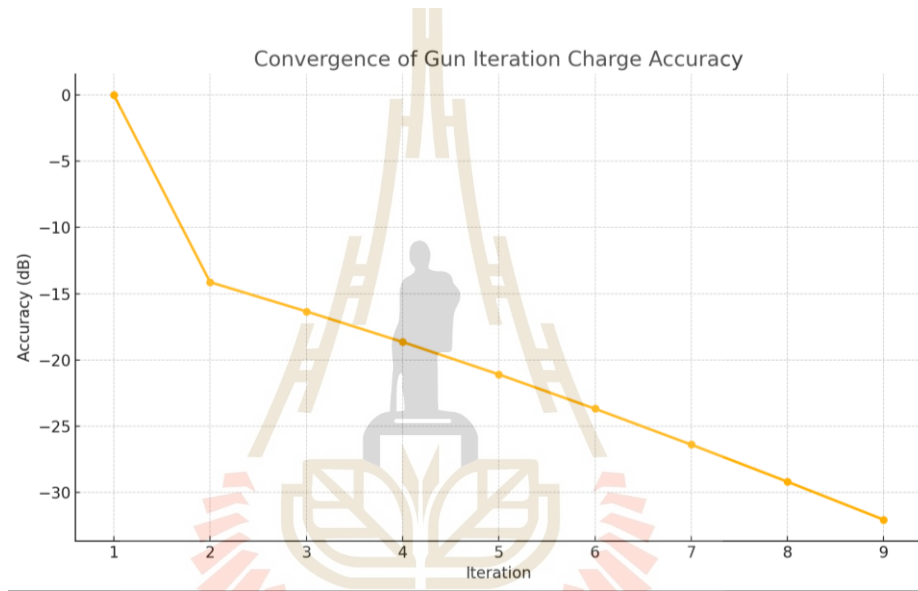


Figure 4.4 Convergence of gun iteration vs. charge accuracy.

4.1.2 The study of miss alignment of the octupole deflector

Based on the available alignment tools and system design, engineers defined the maximum possible alignment errors as a 1 mm offset and a 2° tilt. In the simulation, two parameters were varied: the tilt angle (θ) at 0°, 0.5°, 1°, 1.5°, and 2°, and the octupole deflector's y-axis offset at 0, 0.5, 1, 1.5, and 2 mm. The objective was to determine whether the beam, under worst-case misalignment conditions, still focuses onto and passes through the aperture slit. Beam acceptance was evaluated by analyzing the particle monitor images at the slit, which has a maximum opening of 20 × 20 mm².

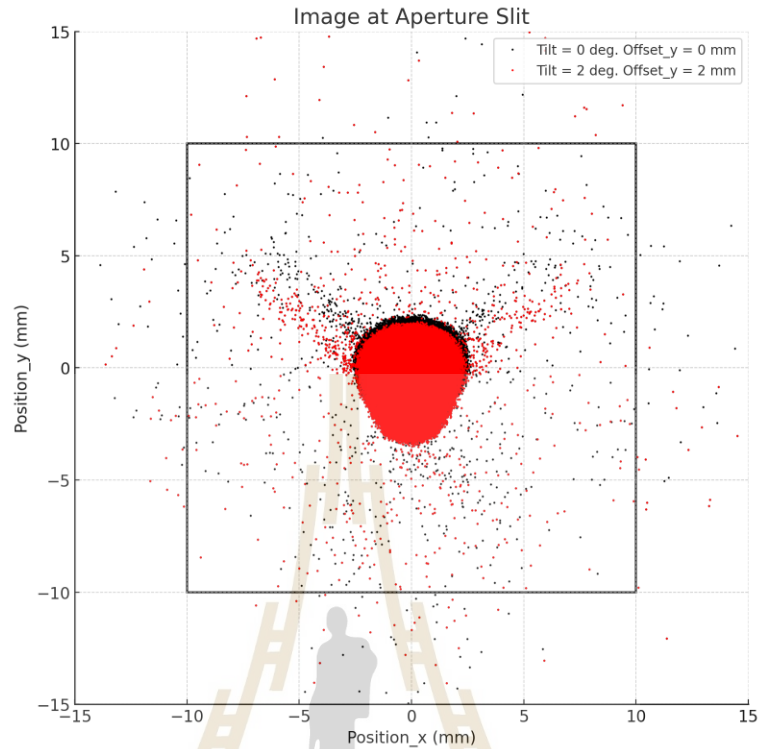


Figure 4.5 Comparison of particle images at the aperture slit between perfect alignment (black) and tilt = 2° with offset = 2 mm (red). The black square indicates the maximum slit opening of 20 × 20 mm².

The simulations demonstrated that in all 25 misalignment scenarios, over 99% of the ions successfully passed through the fully open 20 × 20 mm² slit and remained focused. Two representative cases are compared in Figure 4.3: perfect alignment ($\theta = 0^\circ$, offset = 0 mm) and the worst-case misalignment ($\theta = 2^\circ$, offset = 2 mm). In the worst-case scenario, the ion beam was displaced by 1 mm along the y-axis at the focal plane, as shown in the histogram in Figure 4.6, while the overall beam shape remained essentially unchanged. This displacement can be corrected by increasing the electric field through the application of a bias voltage to the octupole rod on the side toward which the beam has shifted. Chomchan et al. (2024) demonstrated (Figure 2.6) that applying up to 300 V to a single octupole rod can steer the beam by approximately 1.5 mm downstream of the deflector. Therefore, the octupole deflector—with its independent x-y steering capability—can reliably compensate for misalignment errors.

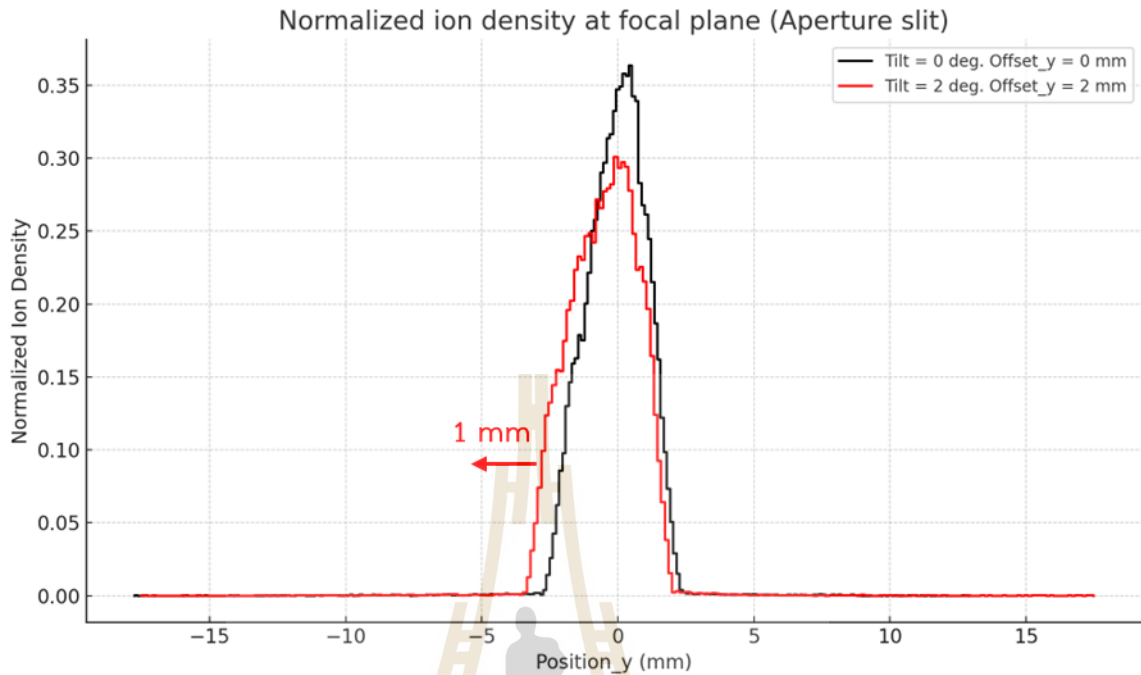


Figure 4.6 Comparison of normalized ion density at the aperture slit for perfect alignment (black) and for the worst-case misalignment with $\theta = 2^\circ$ and offset = 2 mm (red), shown as a histogram.

4.1.3 Einzel lens simulation results

4.1.3.1 The study of effects from mounting support

The first model, including its mounting supports shown in Figure 4.7a, produced a three-lobed beam profile at the focal plane downstream of the Einzel lens. This distortion was caused by electric-field perturbations (Figure 4.8) from the three long stainless-steel support rods on rings 1 and 3. To correct this, the model was revised as shown in Figure 4.7b by reducing the gap between the support rings and adopting the dimensions from Suethonglang et al. (2024).

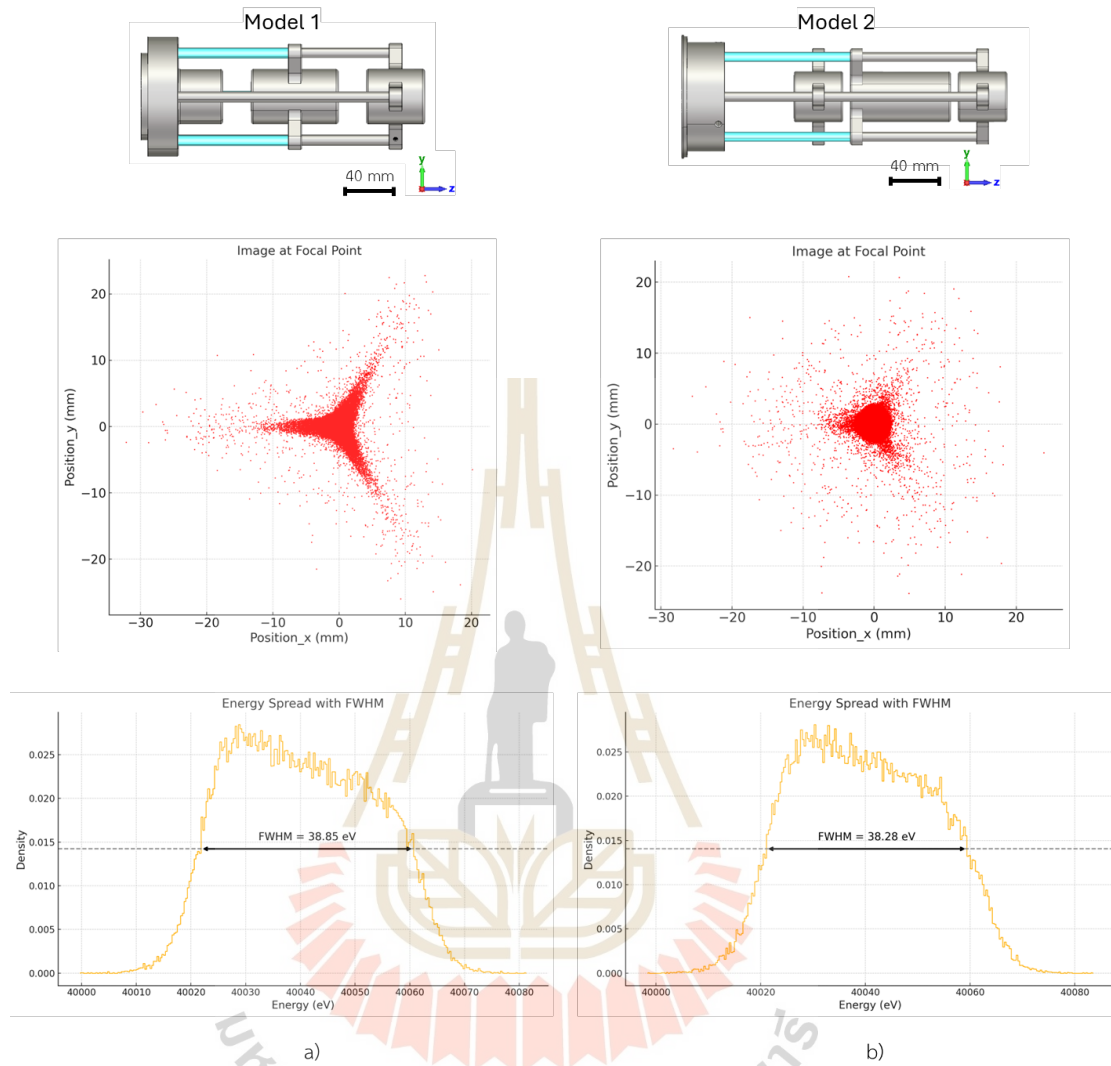


Figure 4.7 Simulated beam image at the focal plane using a -20 kV bias on the central electrode. a) Model 1 with ratio of 43 : 21 : 64 mm. b) Model 2 ratio of 40 : 6 : 82 mm. The insulator segment is shown in blue.

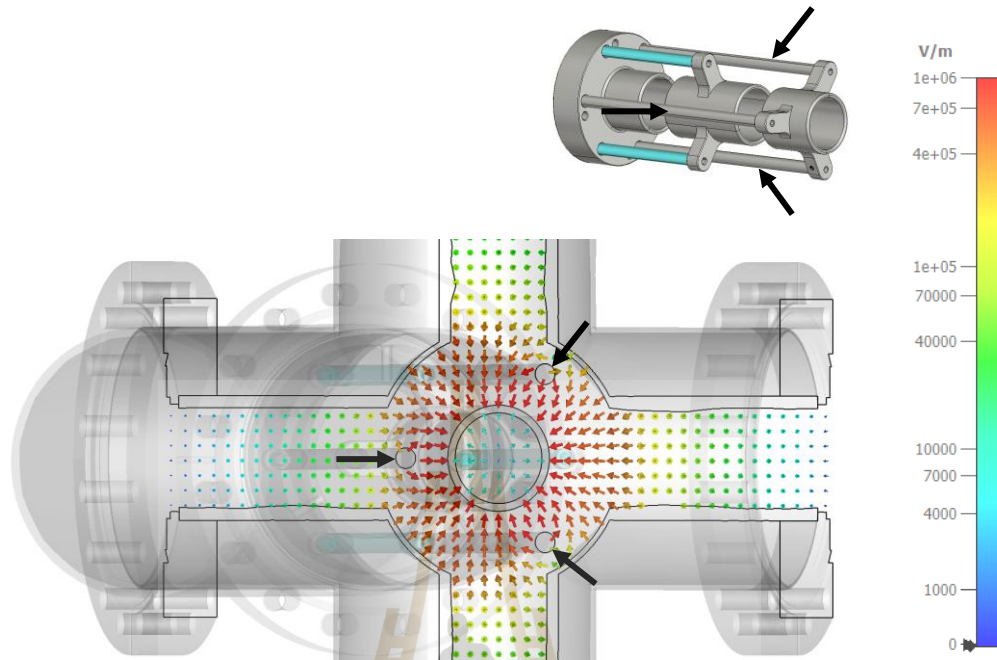


Figure 4.8 The electric field inside Einzel lens model 1 is shown in a cross-sectional view to illustrate the electric field perturbations around the support rods (black arrows).

After updating to Model 2, the beam image still exhibits slight lobes. This distortion is unavoidable, as the electric field from the support rods penetrates the ion beam path. To minimize this effect, the gap between the support rings was reduced to 6 mm—the minimum allowable distance without risking electrical breakdown. In ultra-high vacuum conditions (10^{-6} to 10^{-9} Torr), the dielectric strength typically ranges from 20 to 40 MV/m (20–40 kV/mm); however, practical values between 5 and 20 kV/mm have been reported by Ratkus et al. (2024), depending on electrode surface finish and geometry.

Moreover, the Model 2 design focuses the ion beam more effectively than Model 1, as shown in Figure 4.9. When the same -20 kV bias is applied to the Einzel lens, Model 2 achieves a focal distance of 900 mm from the source, compared to 1100 mm for Model 1. The shorter focal length reduces the power required from the supply, making Model 2 more energy-efficient. Based on these advantages, Model 2 was selected for use in the negative carbon ion beamline in AMS.

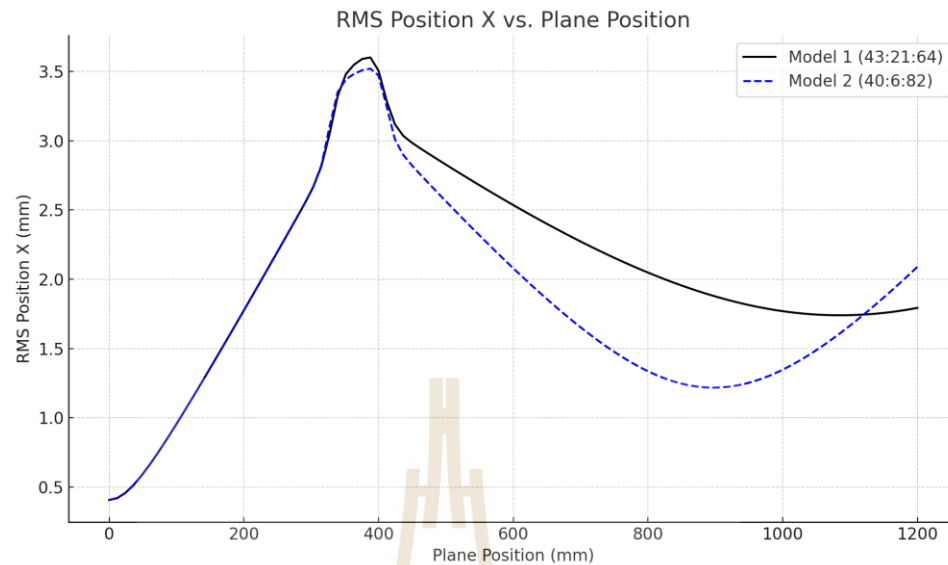


Figure 4.9 Comparison of the focal distances of Einzel lens Model 1 and Model 2.

4.1.3.2 The study of focal range

Using Einzel lens Model 2, which has dimensions of 40 : 6 : 82 mm, further studies were conducted with the selected negative-polarity power supply from Matsusada Precision, Inc., capable of delivering up to 30 kV. Bias voltages ranging from 0 V to –30 kV were applied to the central electrode in ten increments (0 V, –2.5 kV, –5 kV, ..., –30 kV), as shown in Figure 4.10. These simulations enabled the examination of the corresponding focal distances at each voltage level.

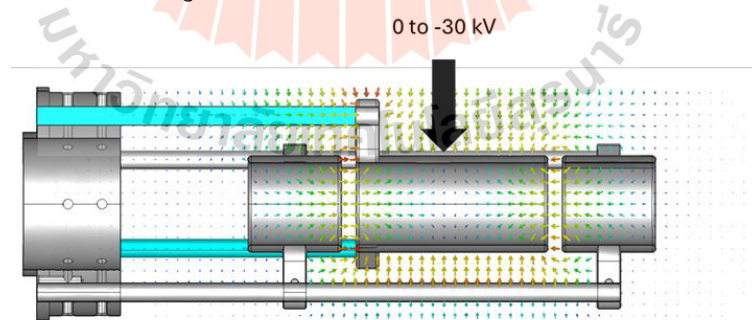


Figure 4.10 Cross-sectional view of the electric field within the Einzel lens, showing how the field strength varies with the applied bias voltage.

The results showed that increasing the central-electrode voltage strengthened the electric field and shortened the focal length, reaching a minimum of 83.61 mm downstream from the lens center at –30 kV. At –17.5 kV, the ion beam was nearly parallel.

A shorter focal length requires a stronger field, which pulls the beam into a tighter convergence and produces a larger convergence angle. After the focus, that same angle causes rapid divergence. In other words, a short focal length yields a smaller spot size at the focus but increases aberrations and space-charge effects, causing the beam to spread out more quickly beyond the focal point as shown in Figure 4.12.

The optimizer function was then used to determine the ideal bias voltage needed to focus the ion beam at 865 mm—the position of the aperture slit measured from the source. The study found that a voltage of $-20,139$ V was required, which falls within the operating range of the power supply selected for the AMS radiocarbon dating system.

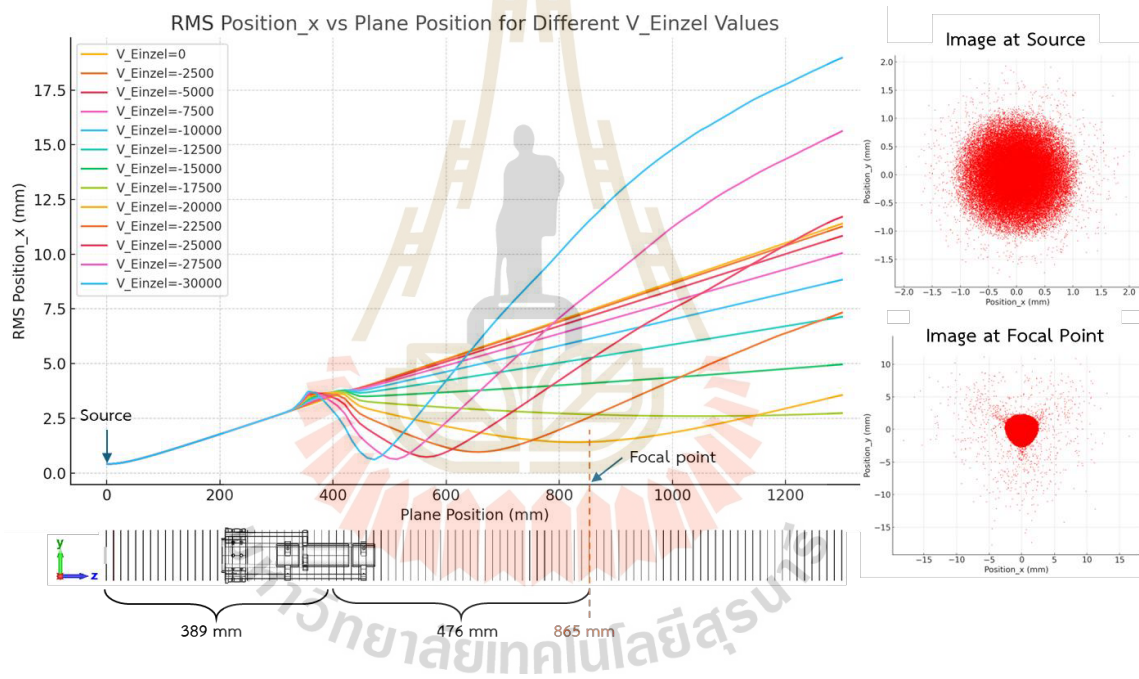


Figure 4.11 Graph showing the relationship between plane position and $rms(position_x)$ for various V_{Einzel} values. The plot also indicates the distance from the source to the center of the Einzel lens (389 mm) and the distance from the lens center to the aperture slit (476 mm).

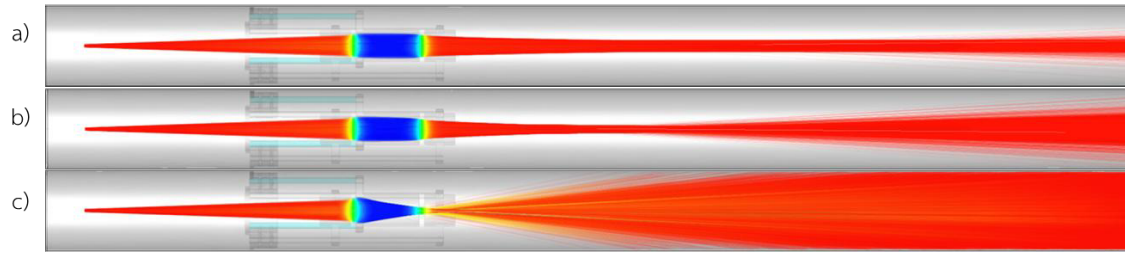


Figure 4.12 Trajectories of negative carbon ions through the Einzel lens. a) -17.5 kV, producing an almost parallel beam. b) $-20,139$ V (from the optimizer), focused exactly at the aperture slit. c) -30 kV, the maximum output of the power supply.

4.1.3.3 The study of miss alignment

In this section, the practical challenges of assembling the Einzel lens downstream of the octupole deflector are addressed. Both components share common mounting supports on a CF152 vacuum chamber flange. Acknowledging that perfect alignment is unattainable in the actual system, maximum assembly errors were defined as a 1 mm offset and a 2° tilt, based on the limitations of the available tooling.

With the central electrode biased at $-17,500$ V, a total of 81 misalignment scenarios were investigated. In the worst-case scenario—featuring a 1.6 mm offset and a 1.6° tilt—the ion beam trajectory deviated significantly from the optical axis and struck the chamber wall, as shown in Figure 4.13. This led to complete beam loss, with no beam focusing observed at the aperture slit.

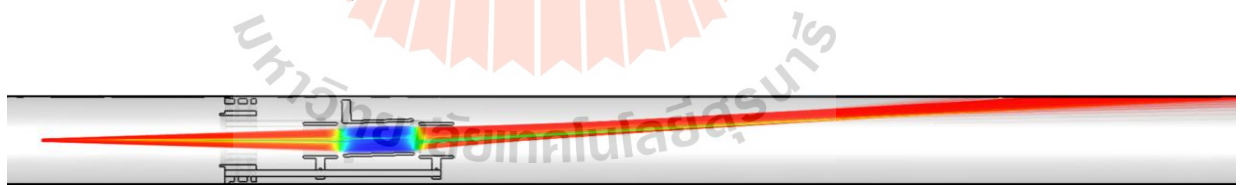


Figure 4.13 Trajectories of C^- ions through the Einzel lens with a middle electrode 1.6° tilt and 1.6 mm offset from the optical axis.

The results from the particle monitor at the aperture slit, evaluating whether the beam remained focused on and passed through the slit under varied parameters, are presented in Table 4.1.

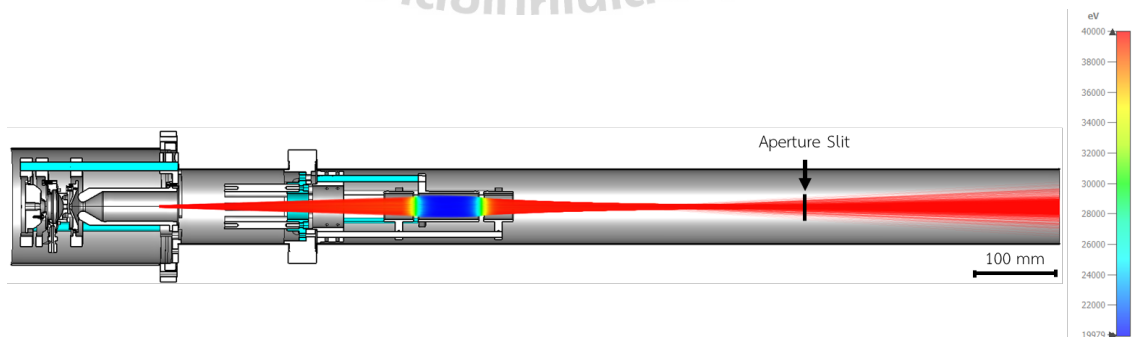
Table 4.1 Acceptable tolerances for the central electrode of the Einzel Lens.

Offset_y (mm)	Tilt angle (θ)
0.0	0.6
0.2	0.4
0.4	0.2

The table shows that the middle electrode cannot be offset by more than 0.4 mm, nor tilted by more than 0.6° , with other tolerances kept at zero. This differs from the octupole deflector, which maintained beam focus at the slit even with a 2° tilt and 2 mm offset. The stricter tolerances for the Einzel lens result from the very strong electric field between the central and side electrodes. Even a slight misalignment breaks the field symmetry and immediately deflects the ion beam.

4.1.4 Low-energy negative carbon ion beamline simulation results

In this section, the results of the end-to-end beamline simulation are presented, encompassing the ion source, octupole deflector, Einzel lens, and aperture slit within a fully integrated CST model. To streamline the simulation, nonessential hardware—such as vacuum pumps, chamber fittings, and screws—was omitted. The particle distribution at the ion source focus was imported using the Particle Import Interface. Under ideal, perfectly aligned conditions, the optimized bias voltage of $-20,139$ V was applied to the Einzel lens. The beam size, emittance, beam envelope, and particle image were then tracked along the optical axis using a 2D monitor placed at the aperture slit and a series of 100 monitors positioned from the source focus to just beyond the slit.

**Figure 4.14** Trajectories of C^- ions passing through the perfectly aligned low-energy negative carbon ion beamline.

At the aperture slit, the ion beam emittance was found to be 8 mm·mrad at 40 keV. When multiplied by the square root of the beam energy in MeV ($\sqrt{0.04}$ MeV), this yields 1.6 mm·mrad· $\sqrt{\text{MeV}}$ —well within the design requirement of keeping the emittance below 10π mm·mrad· $\sqrt{\text{MeV}}$ at the slit. This confirms the system's ability to deliver a negative carbon ion beam up to 40 keV with adjustable focal length and independent X–Y steering. The beam size, based on $\text{rms}(\text{position}_x)$ and $\text{rms}(\text{position}_y)$, was approximately 2.42×2.38 mm² (Figure 4.15). Furthermore, 99% of the ions successfully passed through the fully open slit.

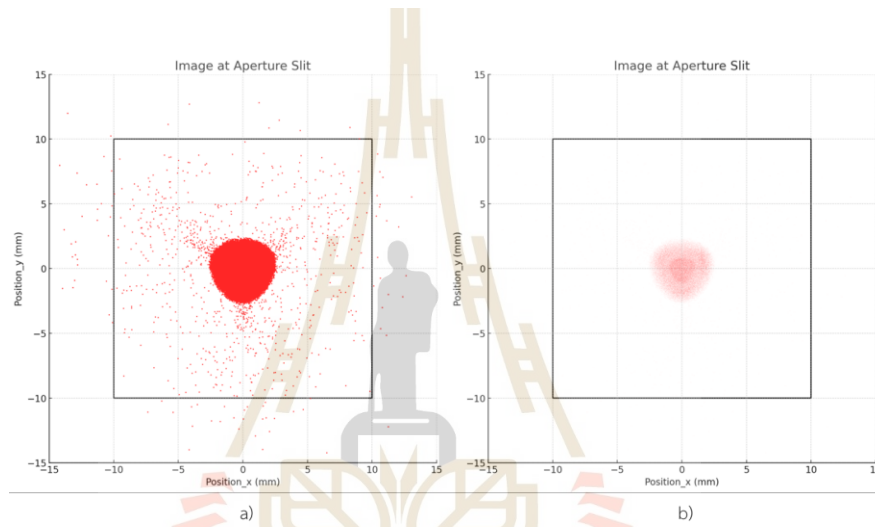


Figure 4.15 Particle images at the aperture slit for the perfectly aligned low energy negative carbon ion beamline. The black square indicates the maximum slit opening of 20×20 mm². Figure a) mark size = 1.5 and Figure b) mark size = 0.1

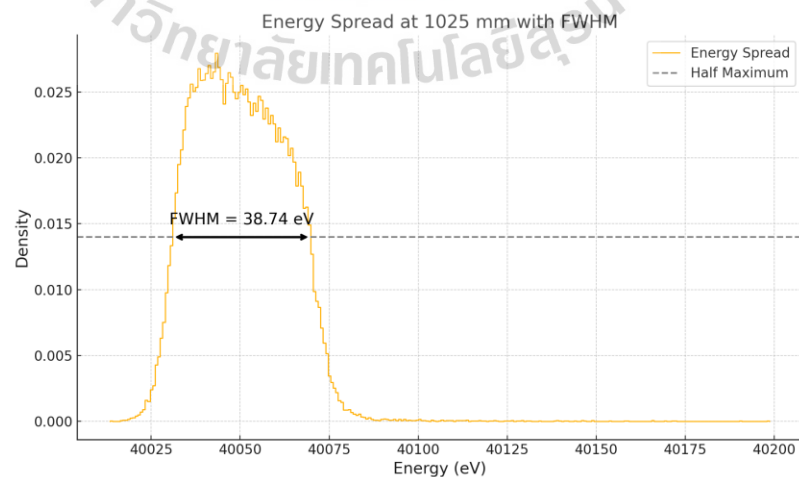


Figure 4.16 Energy spread with FWHM at the aperture slit location.

4.2 Low-energy beamline design

4.2.1 Leak checking by helium detector

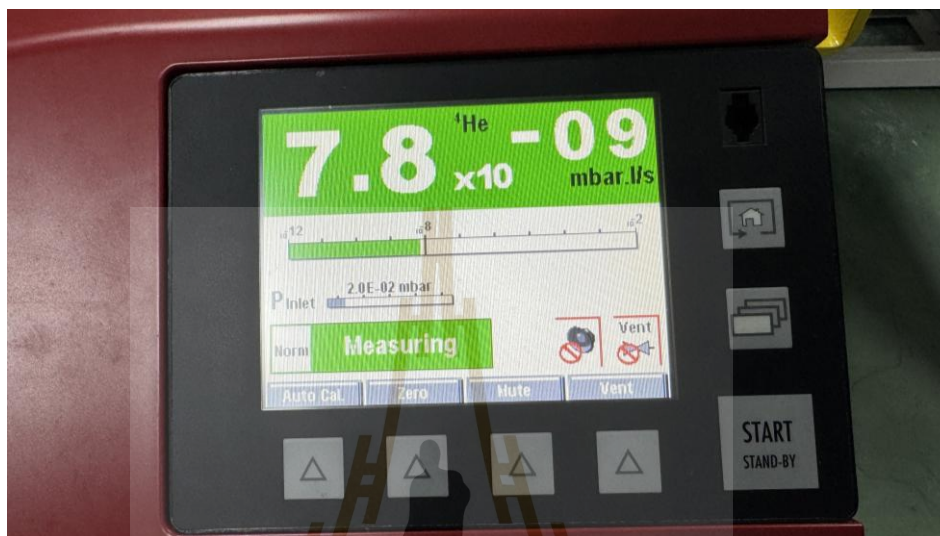


Figure 4.17 Digital display of the helium leak rate during vacuum component testing.

By selecting existing vacuum components from SLRI, each part was first cleaned with alcohol to remove contaminants. A leak check was then performed using a Pfeiffer Adixen ASM 340 leak detector. All components were found to be suitable for use, with measured helium leak rates on the order of 10^{-9} mbar·L/s—well below the 10^{-8} mbar·L/s threshold—indicating that the chambers were leak-tight and ready for operation. These components were therefore selected for assembly in the AMS beamline.

4.2.2 High voltage power supply

A suitable high-voltage power supply configuration for the low-energy negative carbon ion beamline was selected from Matsusada Precision, Inc. The system uses 10 DC power supplies, all powered from a 220 V AC input. For the cesium-sputter ion source, five HVPS units are required. One unit AU-40N1.5-LCW(220V)(5m) provides the ionizer bias field, while four identical units float on an isolation transformer to supply:

1. The high-current heater for the ionizer (TB35V72A720W-Lgob)
2. The heater for the cesium reservoir (TB35V36A360W-Lgob)
3. The heater for the cesium transport line (TB35V36A360W-Lgob)
4. The sample target bias, which operates at -40 kV, using an AU-15N2-LCW(220V)(5m)

One additional HVPS AU-30N1-LC(220V)(5m) provides the negative bias for the Einzel lens, and four AP-1P(A) supplies independently drive each rod of the octupole deflector for X–Y beam steering. Figure 4.18 shows the digital HVPS control diagram, in which all power supplies are connected via fiber-optic links to a CO-HV interface adapter for isolated computer control and monitoring, and to a CO-E32 interface adapter for simultaneous control of multiple units without electrical noise.

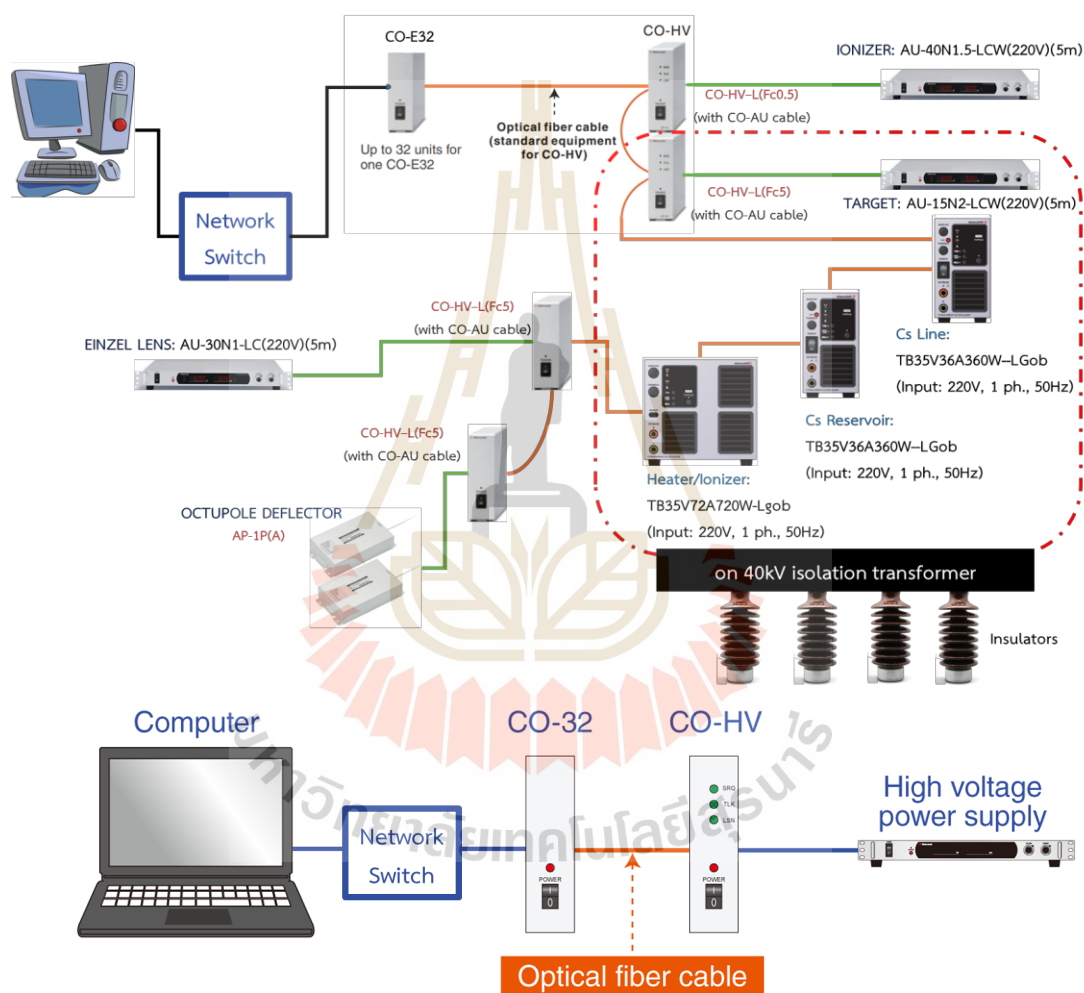


Figure 4.18 Diagram of the HVPS configuration used in the negative carbon ion beamline.

4.2.3 Integrated system

After confirming that all vacuum components were ready for use, collaboration with engineers from NARIT was undertaken to create 3D models in SolidWorks based on the measured dimensions of each chamber, some of which followed standard sizes. The chambers were then arranged in series, with appropriate ports and locations assigned. The beamline is designed to operate under ultra-high vacuum conditions (10^{-6} to 10^{-9} Torr) to minimize ion collisions with residual gas molecules. A gate valve is included to isolate the low-energy negative carbon ion beamline from the downstream bending magnet and acceleration section of the AMS system. Vacuum is maintained by turbomolecular pumps with pumping speeds of 300 L/s, 350 L/s, and 700 L/s, backed by a scroll pump, as shown in Figure 4.19.

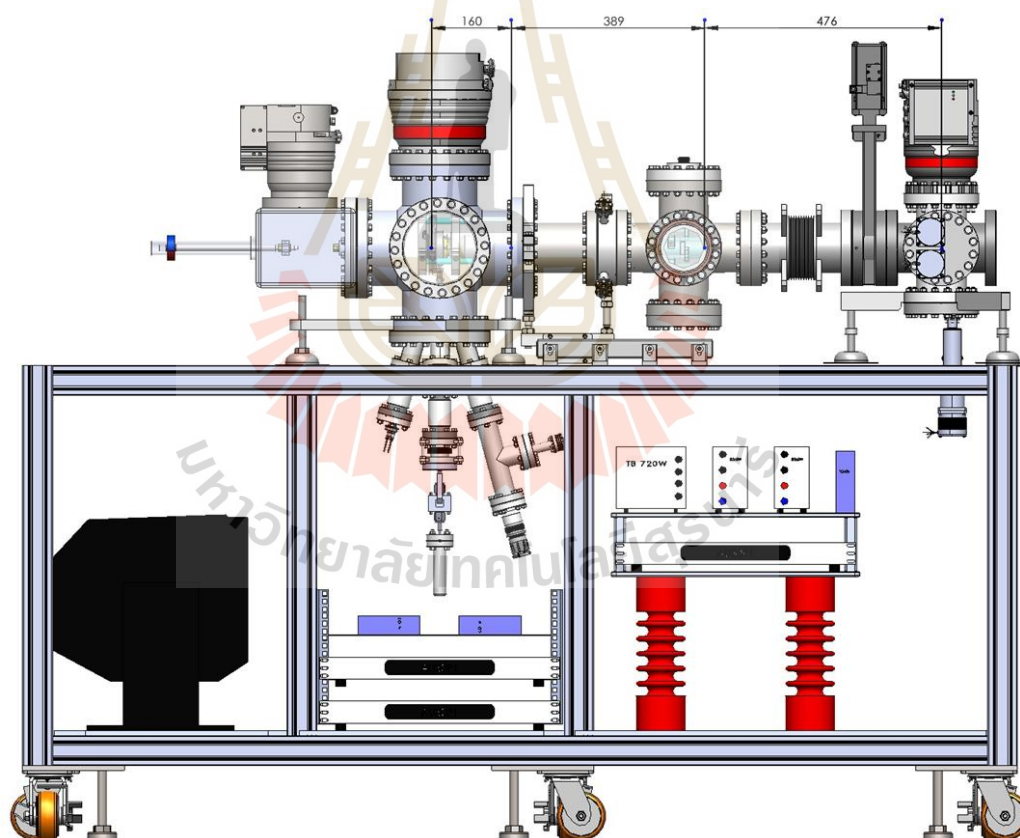


Figure 4.19 A compact system design for the low-energy negative carbon ion beamline, comprising a tabletop vacuum system integrated with HVPS units beneath the table. The ceramic insulator standoffs are shown in red, and the isolation transformer is shown in black.

High-voltage feedthroughs for the Einzel lens and octupole deflector, along with the pressure gauge and viewport, are installed on top of the tabletop vacuum chamber. The 160 mm distance shown in Figure 4.19 is measured from the sample target to the ion source's first focal point. The 389 mm distance extends to the center of the Einzel lens, and 476 mm reaches the aperture slit. This gives the electrostatic Einzel lens a magnification ratio of $476 \text{ mm} / 389 \text{ mm} \approx 1.22$, which is as close to 1 : 1 as practical within the constraints of the vacuum chamber and mounting supports.

The ion source's power supplies and high-voltage feedthroughs are integrated beneath the table. They include an isolation transformer (black) that powers each supply according to the diagram in Figure 4.18. All components rest on ceramic insulator standoffs (red), ensuring that the exterior of the vacuum chamber remains at ground potential for maximum safety.

4.3 The development of heater for ionizer

A tamper tool was 3D-printed at SUT QLAB to press alumina paste (Al_2O_3) into the grooves of the ionizer body, as shown in Figure 4.20. The tool was tested using green modeling clay as a stand-in for the alumina paste. The tamper successfully produced a layer approximately 1 mm thick; however, the surface exhibited ridges due to the layer lines from the 3D-printing process. For improved smoothness and durability, the tamper could be machined from aluminum using a lathe.



Figure 4.20 Pressing the tamper into modeling clay in the ionizer body's grooves, simulating the application of alumina paste (Al_2O_3).

In the filament heating tests shown in Figure 4.21, the pyrometer's measurement range was limited to a minimum of 249.0 °C and a maximum of 1370.1 °C. During the experiments, the supply current (I) and voltage (V) from the power supply were recorded, along with the pressure readings in both the test chamber and the pump, as summarized in Table 4.2. The filament was observed to first glow red at approximately 800 °C. After completing the heating cycle, the system was allowed to cool gradually before the vacuum pump was shut off, preventing air from entering the chamber and oxidizing the filament. This procedure helps extend the filament's operational lifetime.

Table 4.2 Recording data on MoRe filament heating under vacuum conditions.
* Pressure was measured only during the first trial to study outgassing behavior at various temperatures.

Temp. (°C)	Volt (V)				Current (A)				Pressure @Chamber (Torr)	Pressure @Pump (Torr)
	1	2	3	Mean	1	2	3	Mean		
249.0	0.7	0.6	0.5	0.6	2.2	2.5	1.9	2.2	3.00E-04	4.70E-06
300.0	-	0.6	0.5	0.6	3.9	2.5	1.9	2.8	3.00E-04	4.70E-06
400.0	-	0.8	0.7	0.8	3.9	2.9	2.5	3.1	4.10E-04	6.20E-06
500.0	1.0	1.0	0.9	1.0	3.9	3.5	3.3	3.6	3.00E-04	4.90E-06
600.0	1.3	1.3	1.3	1.3	4.3	4.2	4.1	4.2	1.44E-04	3.00E-06
700.0	1.8	1.7	1.6	1.7	5.5	5.1	4.8	5.1	1.87E-04	3.30E-06
800.0	2.1	2.1	2.0	2.1	6.2	6.1	5.8	6.0	1.80E-04	3.50E-06
900.0	2.5	2.7	2.5	2.6	6.9	7.1	6.8	6.9	1.17E-04	2.50E-06
1000.0	3.0	3.3	3.0	3.1	7.8	8.3	7.8	8.0	1.21E-04	2.50E-06
1100.0	3.4	3.9	3.6	3.6	8.6	9.4	8.9	9.0	1.21E-04	2.60E-06
1200.0	4.0	4.7	4.2	4.3	9.7	10.8	10.0	10.2	1.29E-04	2.70E-06
1300.0	5.9	5.3	4.9	5.4	12.7	11.9	11.1	11.9	1.83E-04	3.30E-06
1370.1	6.2	5.8	5.4	5.8	13.3	12.7	12.0	12.7	1.83E-04	3.30E-06

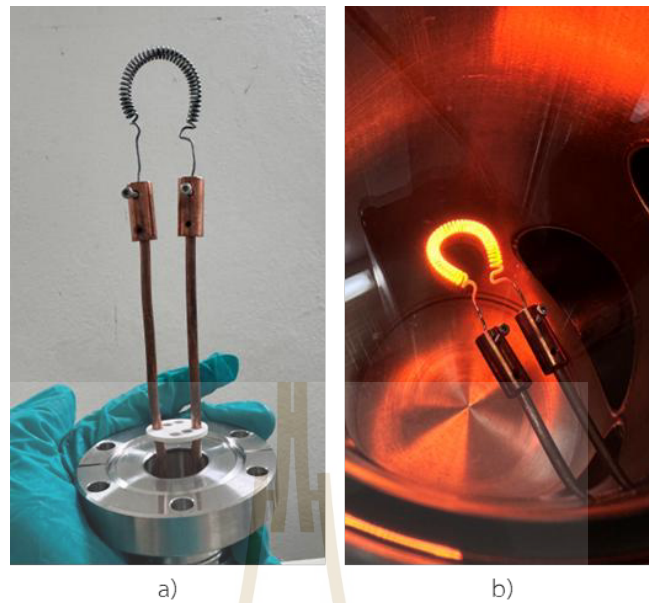


Figure 4.21 MoRe heater coil a) Before installation b) During testing at 800 °C

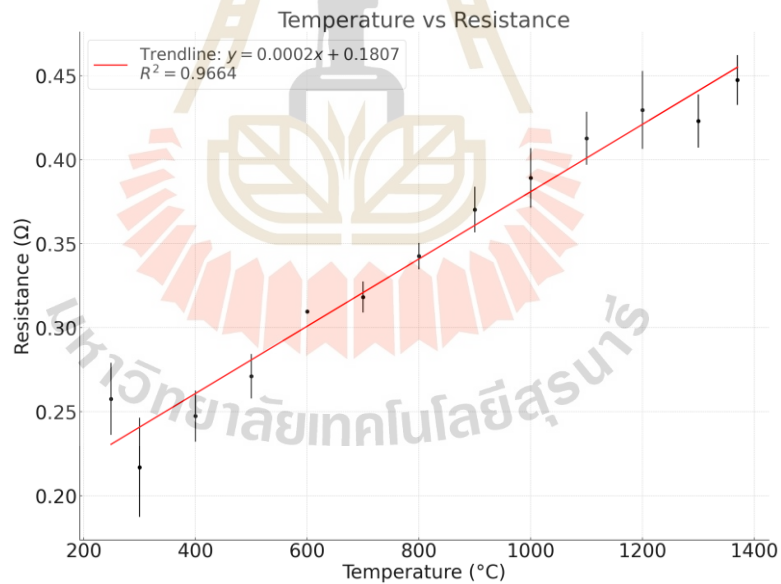


Figure 4.22 The graph shows the relationship between temperature and resistance.

The graph of Temperature vs Resistance in Figure 4.22 illustrates a typical behavior observed in metallic conductors. As the temperature increases, the resistance of the filament also increases. This positive correlation between temperature and resistance is due to the increased vibrations of the metal atoms at higher temperatures, which impedes the flow of electrons, thereby increasing resistance. The trendline in the graph is linear,

confirming the material behaves according to the linear relationship described by the formula $R(T) = R_0[1 + \alpha(T - T_0)]$. The calculated R^2 value indicates that the linear model fits the data well, suggesting that the filament material's resistive properties follow expected behavior for most metals at these temperatures. The graph demonstrates a clear, predictable increase in resistance with temperature, which is crucial for applications where temperature control and resistivity are important, such as in heating elements and thermistors.

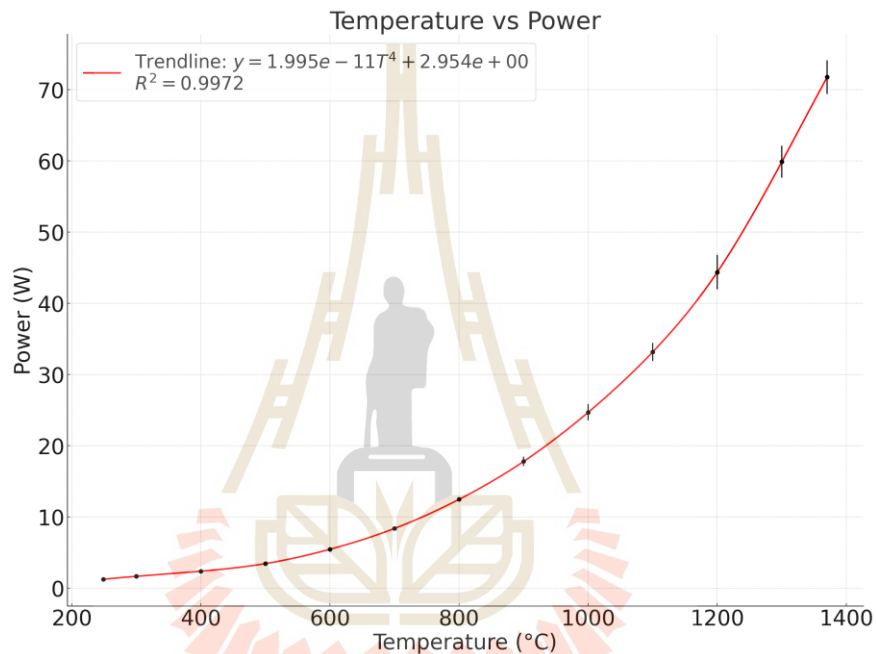


Figure 4.23 The graph shows the relationship between temperature and power consumption.

In the Temperature vs Power graph as shown in Figure 4.23, we observe the relationship between temperature and the power consumed by the filament. The power increases significantly as the temperature rises, following the relationship $P = IV$, where voltage and current increase with temperature. The trendline fits the data well using a T^4 model, which is consistent with the Stefan-Boltzmann law for radiation, suggesting that the energy radiated by the filament increases with the fourth power of its absolute temperature. The smooth curve shows a nonlinear increase in power with temperature, indicating that more energy is required to maintain the filament at higher temperatures. The R^2 value confirms a strong fit, showing that the power consumption behavior closely follows the theoretical model for radiative heat loss. This graph highlights the increasing

demands on energy as the filament heats up, which is important for energy efficiency considerations in high-temperature applications.

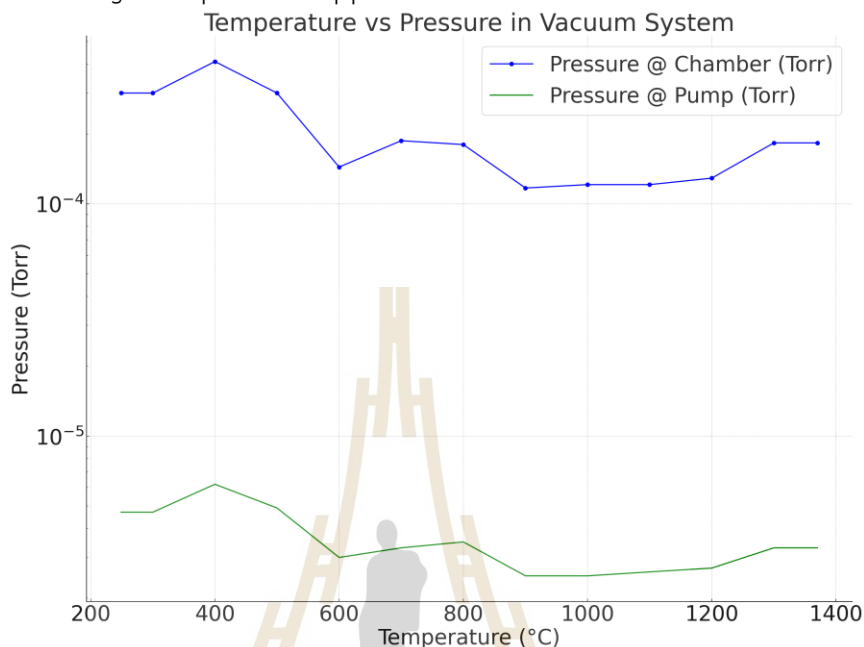


Figure 4.24 The graph shows the relationship between temperature and pressure in vacuum system.

The graph in Figure 4.24 presents the relationship between temperature and pressure at two locations within the vacuum system: the chamber and the pump. As temperature increases, pressure in both locations decreases, which is typical for vacuum systems. However, the chamber pressure remains consistently higher than the pump pressure, suggesting minor outgassing or leakage as the pump works to reduce the pressure further.

The data points follow a generally logarithmic decline with rising temperature. Using a logarithmic scale on the y-axis allows us to visualize small pressure changes at extremely low values, which would be difficult to discern on a linear scale. Interestingly, both pressures exhibit slight increases at approximately 400 °C, 800 °C, and 1300 °C, likely due to residual gases being released (outgassing) from chamber materials when heated.

CHAPTER V

CONCLUSION

This thesis comprised three main components: CST simulations, system assembly, and hands-on experiments. Using CST Studio Suite and SolidWorks modeling, a compact low-energy negative carbon ion beamline was designed, incorporating an octupole deflector, an Einzel lens, and a four-blade aperture slit. Simulations demonstrated that a 40 keV C^- ion beam could be focused to an RMS size of $2.42 \times 2.38 \text{ mm}^2$ with an emittance of $8 \text{ mm}\cdot\text{mrad}$ (equivalent to $1.6 \text{ mm}\cdot\text{mrad}\cdot\sqrt{\text{MeV}}$) at the slit, achieving 99% transmission through a fully open $20 \times 20 \text{ mm}^2$ aperture. Optimization of the Einzel lens identified a central-electrode bias of $-20,139 \text{ V}$ for precise focusing, while the octupole deflector enabled independent X and Y beam steering.

Misalignment studies established that the octupole deflector tolerates up to a 2° tilt and 2 mm offset, maintaining over 99 % transmission, and that its steering fields can correct 1 mm beam shifts with less than 300 V adjustments. The Einzel lens, however, demanded tighter tolerances of 0.4 mm offset and 0.6° tilt, beyond which the beam was lost due to field-symmetry disruption.

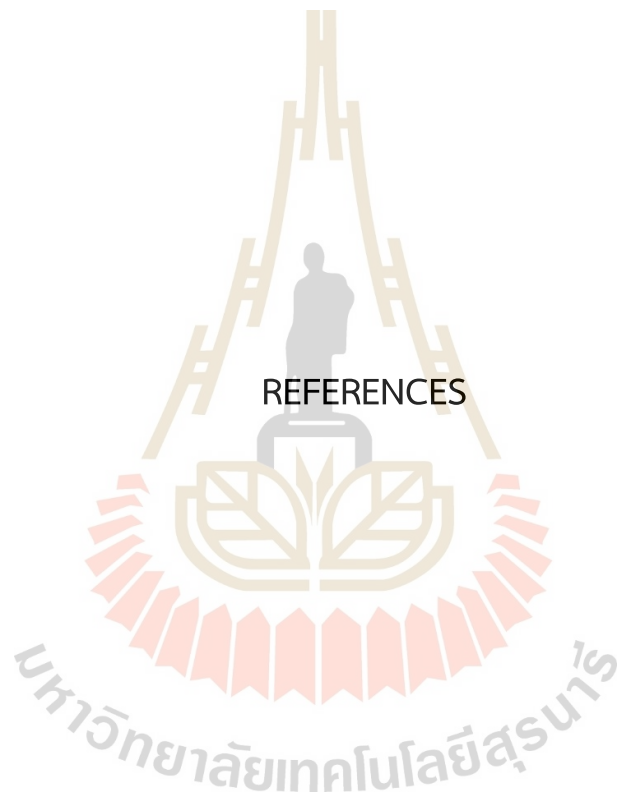
Existing SLRI vacuum components were cleaned, He leak-tested to $10^{-9} \text{ mbar}\cdot\text{L/s}$, and assembled into a tabletop UHV system with turbo-molecular pumps (300, 350, 700 L/s) and a scroll pump. Ten DC high-voltage supplies from Matsusada Precision (five for the cesium sputter source, floating on an isolation transformer; one for the Einzel lens; and four 1 kV units for the octupole rods) were controlled via CO-HV and CO-E32 fiber-optic interfaces, all mounted beneath the table on ceramic standoffs so that the chamber exterior remains at ground potential for safety.

The ionizer heater used a toroidal MoRe filament (0.9 mm diameter) designed to deliver $\sim 150 \text{ W}$ at 1200°C . Ohm's law and electrical resistance formula yielded a 20 cm coil length wound in 22 turns, later doubled to halve the power draw to $\sim 70 \text{ W}$. A 3D-printed tamper tool applied a 1 mm insulator layer; future aluminum tooling is expected to improve surface finish. Filament testing (pyrometer range $249\text{--}1370^\circ\text{C}$) confirmed that resistance rises linearly with temperature (TCR behavior) and that power consumption follows a T^4 trend (Stefan-Boltzmann radiation). Vacuum measurements showed decreasing chamber and pump pressures with temperature—typical for UHV systems—with slight pressure spikes at 400°C , 800°C , and 1300°C due to material outgassing.

Overall, the integrated design meets all performance targets, including compact footprint, beam quality, alignment tolerances, vacuum integrity, and reliable heating. It establishes a robust foundation for Thailand's first in-country AMS radiocarbon dating system.



REFERENCES



REFERENCES

- Balsley, D. R., Farwell, G. W., Grootes, P. M., and Schmidt, F. H. (1987). Ion source sample preparation techniques for carbon-14 AMS measurements. *Nuclear Instruments and Methods in Physics Research B*, 29, 37–40. [https://doi.org/10.1016/0168-583X\(87\)90199-6](https://doi.org/10.1016/0168-583X(87)90199-6)
- Broek, T. A. B., and Roberts, M. L. (2024). Improving IONPLUS MICADAS performance with recessed graphite. *Radiocarbon*, 1–9. <https://doi.org/10.1017/RDC.2024.36>
- Cathode Engineering Co. (2023). HeatWave Labs AG Cesium-Sputter Ionizer Product Data Sheet. Retrieved June 2025, from <https://www.cathode.com/pdf/101869a>
- Chomchan, N., Rugmai, S., and Songsiriritthigul, P. (2024). Design of electrostatic octupole deflector for accelerator mass spectrometer. In *Proceedings of the 19th Siam Physics Congress (SPC2024)* Krungsri River Hotel, Ayutthaya, Thailand.
- Drummond, I. W. (1984). The ion optics of low-energy ion beams. *Vacuum*, 34(1–2), 51–61. [https://doi.org/10.1016/0042-207X\(84\)90107-6](https://doi.org/10.1016/0042-207X(84)90107-6)
- Haag, A. M. (2016). Mass analyzers and mass spectrometers. In H. Mirzaei and M. Carrasco (Eds.), *Modern Proteomics: Sample Preparation, Analysis and Practical Applications (Advances in Experimental Medicine and Biology, Vol. 919)*. Springer International Publishing. https://doi.org/10.1007/978-3-319-41448-5_7
- Harris, S. A. (1987). The impact on archaeology of radiocarbon dating by AMS. *Philosophical Transactions of the Royal Society of London. Series A, Mathematical and Physical Sciences*, 325(1584), 3–10.
- Kieser, W. E. (2023). Accelerator mass spectrometry: An analytical tool with applications for a sustainable society. *EPJ Techniques and Instrumentation*, 10(7). <https://doi.org/10.1140/epjti/s40485-023-00088-9>
- Linick, T. W., Damon, P. E., Donahue, D. J., and Jull, A. J. T. (1989). Accelerator mass spectrometry: The new revolution in radiocarbon dating. *Quaternary International*, 1, 1–6. [https://doi.org/10.1016/1040-6182\(89\)90004-9](https://doi.org/10.1016/1040-6182(89)90004-9)

- Liu, S., Yang, Y., Xu, S., Zhang, H., Jiang, Y., and Shi, H. (2019). ^{14}C sample preparation vacuum line and graphite preparation method for ^{14}C -AMS measurement. *Rock and Mineral Analysis*, 38(3), 270–279. <https://doi.org/10.15898/j.cnki.11-2131/td.201807120084>
- Mandal, P., Sikler, G., and Mukherjee, M. (2011). An einzel lens with a diagonal-slit central electrode to combine steering and focusing of a low energy ion beam. arXiv: Nuclear Experiment. <https://arxiv.org/abs/1102.0213>
- Marchetti, A. A., Brown, T. A., Cox, C. C., Hamilton, T. F., and Martinelli, R. E. (2005). Accelerator mass spectrometry of actinides. *Journal of Radioanalytical and Nuclear Chemistry*, 263(2), 483–487. <https://doi.org/10.1007/10967-005-0022-4>
- Matsubara, A., Saito-Kokubu, Y., Nishizawa, A., Miyake, M., Ishimaru, T., and Umeda, K. (2014). Quaternary geochronology using accelerator mass spectrometry (AMS): Current status of the AMS system at the TONO Geoscience Center. InTech. <https://doi.org/10.5772/58549>
- Ojha, S. S. (2013). AMS – A novel method of dating in archaeology. *International Journal of Humanities and Religion*, 2(2), 37–43.
- Park, S.-H., Lee, S.-H., and Kim, Y.-S. (2020). Simulation study for beam extraction with an Einzel lens for low energy accelerator mass spectrometry. *Journal of the Korean Physical Society*, 77(5), 425–428. <https://doi.org/10.3938/jkps.77.425>
- Pfeiffer Vacuum GmbH. (n.d.). CF vacuum gate valves [Product data sheet]. Retrieved June 2025, from <https://www.pfeiffer-vacuum.com/products/vacuum-valves/gate-valves/>
- Purdue University Prime Lab. (n.d.). Ionizer. Retrieved June 2025, from https://www.physics.purdue.edu/primelab/ion_source/ionizer/ionizer.html
- Ratkus, A., Torims, T., Pikurs, G., Bjelland, V., Calatroni, S., Peacock, R., Serafim, C., Vretenar, M., and Wuensch, W. (2024). *Initial high electric field–vacuum arc breakdown test results for additively manufactured pure copper electrodes*. arXiv. <https://doi.org/10.48550/arXiv.2410.01714>

- Rhenium.com. (n.d.). Molybdenum-Rhenium alloy annealed properties. Retrieved June 2025, from https://rhenium.com/assets/molybdenum-rhenium_alloy_annealed_properties.pdf
- Saengwises, N., Chomchan, S., and Songsiriritthigul, P. (2024). Preliminary design and optimization of a compact SNICS ion source for radiocarbon accelerator mass spectrometry. In *Proceedings of the 19th Siam Physics Congress (SPC2024)*. Krungsri River Hotel, Ayutthaya, Thailand.
- Spivak-Lavrov, I. F., Sharipov, S. Y., and Sarsenbaev, B. O. (2023). Fringe fields of deflector plates with two earthed screens. *Nuclear Instruments and Methods in Physics Research A*, 1051, 16811. <https://doi.org/10.1016/j.nima.2022.168161>
- Synal, H.-A., Stocker, M., and Suter, M. (2007). MICADAS: A new compact radiocarbon AMS system. *Nuclear Instruments and Methods in Physics Research B*, 259, 7–13. <https://doi.org/10.1016/j.nimb.2007.01.138>
- Umput, S., and Songsiriritthigul, P. (2024). Design of electrostatic Einzel lens for accelerator mass spectrometer. In *Proceedings of the 19th Siam Physics Congress (SPC2024)*. Krungsri River Hotel, Ayutthaya, Thailand.



CURRICULUM VITAE

Name: Natthapong Saengwises

Date of Birth: 7 September 2000

Place of Birth: Nakhonratchasima, Thailand

Educations:

- 2019-2023: School of Physics, Science, Suranaree University of technology, Nakhon Ratchasima, Thailand (Bachelor of Science)
- 2023-2025: School of Physics, Science, Suranaree University of technology, Nakhon Ratchasima, Thailand (Master of Science)

Publication:

Saengwises, N., Ruhmai, S., Songsiriritthigul, P., 2024. Optimization of SNICS Design for Accelerator Mass Spectrometry. *E-Proceedings: The 19th Siam Physics Congress*, 29-32

Grants and Fellowship:

Development and Promotion of Science and Technology Talents Project (DPST)

